

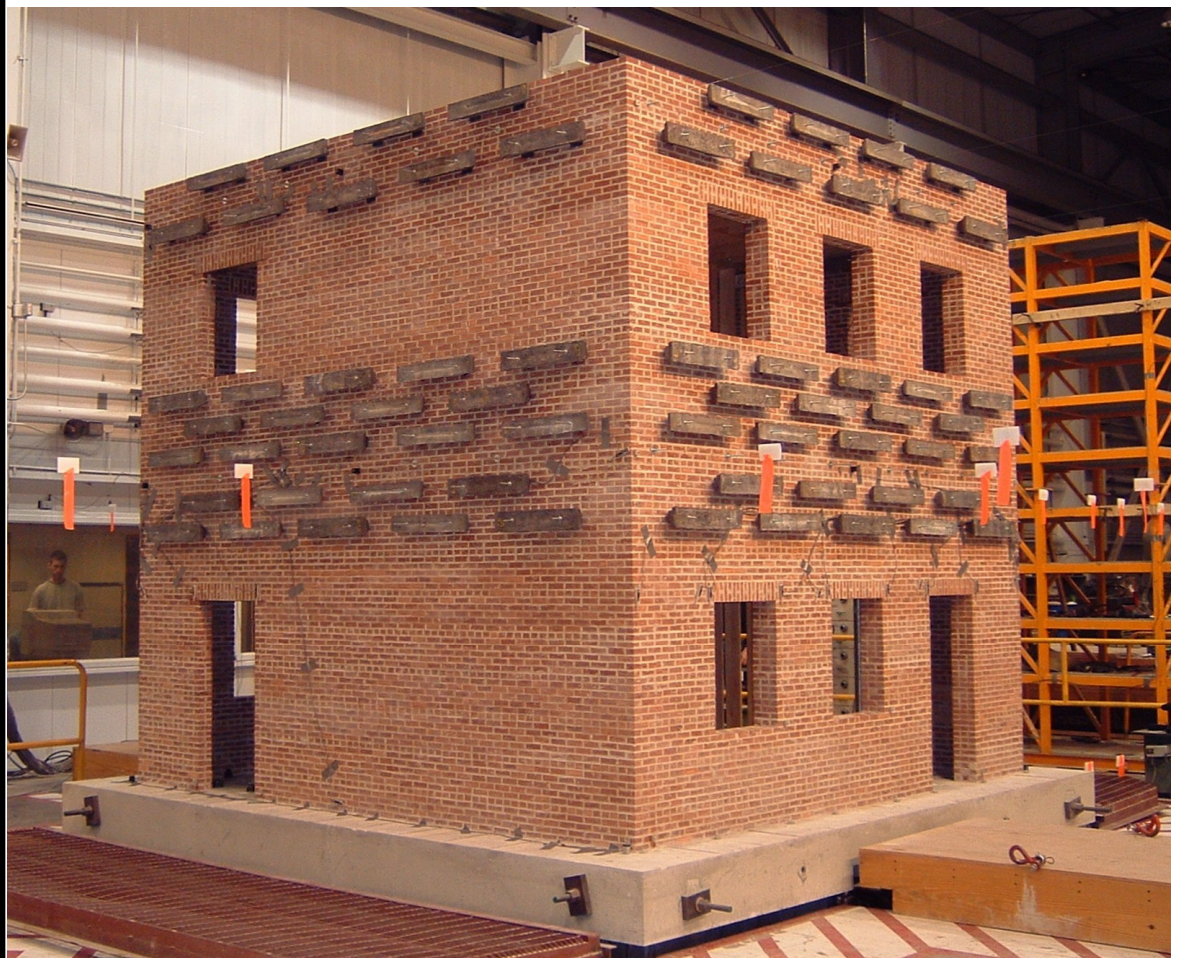


**US Army Corps  
of Engineers®**  
Engineer Research and  
Development Center

## **Seismic Response of a Half-Scale Masonry Building with Flexible Diaphragms**

Steven C. Sweeney, Matthew A. Horney, and  
Sarah L. Orton

September 2005



# Seismic Response of a Half-Scale Masonry Building with Flexible Diaphragms

Steven C. Sweeney, Matthew A. Horney, and Sarah L. Orton

*Engineer Research and Development Center  
Construction Engineering Research Laboratory  
PO Box 9005  
Champaign, IL 61826-9005*

## Final Report

Approved for public release; distribution is unlimited.

Prepared for     U.S. Army Corps of Engineers  
Washington, DC 20314-1000

Under             Work Unit AT41-CFM-A001

**ABSTRACT:** Unreinforced masonry (URM) buildings constructed on Army installations before the development of modern seismic codes may be susceptible to earthquake damage and therefore could benefit from seismic mitigation measures. Improved understanding of URM structural response under multidirectional loads is required to develop the most effective seismic structural retrofit strategies.

This research used a half-scale structural model to investigate the seismic response of URM buildings with flexible diaphragms. The objectives were to determine failure mechanisms and deformation behaviors; examine amplification of ground motion acceleration by walls and diaphragms; approximate any strength effects that flange portions of out-of-plane walls may have on in-plane walls; investigate vertical distribution of lateral forces; and identify any combinational effects of multidirectional base motions.

An unexpected level of out-of-plane wall flange contribution to in-plane wall strength indicates the need for experimental quantification using different pier layouts, URM wall combinations, and wall connection methods. Results also indicate the need to investigate the effect of overturning forces on the in-plane strength of piers and to determine critical ground motion characteristics that lead to the direct combination of response quantities due to orthogonal earthquake components.

**DISCLAIMER:** The contents of this report are not to be used for advertising, publication, or promotional purposes. Citation of trade names does not constitute an official endorsement or approval of the use of such commercial products. All product names and trademarks cited are the property of their respective owners. The findings of this report are not to be construed as an official Department of the Army position unless so designated by other authorized documents.

**DESTROY THIS REPORT WHEN NO LONGER NEEDED. DO NOT RETURN IT TO THE ORIGINATOR.**

# Contents

<b>List of Figures and Tables .....</b>	<b>v</b>
<b>Conversion Factors .....</b>	<b>x</b>
<b>Preface.....</b>	<b>xi</b>
<b>1 Introduction .....</b>	<b>1</b>
Background.....	1
Objective .....	4
Approach .....	4
Scope.....	5
Mode of Technology Transfer .....	5
<b>2 Development of the Test Model .....</b>	<b>6</b>
Design of Prototype .....	6
Masonry Design.....	7
Diaphragm Design .....	12
Material Properties.....	14
<i>Scaling</i> .....	18
<i>Placement of Simulated Mass</i> .....	19
Base Girder.....	21
<b>3 Selection of Model Seismic Motions.....</b>	<b>23</b>
Ground Motions Considered.....	23
Reasons for Selecting the Nahanni Earthquake .....	23
Characteristics of the Nahanni Earthquake .....	24
<b>4 Expected Building Response.....</b>	<b>27</b>
Independent Pier Behavior .....	27
<i>Failure Mode and Strength Calculations</i> .....	27
<i>Deformation Response of Piers</i> .....	32
Diaphragm Behavior .....	33
Force/Deformation Response of Structure (Pushover Analysis) .....	36
Building Mode Shapes and Frequencies.....	40
Predicted Dynamic Response .....	44
<i>Base Shears</i> .....	44
<i>Vertical Forces</i> .....	51
<i>Combined Shear and Vertical Force</i> .....	57
<i>Approximate Cracking Loads</i> .....	59
<b>5 Testing Program.....</b>	<b>61</b>

Test Structure Instrumentation .....	61
<i>Objective</i> .....	61
<i>Instrumentation Scheme</i> .....	62
Sequence of Testing .....	69
<i>Preliminary Testing</i> .....	69
<i>Damage-Level Testing</i> .....	71
Testing of Half-Scale Model .....	73
<i>Natural Frequencies and Damping (Undamaged State)</i> .....	74
<i>Seismic Test Observations at Low-Level Excitation</i> .....	75
<i>Seismic Test Observations at High Level Excitation</i> .....	76
<i>Natural Frequencies and Damping (Final Damage State)</i> .....	79
<b>6 Evaluation of Test Model Behavior.....</b>	<b>81</b>
Force/Deformation Relationships of Walls.....	81
Acceleration Amplifications .....	88
<i>Behavior of Flanges in Out-of-Plane Walls</i> .....	93
Vertical Distribution of Lateral Forces.....	96
<i>Combinational Effect of Bidirectional Excitation on Test Model</i> .....	99
<b>7 Implications of Research on Seismic Provisions .....</b>	<b>102</b>
Force/Deformation Prescriptions .....	102
Vertical Distribution of Lateral Forces .....	105
Strength Contributions to In-Plane Walls from Out-of-Plane Wall Flanges .....	106
Combination of Seismic Forces for Multi-component Excitation .....	107
<b>8 Conclusions and Recommendations .....</b>	<b>109</b>
Conclusions .....	109
Recommendations.....	111
<b>References .....</b>	<b>113</b>

# List of Figures and Tables

## Figures

Figure 2–1. St. Louis firehouse structurally similar to test model.....	6
Figure 2–2. Prototype test structure design features.....	7
Figure 2–3. Elevation of wall B; wall A is identical mirrored image.....	8
Figure 2–4. Elevation of wall 1.....	9
Figure 2–5. Elevation of wall 2.....	9
Figure 2–6. Plan of test structure and coordinate system used.....	10
Figure 2–7. Pin connection for steel support column.....	11
Figure 2–8. Construction of test model.....	12
Figure 2–9. Completed masonry.....	12
Figure 2–10. Plan of diaphragm.....	13
Figure 2–11. Connection detail.....	14
Figure 2–12. Cutting of half scale bricks.....	14
Figure 2–13. Dissection of full scale brick into eight half scale bricks (units in inches).....	15
Figure 2–14. Modulus of rupture test of individual brick.....	16
Figure 2–15. Compression test of prism.....	16
Figure 2–16. Compression test of mortar cube.....	17
Figure 2–17. Flexure test of prism.....	17
Figure 2–18. Bond wrench test of prism.....	17
Figure 2–19. Layout of additional weight on walls.....	20
Figure 2–20. Layout of additional weight on diaphragms.....	20
Figure 2–21. Layout of base girder.....	22
Figure 3–1. Modified Nahanni x-direction time history (walls A and B in-plane).....	25
Figure 3–2. Modified Nahanni y-direction time history (walls 1 and 2 in-plane).....	25
Figure 3–3. Modified Nahanni x-direction acceleration response spectrum for 5% damping.....	25
Figure 3–4. Modified Nahanni y-direction acceleration response spectrum for 5% damping.....	26
Figure 4–1. Pier numbers.....	28
Figure 4–2. Force/deformation curve for masonry piers per FEMA 356.....	28
Figure 4–3. Forces on free standing pier.....	30
Figure 4–4. Deflection of diaphragm.....	34

Figure 4–5. Force/deformation relationships for walls A and B.....	37
Figure 4–6. Force/deformation relationship for wall 1.....	37
Figure 4–7. Force/deformation relationship for wall 2.....	38
Figure 4–8. Comparison of 2D and 3D pushover curves for walls A and B.....	38
Figure 4–9. Comparison of 2D and 3D pushover curves for walls 1 and 2.....	39
Figure 4–10. P-delta effects for A-B plane direction.....	40
Figure 4–11. P-delta effects for 1-2 plane direction.....	40
Figure 4–12. 3D finite element model created in SAP 2000NL.....	41
Figure 4–13. First-mode shape of test structure, period of 0.096 sec.....	42
Figure 4–14. Second-mode shape of test structure, period of 0.086 sec.....	42
Figure 4–15. Third-mode shape of test structure, period of 0.063 sec.....	43
Figure 4–16. Fourth-mode shape of test structure, period of 0.053 sec.....	43
Figure 4–17. Distribution of shear forces for earthquake only in the x-direction.....	45
Figure 4–18. Shear in piers of wall A for earthquake only in the x-direction.....	46
Figure 4–19. Shear in piers of wall 1 for earthquake only in the x-direction.....	46
Figure 4–20. Distribution of shear forces for earthquake only in the y-direction.....	47
Figure 4–21. Shear in piers of wall 1 for earthquake only in the y-direction.....	48
Figure 4–22. Shear in piers of wall A for earthquake only in the y-direction.....	48
Figure 4–23. Shear in piers of wall B for earthquake only in the y-direction.....	49
Figure 4–24. Shear in pier 4 for unidirectional and bidirectional Nahanni earthquake.....	50
Figure 4–25. Shear in pier 12 for unidirectional and bidirectional Nahanni earthquake.....	50
Figure 4–26. Direction of vertical forces for positive x-direction earthquake.....	52
Figure 4–27. Direction of vertical forces for positive y-direction earthquake.....	52
Figure 4–28. Combination of vertical stresses on an in-plane pier for unidirectional loads only.....	53
Figure 4–29. Vertical forces in piers 12 and pier 4, along with their sum, for y-direction earthquake.....	54
Figure 4–30. Vertical forces in pier 10 and pier 5, along with their sum, for y-direction earthquake.....	55
Figure 4–31. Vertical forces in wall A for y-direction earthquake only.....	56
Figure 4–32. Vertical forces in pier 2 for unidirectional and bidirectional ground motions.....	56
Figure 4–33. Interaction of base shear and vertical forces for pier 2 under simultaneous xy ground motion.....	58
Figure 4–34. Variation of lateral strength based on vertical load of a 20" x 24.6" pier based on FEMA 356.....	58
Figure 5–1. Accelerometers located at base beam level.....	62
Figure 5–2. Accelerometers located at the floor diaphragm level.....	63
Figure 5–3. Accelerometers located at the roof diaphragm level.....	63

Figure 5–4. Global displacement transducers located at base beam level. ....	64
Figure 5–5. Global displacement transducers located at floor diaphragm level. ....	65
Figure 5–6. Global displacement transducers located at roof diaphragm level. ....	65
Figure 5–7. Local displacement transducers for wall A. ....	66
Figure 5–8. Local displacement transducers for wall B. ....	67
Figure 5–9. Local displacement transducers for wall 1. ....	67
Figure 5–10. Local displacement transducers for wall 2. ....	68
Figure 5–11. Instrumentation on pier 1. ....	68
Figure 5–12. Typical white-noise test waveform. ....	70
Figure 5–13. Typical sine-sweep test waveform. ....	70
Figure 5–14. Typical transfer function generated by a white-noise test or sine-sweep test. ....	71
Figure 5–15. Typical building response to sine-decay test. ....	73
Figure 5–16. Crack locations in wall 1 after 20%-XY seismic test. ....	76
Figure 5–17. Permanent offset at the top of pier 4 after completed seismic testing. ....	77
Figure 5–18. Crack locations in wall A after completed seismic testing. ....	77
Figure 5–19. Crack locations in wall B after completed seismic testing. ....	78
Figure 5–20. Crack locations in wall 1 after completed seismic testing. ....	78
Figure 5–21. Crack locations in wall 2 after completed seismic testing. ....	79
Figure 6–1. Six-degree-of-freedom model used to compute seismic forces. ....	82
Figure 6–2. Applied base shear on wall A during 20%-X test. ....	84
Figure 6–3. Plot of experimental force/deformation response of wall A. ....	84
Figure 6–4. Plot of experimental force/deformation response of wall B. ....	85
Figure 6–5. Plot of experimental force/deformation response of wall 1. ....	85
Figure 6–6. Plot of experimental force/deformation response of wall 2. ....	85
Figure 6–7. Plot of experimental force/deformation response of wall A (integrated displacement). ....	87
Figure 6–8. Plot of experimental force/deformation response of wall B (integrated displacement). ....	87
Figure 6–9. Plot of experimental force/deformation response of wall 1 (integrated displacement). ....	88
Figure 6–10. Plot of experimental force/deformation response of wall 2 (integrated displacement). ....	88
Figure 6–11. Wall A and wall B amplification of ground acceleration in the x-direction. ....	89
Figure 6–12. Average wall amplification of ground acceleration in the x-direction. ....	90
Figure 6–13. Floor and roof diaphragm amplification of average wall acceleration in the x-direction. ....	90
Figure 6–14. Floor and roof diaphragm amplification of ground acceleration in the x- direction. ....	91

Figure 6–15. Wall 1 and wall 2 amplification of ground acceleration in the y-direction. ....	91
Figure 6–16. Deflected shape of diaphragms during 20%-Y test (with quadratic best fit). ....	92
Figure 6–17. Floor and roof diaphragm amplification of average wall acceleration in the y-direction. ....	93
Figure 6–18. Floor and roof diaphragm amplification of ground acceleration in the y-direction. ....	93
Figure 6–19. Crack pattern on pier 12 and pier 4 indicating structural continuity. ....	94
Figure 6–20. Variation in strength of wall 2 including overturning moment for 30%-XY earthquake. ....	95
Figure 6–21. Vertical distribution of lateral forces in the x-direction. ....	98
Figure 6–22. Vertical distribution of lateral forces in the y-direction. ....	98
Figure 6–23. Base shear on wall A due to 20% unidirectional and bidirectional earthquakes. ....	100
Figure 6–24. Base shear on wall A for the superposition of the 20% unidirectional earthquakes and for the 20% bidirectional earthquake. ....	101
Figure 7–1. Comparison of force/deformation responses measured during seismic tests with those predicted by FEMA 356 for Wall A. ....	103
Figure 7–2. Comparison of force/deformation responses measured during seismic tests with those predicted by FEMA 356 for Wall B. ....	103
Figure 7–3. Comparison of force/deformation responses measured during seismic tests with those predicted by FEMA 356 for Wall 1. ....	103
Figure 7–4. Comparison of force/deformation responses measured during seismic tests with those predicted by FEMA 356 for Wall 1 (based on actual crack pattern). ....	104
Figure 7–5. Comparison of force/deformation responses measured during seismic tests with those predicted by FEMA 356 for Wall 2. ....	104

## Tables

Table 2-1. Results of brick tests. ....	15
Table 2-2. Results of prism and mortar tests. ....	16
Table 2-3. Scaling relationships. ....	19
Table 4-1. Pier force/deformation behavior. ....	29
Table 4-2. Pier lateral strengths based on FEMA 356. ....	32
Table 4-3. Diaphragm deflections (inches). ....	36
Table 4-4. Comparison of peak shear forces due to bidirectional excitation with those predicted by the FEMA 368 combination rule. ....	51
Table 4-5. Maximum and minimum vertical forces due to unidirectional and bidirectional earthquakes. ....	57
Table 4-6. Cracking loads predicted by SAP 2000NL for Nahanni x-direction earthquake. ....	59
Table 4-7. Cracking loads predicted by SAP 2000NL for Nahanni y-direction earthquake. ....	60

Table 4-8. Cracking loads predicted by SAP 2000NL for combined Nahanni x-direction and y-direction earthquake.....	60
Table 5-1. Sequence of preliminary tests performed on the structure. ....	69
Table 5-2. Sequence of damage-level tests performed on the structure. ....	72
Table 5-3. Results from white-noise and sine-sweep tests on undamaged building (sec). ....	74
Table 5-4. Results from sine-decay tests on undamaged building. ....	75
Table 5-5. Results from white-noise test on damaged building (sec). ....	80
Table 5-6. Results from sine-decay tests on damaged building.....	80
Table 6-1. Mass associated with test model degrees of freedom for ground motion in the x-direction and y-direction. ....	83
Table 6-2. Comparison of expected strengths and peak forces resisted for walls of test model.....	96
Table 6-3. Ratio of lateral floor forces to lateral roof forces in the x-direction (kips). ....	97
Table 6-4. Ratio of lateral floor forces to lateral roof forces in the y-direction (kips). ....	97
Table 6-5. Base shear on wall A and wall B for 10% earthquakes (kips). ....	99
Table 6-6. Base shear on wall A and wall B for 20% earthquakes (kips). ....	99

## Conversion Factors

Units of measure used in this report can be converted to SI\* units as follows:

Multiply	By	To Obtain
acres	4,046.873	square meters
cubic feet	0.02831685	cubic meters
cubic inches	0.00001638706	cubic meters
degrees (angle)	0.01745329	radians
degrees Fahrenheit	$(5/9) \times (^{\circ}\text{F} - 32)$	degrees Celsius
degrees Fahrenheit	$(5/9) \times (^{\circ}\text{F} - 32) + 273.15$	kelvins
feet	0.3048	meters
gallons (U.S. liquid)	0.003785412	cubic meters
horsepower (550 ft-lb force per second)	745.6999	watts
inches	0.0254	meters
kips per square foot	47.88026	kilopascals
kips per square inch	6.894757	megapascals
miles (U.S. statute)	1.609347	kilometers
pounds (force)	4.448222	newtons
pounds (force) per square inch	0.006894757	megapascals
pounds (mass)	0.4535924	kilograms
square feet	0.09290304	square meters
square miles	2,589,998	square meters
tons (force)	8,896.443	newtons
tons (2,000 pounds, mass)	907.1847	kilograms
yards	0.9144	meters

---

\* *Système International d'Unités* (International System of Measurement), i.e., the metric system.

## Preface

This research was conducted for Headquarters, U.S. Army Corps of Engineers (HQUSACE), under Program 21 2040 622784T4100, “Military Facilities Engineering Technologies”; Project AT41-CFM-A001, “Seismic Rehabilitation of Roof and Floor Systems.” The Technical Monitor was Peter J. Rossbach, CECW-CE-R-NAD.

The work was performed by the Materials and Structures Branch (CF-M) of the Facilities Division (CF), Construction Engineering Research Laboratory (CERL). The CERL Project Manager was Steven C. Sweeney. The technical editor was Gordon L. Cohen, Information Technology Laboratory – Champaign. Martin J. Savoie is Chief, CEERD-CF-M, and L. Michael Golish is Chief, CEERD-CF. The Technical Director for this work unit was Dr. Paul A. Howdyshell, CEERD-CV-ZT. The Acting Director of CERL is Dr. Ilker R. Adiguzel.

CERL is an element of the Engineer Research and Development Center (ERDC), U.S. Army Corps of Engineers. The Commander and Executive Director of the ERDC is COL James R. Rowan, EN, and the Director is Dr. James R. Houston.

# 1 Introduction

## Background

Unreinforced masonry (URM) is one of the oldest types of building construction and is common throughout the United States. Masonry buildings constructed before the development of modern seismic codes may be susceptible to damage caused by earthquakes and therefore could benefit from seismic mitigation through modification of their structural elements. To develop the most effective seismic retrofit strategy, a clear understanding of the behavior of URM buildings under multidirectional loads is required.

The study documented here was conducted jointly by the U.S. Army Engineer Research and Development Center – Construction Engineering Research Laboratory (ERDC-CERL) and the Mid-America Earthquake Center, University of Illinois at Urbana-Champaign to fill gaps in current knowledge and to verify the findings of select previous studies. The project methodology was developed with reference to previous studies of the seismic performance of masonry buildings and multidirectional combinations of seismic motions. Studies of particular interest are summarized below.

**Masonry Buildings with Flexible Diaphragms.** Tena-Colunga (1992) investigated the seismic response of a URM firehouse with flexible wood diaphragms to the Loma Prieta Earthquake. The firehouse was one of the first instrumented masonry buildings subjected to moderate-intensity ground motion. Although peak diaphragm accelerations were as high as 0.79 g, the building sustained little damage, demonstrating that URM systems with flexible diaphragms can resist sizeable earthquakes. Tena-Colunga also compared the measured response of the building with several analytical models and found that three-dimensional (3D) quasi-dynamic analysis can produce reliable results.

Abrams published a paper in the “Proceedings of the Structures Congress” (1995) that discussed four aspects of flexible diaphragm behavior not usually considered by practicing structural engineers when performing a seismic design. In particular, he examined diaphragm amplification, diaphragm/wall frequency relations,

and the influence of diaphragms on the vertical and horizontal distributions of lateral force. Abrams stated that those aspects of response will differ for rigid and flexible diaphragms and thus need to be considered when evaluating a building system for seismic mitigation.

Costley and Abrams (1996) published a report entitled *Dynamic Response of Unreinforced Masonry Buildings with Flexible Diaphragms*. Their research studied the response of two half-scale rectangular URM buildings subjected to uniaxial earthquake loads. The behavior of the test models demonstrated that pier rocking is a stable nonlinear failure mode, with recorded ductility values greater than 6. The test results also indicated that out-of-plane wall flange effects are minimal and can be ignored when computing the in-plane strength of walls. Although a great deal of information was documented in the study, the authors expressed the need for additional research to test buildings with a nonsymmetrical layout and various pier aspect ratios.

Kingsley et al. (1996) performed a quasi-static cyclic test on a full-scale URM building modeled after the structure tested by Costley and Abrams (1996). The authors determined that simple numerical models can be used to predict the strength of in-plane walls. However, test results indicated that the determination of rocking strength should include consideration of pier heights other than the clear distance of an adjacent window. They also concluded that the variation of axial stress due to global overturning moment in the test model's exterior piers had a significant effect on the piers' failure modes.

To complement studies on small-scale structures and component testing, Paquette and Bruneau (2003) carried out pseudo-dynamic testing of a full-scale one-story URM building with wood diaphragms. Their work confirmed previous findings that rocking and sliding mechanics allowed for large deformations with a relatively small amount of strength degradation. Furthermore, by designing a structure with discontinuous corners on one in-plane wall, they found that continuous corners seemed to have a negligible effect on the strength of an in-plane wall for large-magnitude earthquakes.

Cohen (2000) investigated seismic response of low-rise masonry buildings with flexible roof diaphragms. That study focused on the response of floor diaphragms in rectangular half-scale reinforced masonry buildings. He concluded that the building responded as a single degree of freedom system associated with the degree of freedom of the diaphragm. However, the aspect ratio of the diaphragm in Cohen's study was nearly five times the aspect ratio of the diaphragm used in this investigation.

Simsir et al. (2001) studied the influence of diaphragm flexibility on the out-of-plane response of URM walls. Their experiments consisted of uniaxial tests on two out-of-plane URM walls unconnected to two in-plane walls. They found that increased diaphragm flexibility significantly increased the out-of-plane displacement of the URM walls. The increase in displacement was consistent with the increase in period associated with the flexibility of the diaphragm. They also found that the intensity of the axial load affects the out-of-plane demands. However, their study did not examine the effect of connecting the out-of-plane walls to the in-plane walls.

**Multidirectional Combinations of Seismic Motions.** Wilson et al. (1981) questioned the acceptability of the square root sum of squares (SRSS) method for combining modal maxima in 3D analysis. They found that for torsionally sensitive buildings whose modal vibration frequencies were close, the SRSS method could overestimate the response by up to a factor of 14. The authors presented the complete quadratic combination (CQC) method that takes into account statistical coupling between closely spaced modes.

Anastassiadis et al. (2002) studied the most unfavorable combination of three simultaneous internal forces. They concluded that in order to avoid unnecessary over-dimensioning, the internal forces could be designed by using the extreme value of one force and the probable values of the others. The extreme and probable values are based on the most critical orientation of seismic excitation. However, their study mainly focused on column behavior where the internal forces in question were the x and y bending moments and the axial force. They did not consider behavior of a masonry pier, whose lateral strength is highly dependent on axial stress.

Lopez et al. (2001) evaluated combination rules for multi-component seismic analysis. They found that the current combination rules of SRSS, 30%, and 40% produced errors as large as 18% in determining the design forces to be used. They also concluded that the critical response increases when the vibration periods of the two modes most associated with the orthogonal directions of horizontal ground motion become close to each other. However, their study did not include systems whose orthogonal lateral force resisting systems were not independent, such as in masonry buildings.

Hwang and Hsu (2000) conducted an experimental study examining base isolated buildings under triaxial ground excitations. They studied a series of symmetrical and unsymmetrical base isolated buildings under independently and simultaneously applied ground motions. They found that vertical accelerations

may dramatically increase maximum story accelerations for cases where there is eccentricity on the isolation system. They also found that the maximum displacement predicted using the 100% - 30% combination rule might not be conservative.

## Objective

The overall objective of this project was to achieve a better understanding of the seismic response of URM buildings with flexible diaphragms through experimental testing of a half-scale structural model. Specific tasks executed toward that objective were to:

1. Determine failure mechanisms and force/deformation behavior of the test model's walls.
2. Examine acceleration amplification of ground motion by walls and diaphragms.
3. Approximate any effect that the flange portions of out-of-plane walls may have on the strength of in-plane walls.
4. Investigate the vertical distribution of lateral forces for stiff-wall/flexible-floor systems.
5. Determine the combinational effect of multidirectional base motions on the test model.
6. Provide fundamental knowledge needed to develop seismic protection designs.

## Approach

A half-scale URM building with flexible wood diaphragms was constructed and tested at CERL on the Triaxial Earthquake and Shock Simulator (TESS). Prototypical structures were evaluated and gaps in current knowledge were considered to determine the design of the test model. The final model included structural features common to URM buildings, such as perforated shear walls and flexible diaphragms. Special attention was paid to the actual material properties of the test specimen and the effects of scaling.

A finite element analytical model was developed to predict the response of the physical test model to three recorded earthquake ground motions: 1985 Nahanni, 1940 El Centro, and 1989 Loma Prieta. Based on the results of the analyses, the Nahanni earthquake was selected as the test motion of greatest

interest with respect to the research objectives. The horizontal ground motion components were applied independently and also simultaneously. Seismic tests were initially applied at a low level to measure the test model's linear/elastic response and then increased until the piers developed failure mechanisms. The behavior of the test model is evaluated both in terms of the current research objectives and broader implications for the design methods prescribed by seismic codes.

## **Scope**

The experimental research presented here is part of a larger project that included a preliminary analytic study (Sweeney et al. 2004) and will conclude with a study of rehabilitation methods on the test model. The study reported here parallels a program at the Georgia Institute of Technology using full-scale static tests (Moon 2004, Yi 2004).

## **Mode of Technology Transfer**

The results of this investigation will be presented internally to U.S. Army Corps of Engineers (USACE) personnel through USACE Structural Engineering Workshops, and externally to the structural engineering community at appropriate professional technical conferences. The results of this study will be used to evaluate the behavior of a rehabilitated model building tested within the overall scope of this research effort. Information developed in this project will be submitted for incorporation into appropriate Federal Emergency Management Agency (FEMA) documents and model building code documents for seismic design, evaluation, and mitigation of structures.

## 2 Development of the Test Model

The test structure described in this section was designed to be used in a triaxial dynamic test. This chapter presents an analytical study of the half-scale test structure, and all finite element models and calculations documented here are based on the actual design of that structure.

### Design of Prototype

The prototype for the test structure was developed as part of a collaborative effort between the University of Illinois at Urbana-Champaign and the Georgia Institute of Technology, Atlanta. The prototypical structure was designed to represent older unreinforced brick buildings such as the firehouse shown in Figure 2–1. The test structure is two stories like many common low-rise URM buildings. One wall (whose parallel wall is identical) represents a typical masonry wall with windows and doors, as might be found in a masonry house or military barracks. Another wall represents a firehouse garage with a large opening that also is structurally similar to a storefront design. The final wall is almost solid typical of the side wall or back wall of a store. The diaphragms at the second floor and roof levels are constructed as wood floor decking (Figure 2–2).



Figure 2–1. St. Louis firehouse structurally similar to test model.

The test structure was also designed to reveal aspects of performance that meet the objectives of the overall project. The pair of identical in-plane walls have multiple piers and are designed to study the effects of selectively rehabilitating a pier on the overall performance of the structure. The use of both solid and open walls creates a torsional irregularity that is common to many masonry buildings. The walls are also designed to examine the effects of rehabilitating a weak wall that works in parallel with a strong wall. The flexible diaphragm will deliver the same horizontal load to each wall, independent of the walls' relative strengths or stiffness, so the effects of strengthening the weak wall on system performance are accentuated. Finally, these types of wall/pier combinations are typical of actual construction and will help determine the response of real buildings to earthquakes.

Inherent inadequacies exist in both full-scale static tests and half-scale dynamic tests. Full-scale static tests do not accurately represent strain rate effects or true inertial force distributions. At the same time, reduced-scale dynamic tests are difficult due to the problems of scaling mass, material properties, and ground motions. A goal of this research was to design full-scale and half-scale prototypical structures with similar design and expected behavior such that when the two types of models are tested in parallel, the results are comparable.

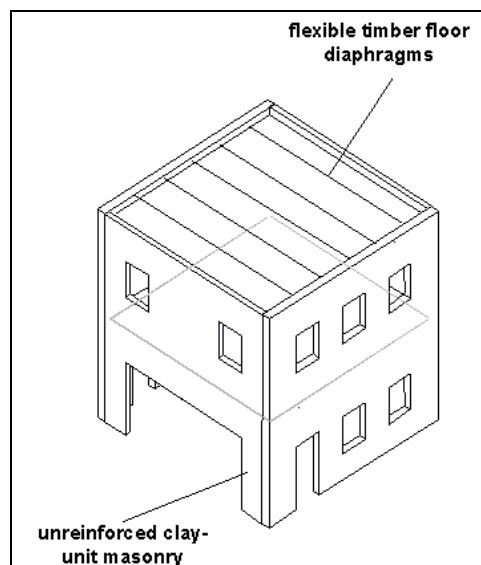


Figure 2–2. Prototype test structure design features.

## Masonry Design

With the basic design for a prototype developed, the specific layout and design details were then determined. Elevation drawings of the walls can be seen in



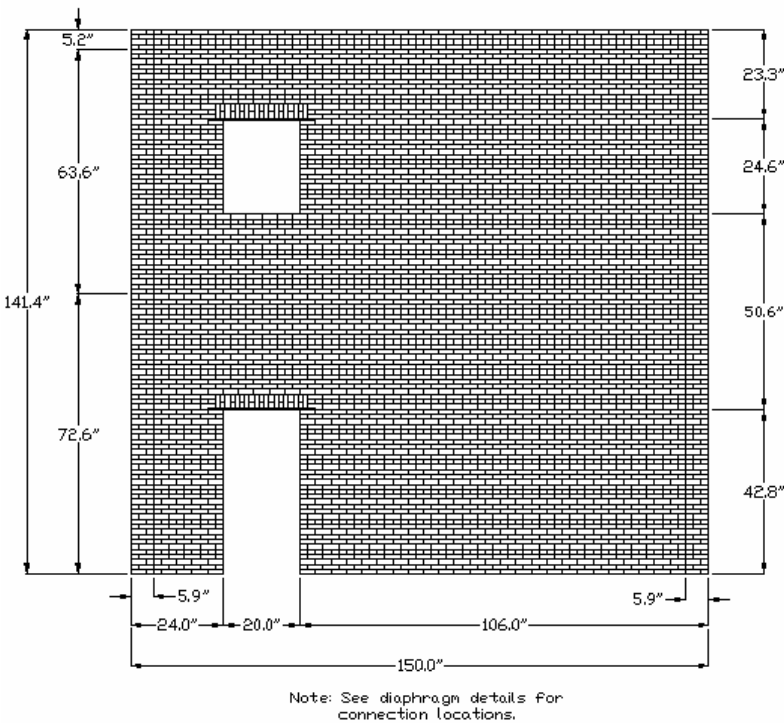


Figure 2-4. Elevation of wall 1.

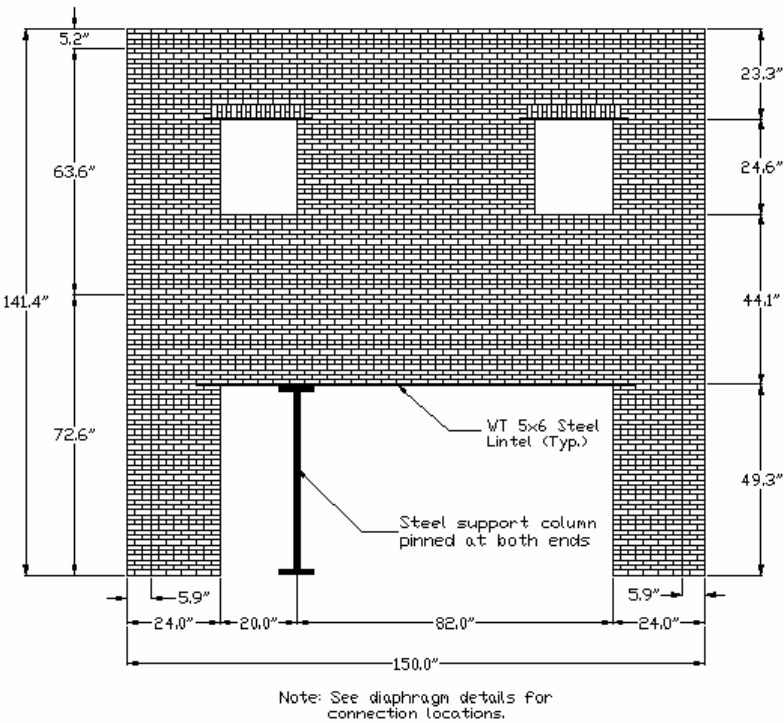
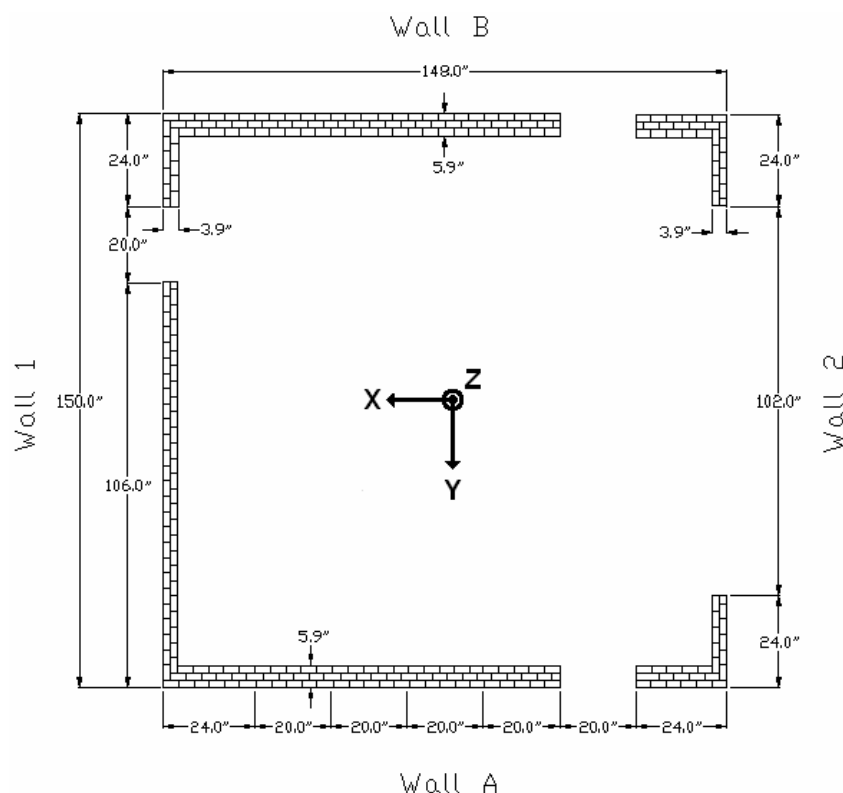


Figure 2-5. Elevation of wall 2.



**Figure 2-6. Plan of test structure and coordinate system used.**

Walls A and B are three wythes thick to represent typical bearing walls. Walls 1 and 2 are two wythe thick to represent typical non-load-bearing walls. Each wall is constructed with a header course every six rows. The mortar is type O (1:2:9) to represent weak mortar typically found in older buildings.

Wall 2 was designed to be typical of a wall with a large garage door and an adjacent standard door. The brick pier that would typically exist between them would likely sustain severe damage during testing and possibly present a safety hazard. Therefore, a steel column was added to simulate the behavior of a brick pier without failing during testing. The support column was pinned at both ends using two plates with a steel ball in the center, as shown in Figure 2-7. This allowed the support column to move freely in all directions, while providing vertical resistance. A similar type of construction found in existing buildings uses a steel column behind the brick pier.

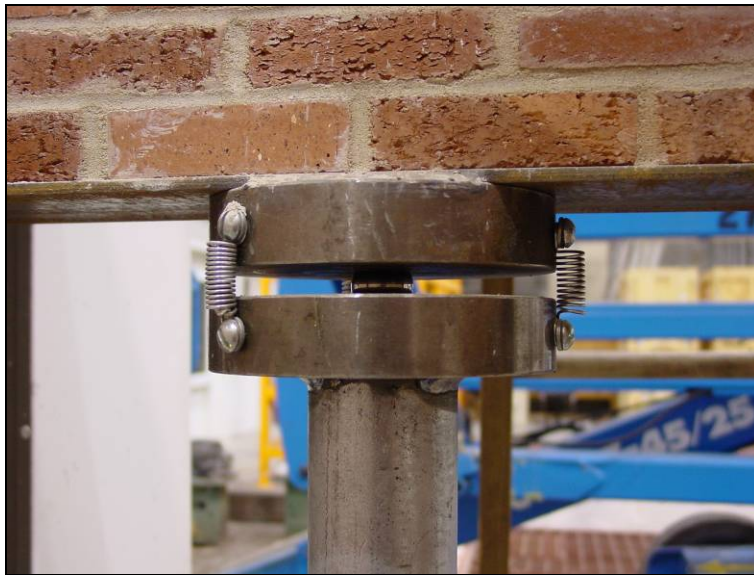


**Figure 2–7. Pin connection for steel support column.**

The large opening on wall 2 required the use of a steel lintel. In order to limit the deflection to the  $l/600$  maximum value prescribed by the Masonry Standard Joint Committee (MSJC 1999), a steel WT5x6 was used. The lintel is continuous over the steel support column. The other lintels in walls 1 and 2 are also WT5x6 sections. Unreinforced masonry lintels were designed for walls A and B. Details can be found in Appendix A.

Construction of the test model took place between August and December 2001. The structure was constructed off the shake table and then lifted onto the table by aid of a concrete base girder. Two professional masons constructed the walls at the ERDC-CERL test facility, as shown in Figure 2–8.



Figure 2–8. Construction of test model.

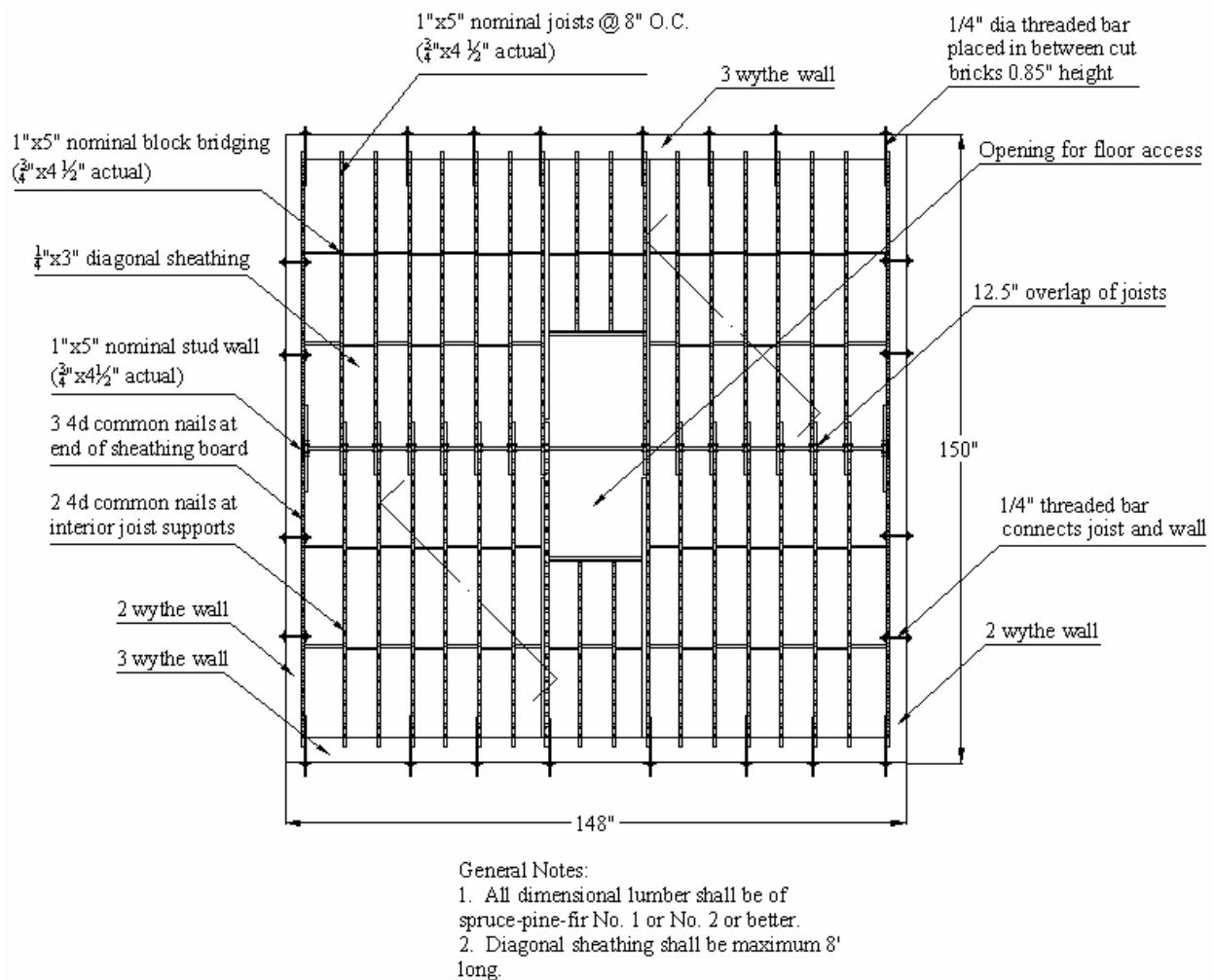


Figure 2–9. Completed masonry.

## Diaphragm Design

The floor and roof were designed as typical wood diaphragms. The design is identical for both floors, and it consists of 1/4 in. diagonal sheathing and 1 x 5 joists, as shown in Figure 2–10. The diaphragm is tied to each wall by 1/4 in. threaded steel bars. The locations of the joist-to-wall connections are shown in

Figure 2–10 and details of connections along walls A and B are illustrated in Figure 2–11. Walls 1 and 2 are bolted to the outermost joist on each side of the floor. The diaphragm is designed to obtain frequency ratios between the wall and the diaphragm that realistically emulate real-world structures. This design allows a distinction between the motions of the diaphragms and the walls in the analysis.



**Figure 2–10. Plan of diaphragm.**

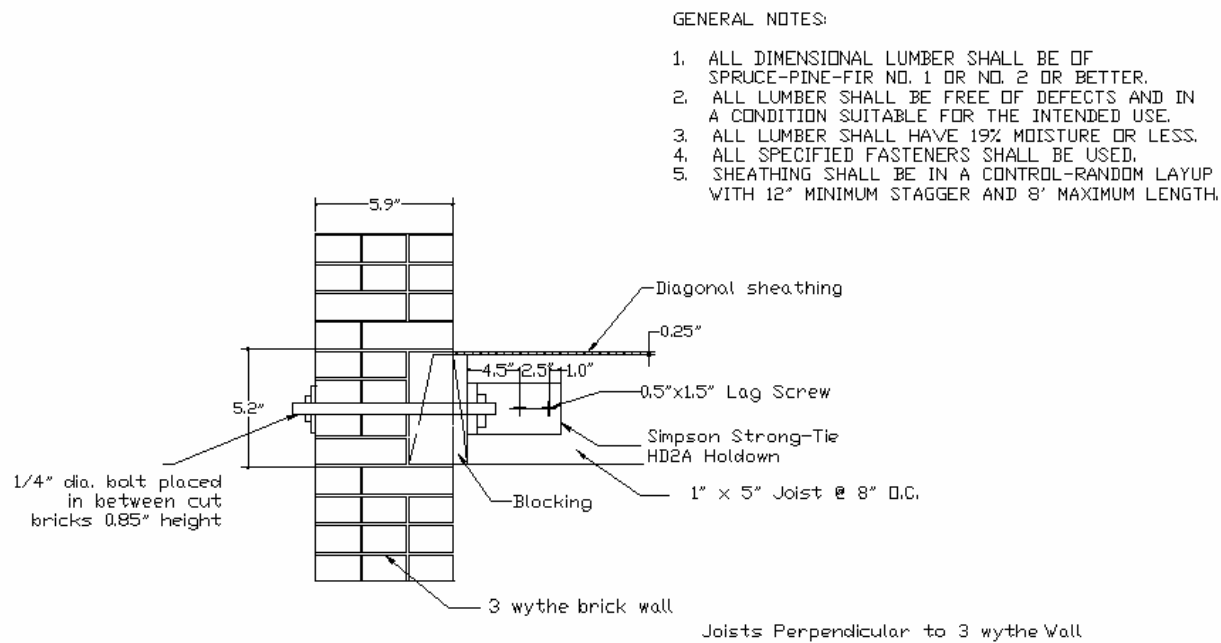


Figure 2-11. Connection detail.

## Material Properties

A circular saw was used to cut full-size common clay paver bricks measuring 7.625 x 3.625 x 2.125 in. into halves along each axis (Figure 2-12). Each paver produced eight half-scale bricks measuring approximately 3.75 x 1.75 x 1 in. after loss of about 1/8 in. of material in each cut due to kerf (Figure 2-13).



Figure 2-12. Cutting of half scale bricks.

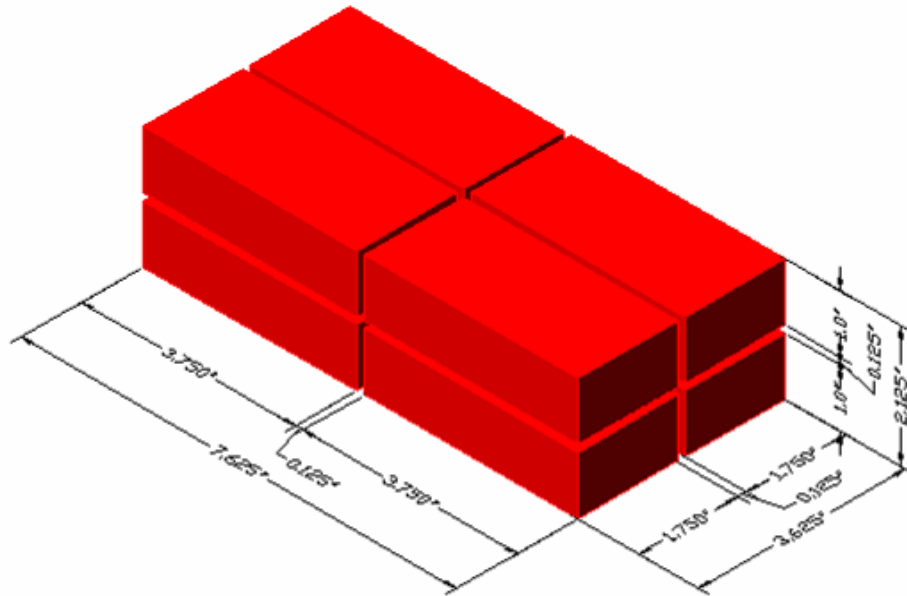


**Figure 2–13. Dissection of full scale brick into eight half scale bricks (units in inches).**

Ten half-scale bricks were tested to determine their actual size, initial rate of absorption (IRA), modulus of rupture, compressive strength, and modulus of elasticity using ASTM C 67 – 98a standard tests. The results are presented in Table 2-1.

**Table 2-1. Results of brick tests.**

Length	3.73	±	0.02	in
Width	1.78	±	0.03	in
Height	1.06	±	0.04	in
IRA	9.05	±	2.11	g/min/30 in <sup>2</sup>
Modulus of Rupture	0.633	±	0.087	ksi
Compressive Strength	15260	±	3145	psi
Modulus of Elasticity	44320	±	1134	ksi

Twenty prisms were built during the model construction phase. The prisms were tested using ASTM standard methods for flexural bond strength (E 518 – 00a), masonry bond strength (C1357 – 98a), and compressive strength (C 1314 – 98a). The results of the tests are given in Table 2-2. In addition to the prism tests, 10 mortar cubes were tested in accordance with ASTM C109/C109M-02. Pictures from the material tests are shown in Figure 2–14 through Figure 2–18.

**Table 2-2. Results of prism and mortar tests.**

Prism Compressive Strength	4.58	± 0.56	ksi
Prism Elastic Modulus	527.13	± 228.42	ksi
Mortar Compressive Strength	172.59	± 81.69	psi
Mortar Elastic Modulus	23.78	± 12.78	ksi
Prism Tensile Strength	79.09	± 12.59	psi
Prism Flexural Bond Strength	91.72	± 39.41	psi

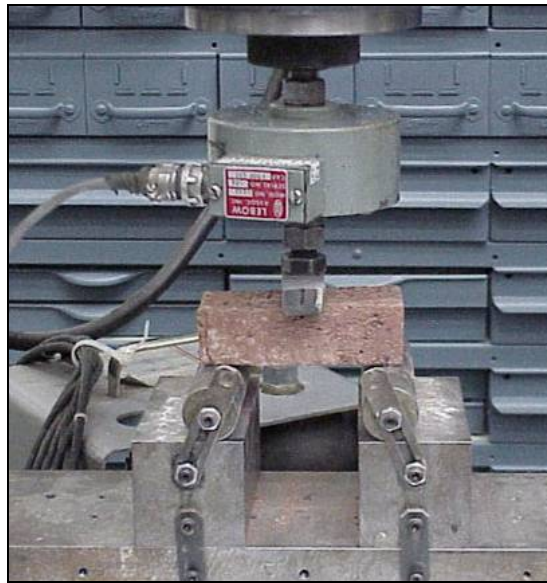
**Figure 2-14. Modulus of rupture test of individual brick.****Figure 2-15. Compression test of prism.**



Figure 2-16. Compression test of mortar cube.

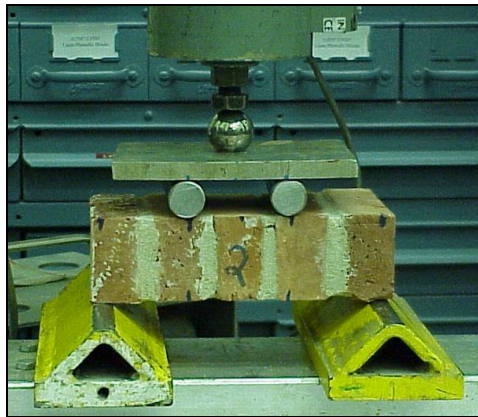


Figure 2-17. Flexure test of prism.

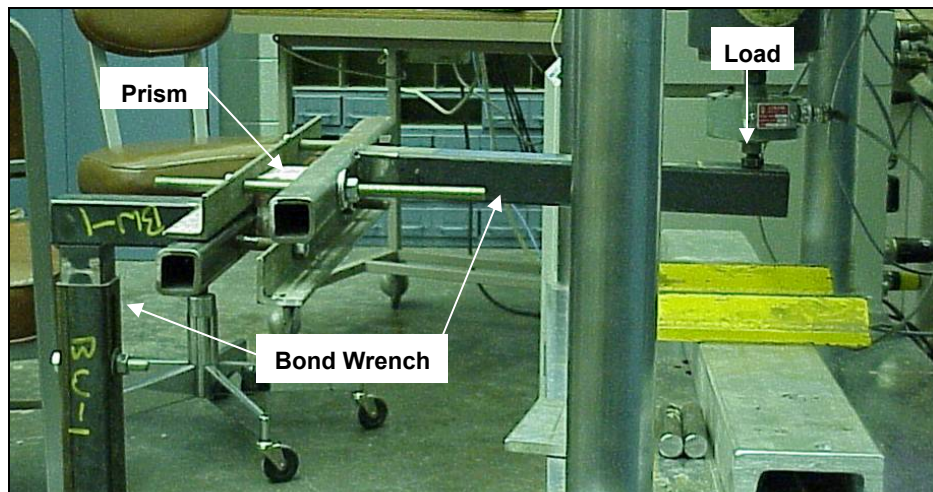


Figure 2-18. Bond wrench test of prism.

## Scaling

A common problem in reduced-scale testing is that not all properties can be scaled. For example, the half-scale test structure was constructed using half-scale bricks, but the bricks retain the same material properties (elastic modulus and density) as the full-scale bricks.

The scaling relationships inherent to the model are presented in Equation 2-1. When these relationships are applied to accurately scale the gravity stress, the result is Equation 2-2. Consequently, the gravity stress versus the material strength relationship is not constant if the densities of the two materials are the same (Harris 1999). This relationship is important for masonry construction because the lateral strength of the piers is based, in part, on vertical stress.

$$l_{model} = \frac{1}{2} l_{prototype} \quad E_{model} = E_{prototype} \quad \text{Equation 2-1}$$

$$\left( \frac{\gamma}{E} \right)_{model} = \left( \frac{\gamma}{E} \right)_{prototype} \quad \gamma_{model} = 2\gamma_{prototype} \quad \text{Equation 2-2}$$

In order to correctly model the prototype, the density of the bricks use in the half-scale model is half what it would be in a full-scale structure. Therefore, in order to effectively double the density of the brick, additional mass should be added throughout the volume of the walls. Unfortunately, uniform distribution of the additional mass was not feasible, so mass was added in a dispersed pattern on the wall faces and diaphragm.

As a consequence of scaling the gravity stress, the duration of the applied ground motions had to be divided by the square root of 2. This division is supported by the scaling relationships presented in the following equations:

$$\frac{f_{model}}{f_{prototype}} = \frac{\left( \sqrt{K/M} \right)_{model}}{\left( \sqrt{K/M} \right)_{prototype}} = \frac{\left( \sqrt{\frac{El^2/l}{\gamma^3}} \right)_{model}}{\left( \sqrt{\frac{El^2/l}{\gamma^3}} \right)_{prototype}} = \sqrt{2} \quad \text{Equation 2-3}$$

$$f = 1/T \quad \frac{T_{model}}{T_{prototype}} = 1/\sqrt{2} \quad \text{Equation 2-4}$$

With these scale factors determined, the model scaling factors for the remaining quantities could be determined. The results are shown in Table 2-3.

**Table 2-3. Scaling relationships.**

Quantity	Scale Factor ( $S_m/S_p$ )
Force	1/4
Stress	1
Acceleration	1
Velocity	1/√2
Time	1/√2
Frequency	√2
Length	1/2
Displacement	1/2
Modulus	1
Strain	1
Density	2

### ***Placement of Simulated Mass***

The actual weight of the test structure was 24 kilopounds (kips). In order to essentially double the density of the building, 21 kips of lead weights were added. All of the mass was placed outside of the first and second story piers in order to prevent interference with their behavior. That constraint meant the weights had to be located along the spandrels of the structure (Figure 2–19). Weights were placed on the interior and exterior of the walls in the same pattern, in terms of both location and mass distribution. Approximately 3.8 kips of lead weights were bolted to each wall using 1/4 in. threaded rods (two rods per weight set), which passed through holes cast in the wall's bed joints during construction. Each lead weight weighed an average of 59 lb.

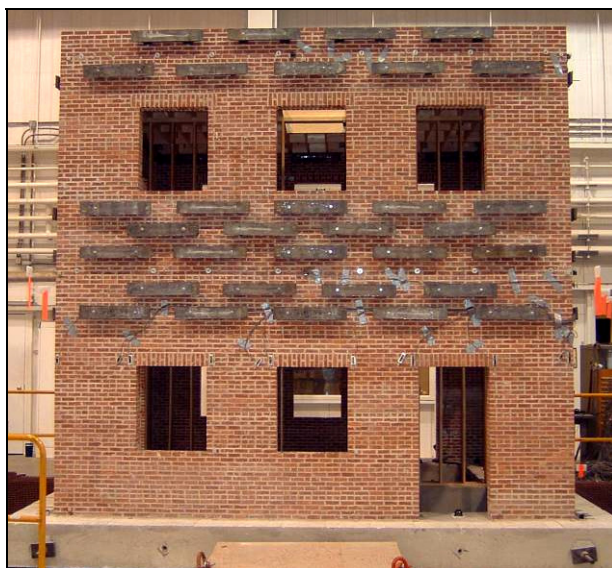


**Figure 2-19. Layout of additional weight on walls.**

In addition to the masses on the walls, the remaining lead weights were added to the perimeters of the diaphragms (Figure 2-20). The explanation for this approach is twofold and directly related to the behavior of a structure when the joists are unconnected to the walls. The primary reason was that a significant normal force was needed to determine an estimate of the frictional force developed in the joist pocket. The second reason was to provide the diaphragm with its own mass, allowing it to respond independently of the walls. Once the diaphragm was connected to the walls, the weights could be considered as tributary mass from the out-of-plane walls due to the forced continuity.

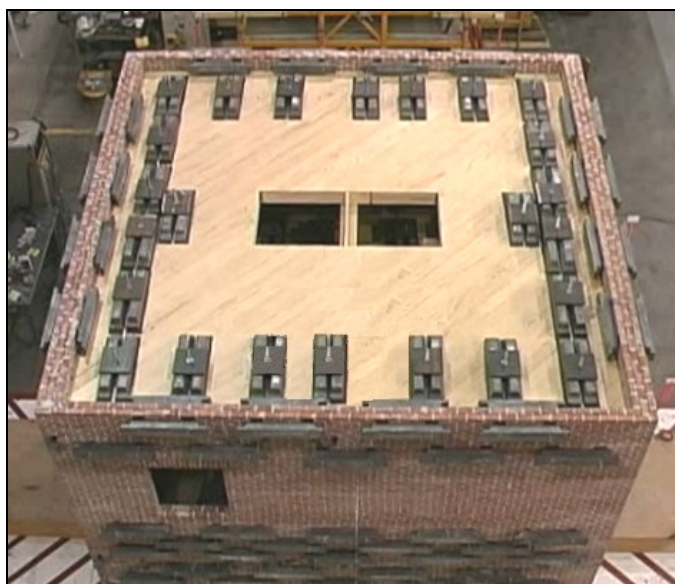


**Figure 2-20. Layout of additional weight on diaphragms.**

The weights were placed on the diaphragm such that they spanned two joists and applied no stress to the diagonal sheathing. In total, 3.0 kips were added to both the floor and roof diaphragms. Rubber pads were positioned below the weights to prevent movement during testing.

The additional weight concentrated around the spandrels rather than throughout the volume of the walls does not pose a serious analytical concern. This type of model is accurate while the material is in the elastic response range, so the expected crack patterns will not be affected by the location of the additional mass. In the inelastic range, the modeling of gravity stress does affect the accuracy of the model. However, the objective of the overall project was to study the global response characteristics and to evaluate the retrofit measures. Because the half-scale model is expected to have crack patterns similar to those occurring in the full-scale prototype, the response of the cracked model will have the same global characteristics as the full-scale prototype.

## **Base Girder**

The test structure was mortared to a concrete base girder, which was designed to support the model for its move onto the shake table. During testing, the girder remained stiff and acted as a rigid connection between the table and the building. The base girder (shown in Figure 2–21) has perimeter beams that are 1 ft thick and 2 ft-3 in. wide, with an additional interior beam 1 ft thick and 1 ft wide. The girder was fabricated of reinforced concrete and post-tensioned to provide additional strength during lifting of the test structure onto the shake table. The base girder was bolted to the shake table with 25 1.5 in. bolts.

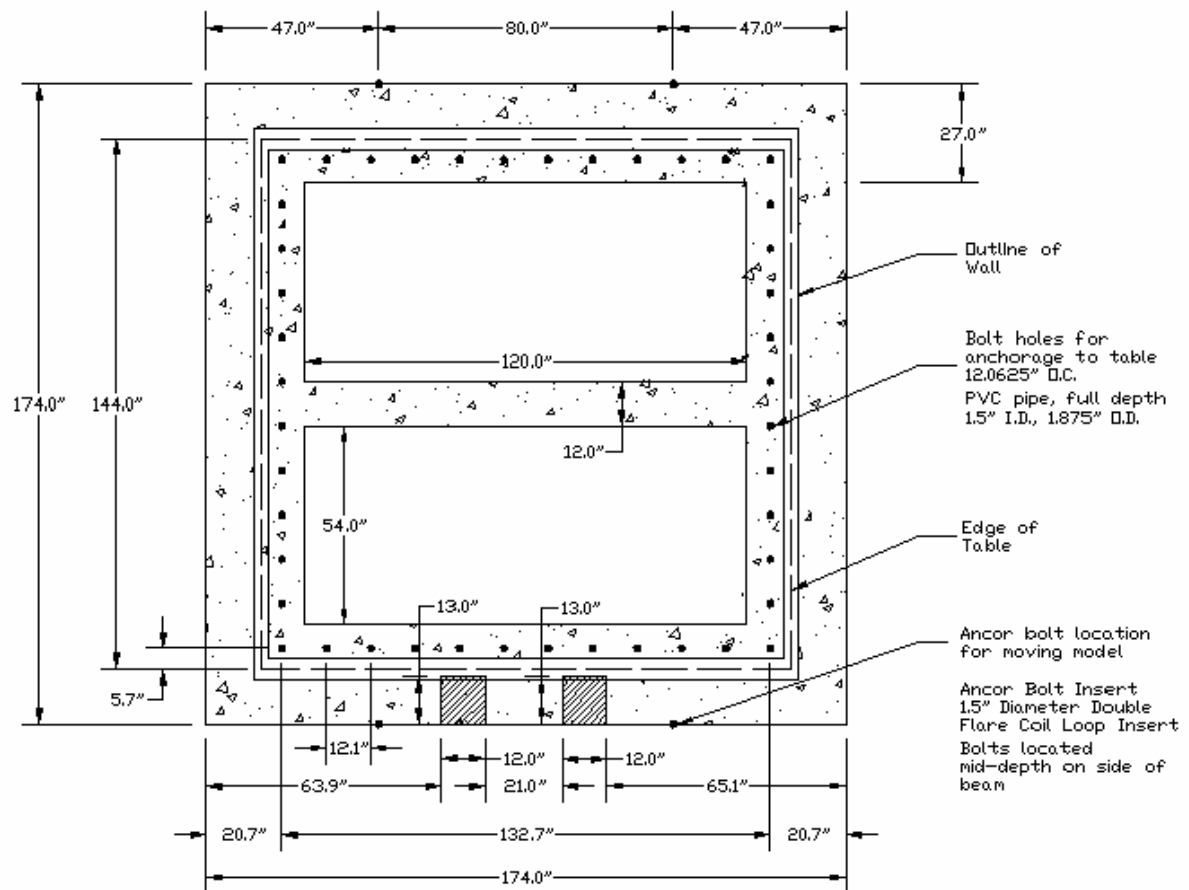


Figure 2-21. Layout of base girder.

## 3 Selection of Model Seismic Motions

### Ground Motions Considered

Three earthquake ground motion suites were considered as possibilities for the seismic testing of the half-scale model. They were the 1985 Nahanni earthquake, the 1940 El Centro earthquake, and the 1989 Loma Prieta earthquake. Below is a brief summary why each seismic event was considered. See Chapter 3 of Sweeney et al. (2004) for more information on the considered earthquakes.

#### Nahanni:

- intraplate earthquake; may be similar to one that could occur in the central United States
- has narrow frequency content at natural periods of the test model.

#### El Centro:

- widely used and well understood
- spectral accelerations near natural periods of test model are very different for horizontal components.

#### Loma Prieta:

- large spectral accelerations for horizontal components occur at different frequencies
- broad frequency content will excite multiple modes.

### Reasons for Selecting the Nahanni Earthquake

The combination of response quantities due to multidirectional excitation was considered to be of primary importance for the selection of the test motion. Due to the variation of dynamic behavior resulting from different forcing functions, the severity of combinational effects will differ for the three earthquakes under

consideration. Therefore, to aid in the selection of the test motion, extensive computer analyses were conducted to estimate the test structure's response. Chapter 4 of Sweeney et al. (2004) describes these analyses in detail, which include 2D equivalent static, 2D response spectrum, and 2D and 3D time-history analyses.

The results of those analyses predicted that peak responses in the horizontal directions occurred concurrently for the Nahanni earthquake, but did not occur at the same time for either the Loma Prieta or the El Centro earthquakes. The consequence of the combination is twofold. The first effect is that ground motion in a direction parallel to walls 1 and 2 creates twisting shears in walls A and B (due to the different stiffnesses of walls 1 and 2), the maximum of which directly combines with the maximum in-plane shear caused by the perpendicular ground motion component. Note that this fact contradicts the 100%-30% combination rule used to determine design loads prescribed in FEMA 368. The second consequence is that due to overturning moment, the walls in the test structure are subjected to maximum base shear and maximum tensile force at the same time. Because the lateral strength of a masonry pier is based in large part upon the compressive stress in the pier, this combination should have damaging effects on the building.

Upon selection of the Nahanni earthquake as the test motion, it also was decided to test only in the orthogonal plan directions. This decision was made because the analyses indicated that the vast majority of vertical tensions and compressions in the walls were caused by overturning forces, not vertical accelerations.

## Characteristics of the Nahanni Earthquake

The Nahanni time histories were downloaded from the PEER strong motion database web site (<http://peer.berkeley.edu/smcat/>). In accordance with the scaling factors presented in Chapter 2, the time histories were multiplied by  $1/\sqrt{2}$ . The modified time histories for the x-direction and y-direction are shown below in Figure 3-1 and Figure 3-2, respectively (see Figure 2-6 for coordinate system). Using the modified time histories, response spectra were generated for an assumed damping ratio of 5%. The response spectra for the x-direction and y-direction are shown below in Figure 3-3 and Figure 3-4, respectively.

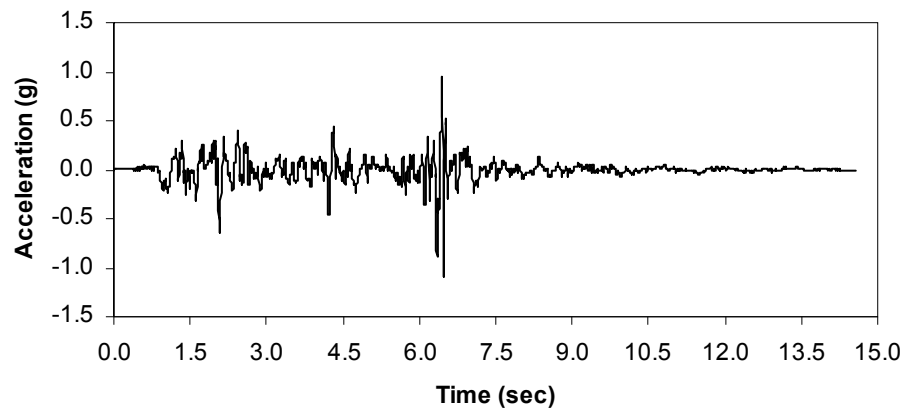


Figure 3-1. Modified Nahanni x-direction time history (walls A and B in-plane).

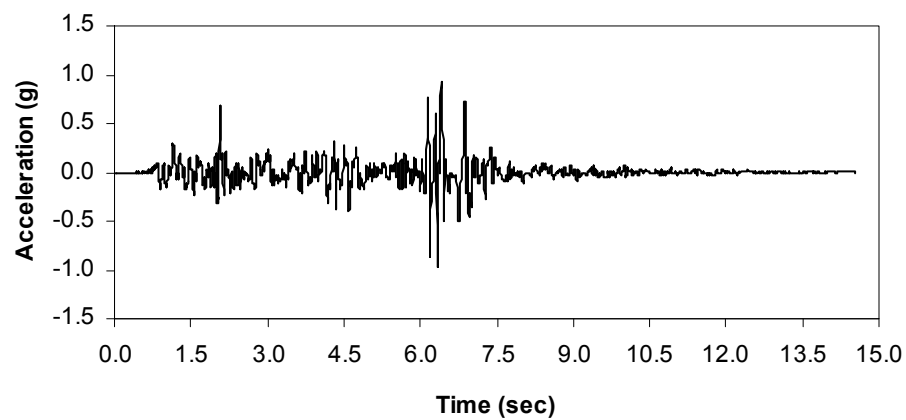


Figure 3-2. Modified Nahanni y-direction time history (walls 1 and 2 in-plane).

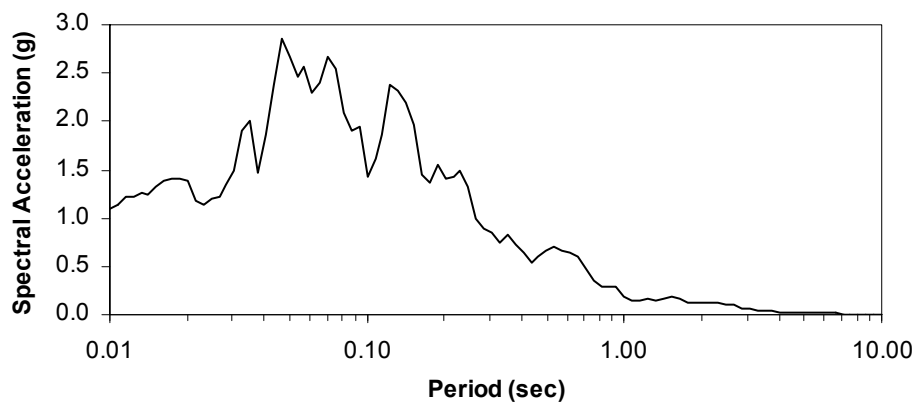


Figure 3-3. Modified Nahanni x-direction acceleration response spectrum for 5% damping.

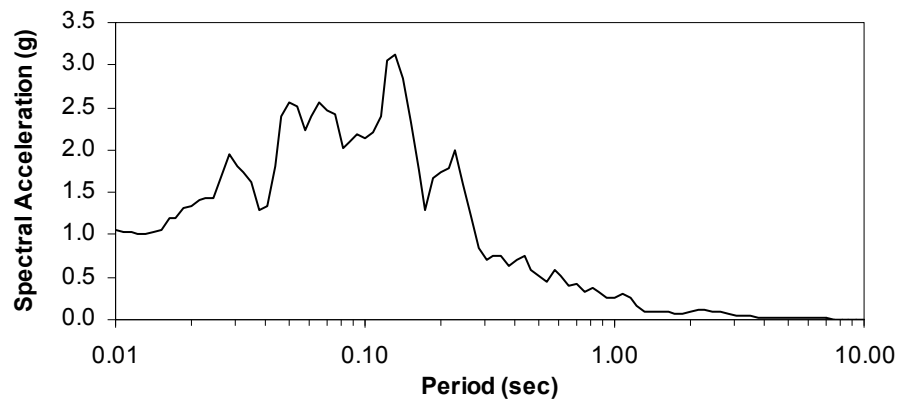


Figure 3–4. Modified Nahanni y-direction acceleration response spectrum for 5% damping.

## 4 Expected Building Response

Analyses were performed to predict the response of the half-scale test model. In particular, the expected behavior of the masonry piers was examined per FEMA 356 specifications and the stiffness of the wood diaphragms was estimated based on a number of code equations for predicted in-plane deflection. The results from the component analyses were applied to the development of a 3D finite element model in SAP 2000 Nonlinear, which was used to predict the test structure's force/deformation properties, fundamental frequencies, and dynamic response to the Nahanni earthquake.

### Independent Pier Behavior

The possible pier failure modes and failure strengths are examined according to the prescriptions of FEMA 356. Based on the predicted failure mode, the deformation response of each pier was determined.

#### ***Failure Mode and Strength Calculations***

An important part of seismic analysis of a masonry structural system is determining the lateral behavior of the constituent piers. Piers are the structural elements of a masonry wall and are designed to carry the demands of both vertical and lateral loads. They generally can be identified as the continuous portions of a wall located on either side of openings such as windows or doors. Consequently, there can be many piers in a perforated shear wall (see Figure 4–1), but a solid wall, having no openings, behaves as a single pier. The response of individual piers can be combined to help determine the behavior of an individual wall or the entire building.

The *Prestandard and Commentary for the Seismic Rehabilitation of Buildings* (FEMA 356) provides a straightforward method to determine the lateral force/deformation relationship of masonry piers. The prestandard is a prescriptive method similar to most building codes and is comparable to what is used in practice. FEMA 356 was used during the design phase of this project to ensure that the desired structural response would occur.

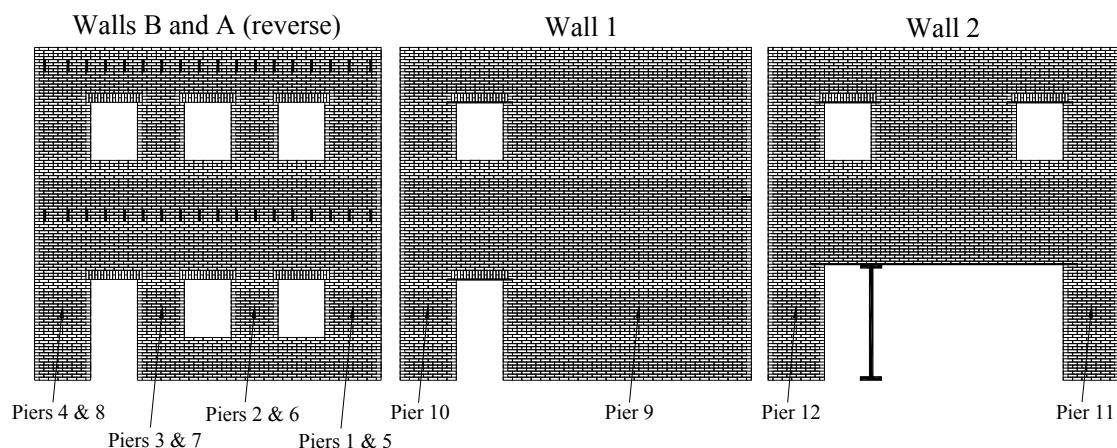


**Figure 4-1. Pier numbers.**

The lateral behavior of a masonry pier before yielding is linear-elastic, and can be identified as the initial straight line portion of the load/deflection curve (see Figure 4-2). At the onset of yield, a failure mechanism occurs, causing increased deflections and loss of resistance. The slope of the load/deflection curve in the linear-elastic region represents the elastic stiffness of the pier.

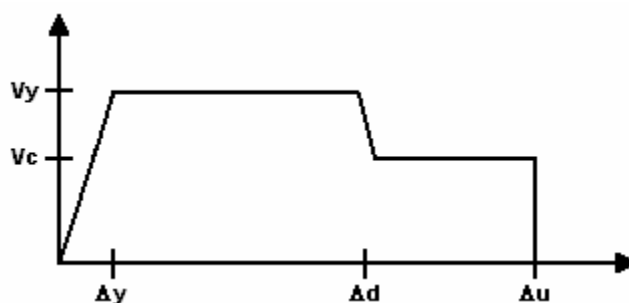


**Figure 4-2. Force/deformation curve for masonry piers per FEMA 356.**

FEMA 356 presents two formulations to calculate the stiffness of a pier — the first for cantilevered walls and the second for piers that have full restraint against rotation at the top and bottom. They are presented below as Equation 4-1 and Equation 4-2, respectively:

$$k_{pier} = \frac{1}{\frac{h_{eff}^3}{3E_m I_g} + \frac{h_{eff}}{A_v G_m}} \quad \text{Equation 4-1}$$

$$k_{pier} = \frac{1}{\frac{h_{eff}^3}{12E_m I_g} + \frac{h_{eff}}{A_v G_m}} \quad \text{Equation 4-2}$$

where

$h_{eff}$  = pier height to the point of lateral load

$E_m$  = masonry elastic modulus

$A_v$  = effective shear area (assumed to be 5/6 of the gross area)

$I_g$  = moment of inertia of the uncracked pier cross-section

$G_m$  = shear modulus (assumed to be  $0.4E_m$ ).

The values for stiffness of the piers are presented in Table 4-1.

**Table 4-1. Pier force/deformation behavior.**

Pier (wall)	$k_{pier}$ (k/in)	$V_{crack}$ (kip)	$V_y$ (kip)	$\Delta y$ (in)	$\Delta d$ (in)	$V_c$ (kip)	$\Delta u$ (in)
1 (A)	699.68	3.417	3.105	0.00444	0.1009	1.863	0.2017
2 (A)	523.34	2.373	2.156	0.00412	0.1210	1.294	0.2421
3 (A)	523.34	2.373	2.156	0.00412	0.1210	1.294	0.2421
4 (A)	263.58	1.981	1.831	0.00695	0.3053	1.098	0.6106
5 (B)	699.68	3.417	3.105	0.00444	0.1009	1.863	0.2017
6 (B)	523.34	2.373	2.156	0.00412	0.1210	1.294	0.2421
7 (B)	523.34	2.373	2.156	0.00412	0.1210	1.294	0.2421
8 (B)	263.58	1.981	1.831	0.00695	0.3053	1.098	0.6106
9 (1)	144.48	3.513	2.513	0.01740	0.7545	1.508	1.5090
10 (1)	176.93	1.163	0.779	0.00441	0.3053	0.468	0.6106
11 (2)	131.49	1.370	1.648	0.01254	0.4051	0.989	0.8102
12 (2)	131.49	1.370	1.648	0.01254	0.4051	0.989	0.8102

The lateral strength of piers in unreinforced masonry walls depends on the mode of failure. FEMA 356 recognizes four different types of failure: bed-joint sliding, rocking, diagonal tension, and toe crushing. The strength calculations for each mode, Equations 7-3 – 7-6 in FEMA 356, are discussed below

*Bed-joint sliding* failure occurs when the shear stress along the base of the pier ( $f_v$  in Figure 4-3) is greater than the shear strength. When the shear strength is reached a crack forms along the length of the bed-joint and the pier begins to slide. The bed-joint sliding strength,  $V_{bjs}$ , is given below as Equation 4-3:

$$V_{bjs} = v_{me} A_n \quad \text{Equation 4-3}$$

where

$v_{me}$  = bed-joint sliding shear strength

$A_n$  = net area of the mortared section.

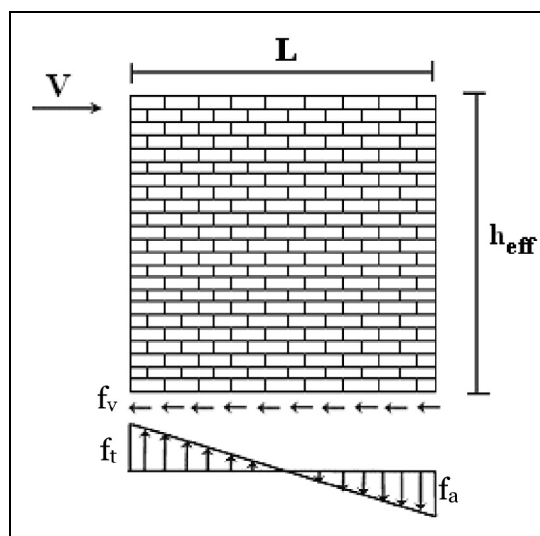


Figure 4–3. Forces on free standing pier.

The *rocking* mode of failure occurs when a crack forms at the bottom of the pier (both top and bottom for a fixed-fixed case), allowing it to rock laterally. The crack forms when the tensile stress ( $f_t$  in Figure 4–3) becomes greater than the axial compressive stress plus tensile strength of the masonry. This occurs when the lateral load is:

$$V_{crack} = \frac{L^2 t}{6 h_{eff}} (f_a + f_t) \quad \text{Equation 4-4}$$

where

$L$  = pier length

$f_a$  = axial compressive stress

$f_t$  = tensile strength of masonry

$t$  = thickness.

This equation specifically applies to a cantilevered pier, as is shown in Figure 4–3. For a fixed-fixed case, multiply Equation 4-4 by 2.

Once cracks have sufficiently formed over the length of the pier, the rocking strength is reached (Equation 4-5). The formula for determining rocking strength is a function of the expected axial compressive force ( $P_E$ ), the ratio of the pier length ( $L$ ) to the effective height of the pier ( $h_{eff}$ ), and a factor  $\alpha$  equal to 0.5 for a fixed-free cantilevered wall and 1.0 for a fixed-fixed pier:

$$V_r = 0.9\alpha P_E \left( \frac{L}{h_{eff}} \right) \quad \text{Equation 4-5}$$

*Diagonal tension* failure is characterized by X-cracks through the wall or pier caused by internal stresses. If the cracks pass through the mortar in a stair step pattern, the strength of the pier is the same as the bed joint sliding strength of Equation 4-3. However, if the cracks propagate diagonally through the mortar and the bricks, the strength is given by Equation 4-6:

$$V_{dt} = f'_{dt} A_n \left( \frac{L}{h_{eff}} \right) \sqrt{1 + \frac{f_a}{f'_{dt}}} \quad \text{Equation 4-6}$$

where  $f'_{dt}$  is the lower-bound masonry diagonal tension strength and  $f_a$  is the lower-bound axial compressive stress.

*Toe crushing* is the failure of the bricks and mortar at the corners of the pier due to the additional compressive stresses of the overturning moment ( $f_a$  in **Error! Reference source not found.**). Toe crushing strength is determined using Equation 4-7:

$$V_{tc} = \alpha P_L \left( \frac{L}{h_{eff}} \right) \left( 1 - \frac{f_a}{0.7 f'_m} \right) \quad \text{Equation 4-7}$$

where  $f'_m$  is the lower-bound masonry compressive strength and the ratio of  $L/h_{eff}$  shall not be taken less than 0.67.

The FEMA 356 equations were used to determine the lateral strength of the piers in the test structure. The results are presented in Table 4-2, using the pier numbers shown in Figure 4-1 (piers 1 – 4 are associated with wall A). For these calculations  $v_{me}$  was assumed to be 35.1 psi and  $f'_{dt}$  to be 27 psi in accordance with the default properties in Section 7.3.2.10 of FEMA 356. Furthermore,  $f'_m$  was calculated to be 2,862 psi by taking the prism compression strength presented in Chapter 2 and dividing by 1.6, as prescribed by Section 7.4.2.2.2 of FEMA 356. The remainder of the pier properties used in the strength equations were calculated based on the actual dimensions of the test structure and a structural weight equal to 20 psf per wythe.

Table 4-2. Pier lateral strengths based on FEMA 356.

Pier (wall)	L (in)	$h_{eff}$ (in)	$V_{bjs}$ (kip)	$V_r$ (kip)	$V_{dt}$ (kip)	$V_{tc}$ (kip)
1 (A)	24	24.6	4.89	3.11	5.12	3.41
2 (A)	20	24.6	4.08	2.16	3.55	2.37
3 (A)	20	24.6	4.08	2.16	3.55	2.37
4 (A)	24	42.8	4.89	1.83	2.96	2.40
5 (B)	24	24.6	4.89	3.11	5.12	3.41
6 (B)	20	24.6	4.08	2.16	3.55	2.37
7 (B)	20	24.6	4.08	2.16	3.55	2.37
8 (B)	24	42.8	4.89	1.83	2.96	2.40
9 (1)	106	141.4	14.51	2.51	10.81	2.77
10 (1)	24	42.8	3.29	0.78	1.80	1.03
11 (2)	24	49.3	3.29	1.65	1.94	2.47
12 (2)	24	49.3	3.29	1.65	1.94	2.47

The results of the analysis indicate that all of the first-story piers should fail by rocking, although the toe crushing strengths are only slightly larger. The second-story pier strengths are not reported because they will not receive enough inertial force to cause damage. Thus, the building is considered to be essentially rigid above the first-story piers.

### Deformation Response of Piers

Thus far, only the strength of the piers under lateral load has been considered. Of equal importance is the pier deformation response, which is shown in Figure 4-2. In the figure,  $V_y$  is the minimum strength from Table 4-2, and  $\Delta y$  is determined by dividing  $V_y$  by  $k_{pier}$  of Equation 4-1 and Equation 4-2, as appropriate. For a given failure mode, FEMA 356 specifies the equations used to determine  $\Delta d$ ,  $\Delta u$ , and  $V_c$ . For a rocking pier, these values can be computed using Equation 4-8 through Equation 4-10:

$$\Delta d = 0.4 h_{eff}^2 / 100L \quad \text{Equation 4-8}$$

$$\Delta u = 0.8 h_{eff}^2 / 100L \quad \text{Equation 4-9}$$

$$V_c = 0.6V_y \quad \text{Equation 4-10}$$

These equations yield the results for the force/deformation relationships in Table 4-1.

The lateral behavior of individual piers can be combined to determine the lateral behavior of the wall or the whole building. Such combinations are discussed in later in this chapter.

## Diaphragm Behavior

A *diaphragm* is defined as a floor or roof that carries in-plane forces. The diaphragm distributes the in-plane forces caused by its own mass and the mass of the out-of-plane walls to the vertical lateral load resisting elements. The distribution of force to the lateral resisting elements (in-plane walls) depends on the characteristics of the diaphragm.

Two basic types of diaphragm behavior are possible depending on the relative rigidity between it and the walls. If the deformation of the diaphragm is insignificant compared with that of the walls, the diaphragm is considered to be *rigid*. A rigid diaphragm forces the walls to move together as a unit, thus distributing lateral load in proportion to the walls' stiffness. The other type of diaphragm behavior is *flexible*, and it occurs where wall deformation is insignificant compared with that of the diaphragm. When the diaphragm is flexible, the walls will resist lateral forces based on the amount of tributary mass they carry, just as a beam would distribute its load between two supports. Examples of rigid and flexible cases are concrete and wood diaphragms, respectively. Because the test structure has flexible diaphragms, each wall will receive in-plane lateral forces proportional to their vertical compressive stress and the demands of the attaching out-of-plane walls.

In addition to distributing forces, diaphragms also affect building behavior by their in-plane stiffness. The in-plane stiffness of a wood diaphragm is influenced by the type of sheathing, size and amount of fasteners (nails), and the existence of perimeter chords (FEMA 356). Unfortunately, the in-plane stiffness of wood cannot be predicted by simple analysis due to the complex mechanisms that contribute to their flexibility, namely, the behavior of the nails (Cohen 2001). There have been several attempts to come up with a simple equation to predict the in-plane deflection of the diaphragm. They are presented here in order to exhibit limiting bounds for the actual diaphragm deflection.

The lateral behavior of a wood diaphragm is described in code by the National Design Specification (NDS) for Wood Construction. They propose that the lateral deflection of a wood structural panel diaphragm ( $d$  in Figure 4–4) under uniform lateral load is:

$$d = \frac{5vL^3}{8EAb} + \frac{vL}{4Gt} + 0.188Le_n + \frac{\sum(\Delta_c X)}{2b} \quad \text{Equation 4-11}$$

where  $d$  is the mid-span deflection,  $v$  is the maximum shear,  $L$  is the diaphragm length,  $A$  is the chord cross-sectional area,  $b$  is the diaphragm width,  $t$  is the diaphragm thickness, and  $e_n$  is the nail deformation/slip. The first term in the equation represents the diaphragm deflection due to bending, the second due to shear, the third due to nail deformation or slippage, and the fourth due to chord splice slip. The first two terms evolve from simple bending and shear analysis. The nail deformation term is generally far greater than the others and is also the most difficult to accurately determine.

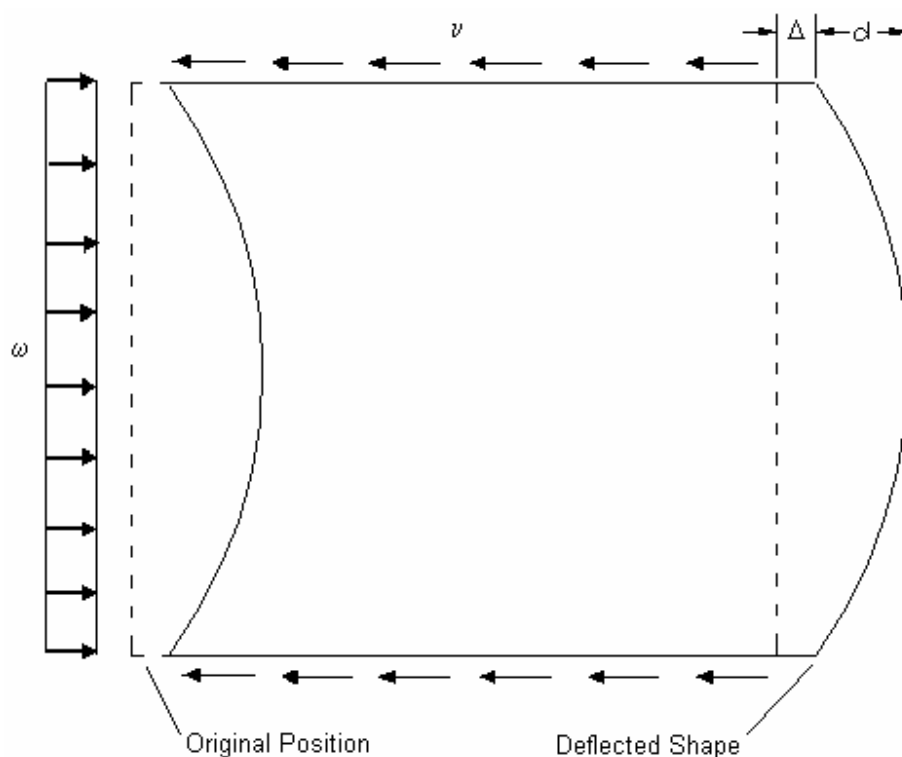


Figure 4-4. Deflection of diaphragm.

FEMA 356 also presents a similar equation for diaphragm deflection. However, it makes a distinction between plywood diaphragms and diagonally sheathed diaphragms. For a single diagonal sheathed diaphragm, the lateral deflection  $d$  is:

$$d = \frac{vL}{2G_d} \quad \text{Equation 4-12}$$

where  $G_d$  is given as 8,000 lb/in. The FEMA 356 equation essentially incorporates all the terms in the NDS equation into one term and defines  $G_d$  based on the general characteristics the diaphragm. FEMA defines a typical single diagonal sheathed diaphragm as 1 in. thick sheathing laid at 45 degrees to the framing members and nailed with two or more 8d nails per board at each support.

Finally, Cohen (2001) developed with a stiffness equation for the diaphragm he tested (similar to the one in this study) based on dynamic analysis. He determined that the stiffness of the diaphragm is:

$$K = A'G \frac{\pi^2}{2L} \quad \text{Equation 4-13}$$

where  $A'G$  was calculated to be 1,300 kip based on experimental data. Therefore, the deflection can be determined using:

$$d = V/K \quad \text{Equation 4-14}$$

where  $V$  is the total diaphragm shear. It is important to note that the calculated  $A'G$  value is derived for the diaphragm used in the tests (22 x 4.67 ft, 4d nailing, and 3/8 in. thick). However, the diaphragm used in this study is similar enough to the one used in Cohen 2001 that a conversion factor based on the width of the diaphragm can be used. Cohen states that  $A'G$  is proportional to diaphragm width. Therefore, to convert the  $A'G$  value from that for the tested 4.67 ft wide diaphragm to that for a different width, multiply by the ratio of the new diaphragm width to 4.67 ft. Therefore, for the diaphragm in this study,  $A'G$  would equal 3,340 kip.

These equations were then used on Cohen's diaphragm under 2,500 lb of shear to determine their relative accuracy. As seen from Table 4-3, the FEMA equation over-predicts the actual diaphragm deflection while the NDS equation is much more accurate even though it is supposed to be for a different type of diaphragm. Calculations were also made for the 12 x 12 ft diaphragm used in this study under 4,000 lb of shear. Based on the data, the deflection of the diaphragm under 4,000 lb of shear should range between 0.035 – 0.125 in. For other values of shear, the deflection should be between the Cohen and FEMA calculated values. This approximated stiffness results in a diaphragm frequency of 8.8 – 16.7 Hz.

**Table 4-3. Diaphragm deflections (inches).**

	<b>22'x 4.67'</b>	<b>12'x12'</b>
NDS	0.116	0.060
FEMA	0.368	0.125
Cohen	0.100	0.035
Actual	0.120*	

Note: measured diaphragm deflection includes the deflection of the in-plane shear walls.

Accurate calculation of diaphragm deflection is important because the out-of-plane displacement of the walls is largely controlled by the lateral displacement of the diaphragm. The more the diaphragm deflects, the more the out-of-plane walls will have to deform (Simsir 2001). Out-of-plane wall failures, as noted previously, are common in URM buildings, but many times it can be prevented by ensuring that there is a sound connection between the diaphragm and the walls.

### **Force/Deformation Response of Structure (Pushover Analysis)**

A pushover analysis consists of a nonlinear model of a structure that is subjected to increasing levels of lateral load. A nonlinear model differs from a linear model because it can account for the redistribution of forces due to yielding. The result of the analysis is a pushover curve, in which the total base shear applied to the structure is plotted versus a chosen “control displacement” at each load increment. The selected control point is usually located at the top of the structure. This analysis allows for the determination of the force/deformation characteristics of the structure as well as the damage states for various levels of base shear. The method is presented in FEMA 368 as “Appendix to Chapter 5.”

To perform a pushover analysis, one must specify the nonlinear load-deformation response of each structural element that could potentially yield. In Chapter 3, the nonlinear behavior of individual piers was found based on FEMA 356, and the information was used to assign hinge properties for models created in SAP 2000NL. The lateral pushover loads applied were proportional to the first mode of each wall for the 2D cases and to the fundamental mode of the structure in each horizontal direction for the 3D cases, per FEMA 368 specifications. In addition, the SAP pushover analyses included the dead load of the test model and P-delta effects.

The results from the SAP 2D analyses are shown in Figure 4–5 through Figure 4–7. Also shown on the figures is the combined pier response (designated as

FEMA), calculated by adding the load/deformation relationships for each of the first-story piers for a given wall (the second-story piers are assumed to not yield). Note that the displacement plotted from SAP is generated at the joint located at the top of the first-story piers at the edge of the wall under consideration. For wall 1, this is the height of the building since pier 9 is considered to be a cantilevered pier. If the SAP pushover analyses for walls A, B, and 2 were plotted based on the displacement of a point at the top of the building, the deformation would be somewhat larger due to global overturning moment. As can be seen from the figures, the combined pier response closely matches the results from the pushover analyses.

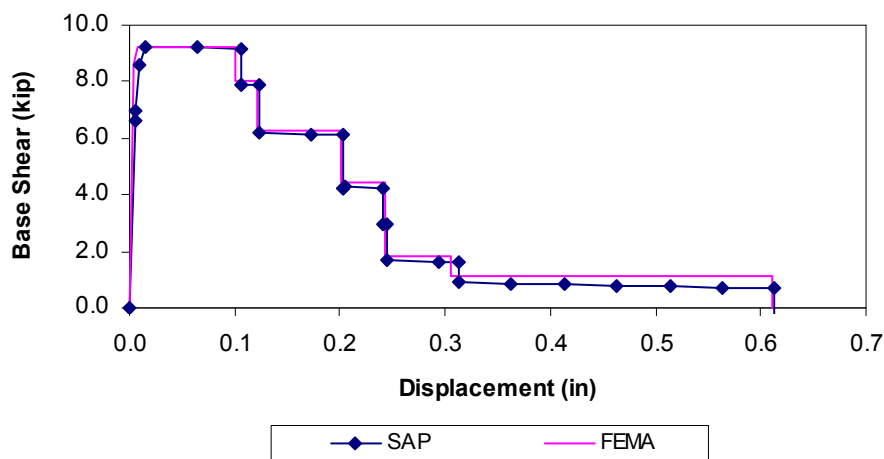


Figure 4-5. Force/deformation relationships for walls A and B.

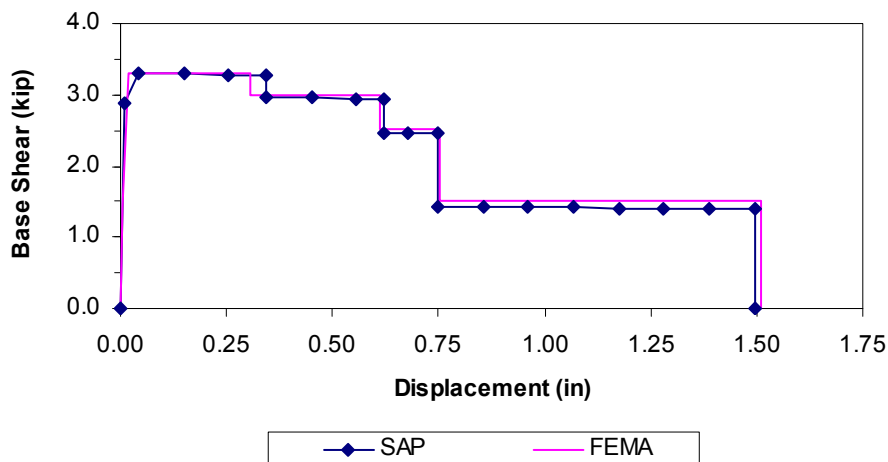


Figure 4-6. Force/deformation relationship for wall 1.

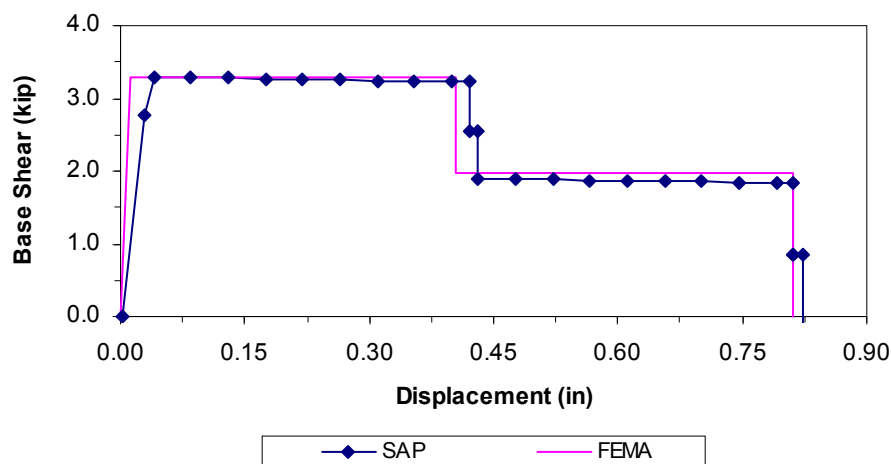


Figure 4-7. Force/deformation relationship for wall 2.

Section 5A.1.1 of FEMA 368 states that “for structures having plan irregularities... or structures without independent orthogonal systems, a three-dimensional model incorporating a minimum of three degrees of freedom, consisting of translation in two orthogonal plan directions and torsional rotation...shall be used.” Using FEMA 368, the test model would require analysis using a 3D model. A 3D model of the test structure was created and, in accordance with Section 5A.1.2, pushover analyses were performed in both horizontal directions. The results of the 3D pushover analyses are plotted below with the combined SAP 2D wall pushovers (Figure 4-8 and Figure 4-9). The pushover curves for the 3D cases were determined by averaging the response at the tops of the two in-plane walls for the direction under consideration.

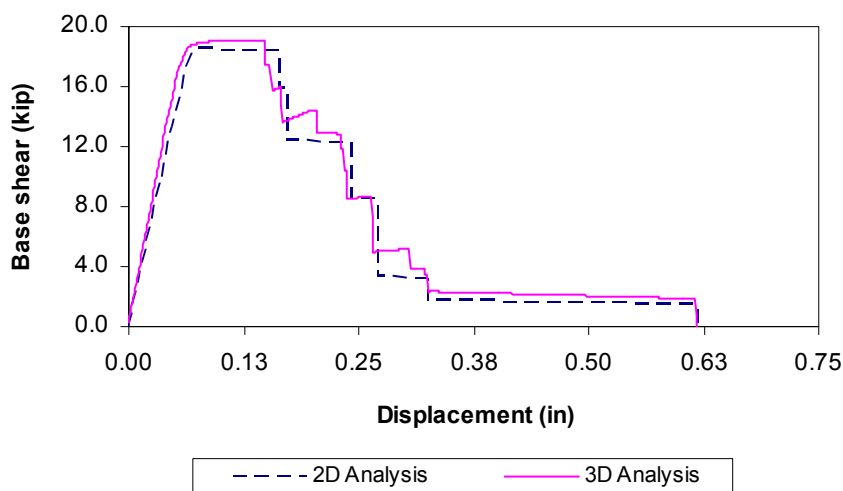
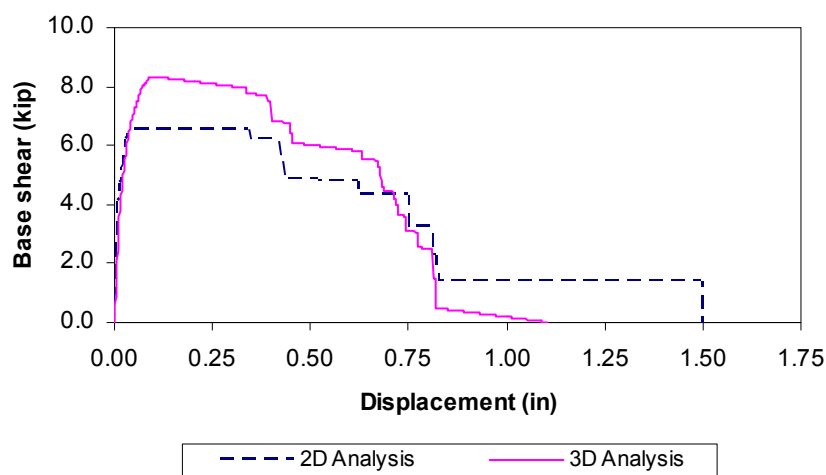


Figure 4-8. Comparison of 2D and 3D pushover curves for walls A and B.



**Figure 4–9. Comparison of 2D and 3D pushover curves for walls 1 and 2.**

As would be expected, the 3D pushovers exhibit increased strength. This effect is due to the behavior of the out-of-plane walls, which is usually neglected for masonry design. For the pushovers shown above, the out-of-plane strength of the masonry piers was specified in SAP to be one-tenth the in-plane strength. Since the combined in-plane strength of walls A and B is about three times larger than that of walls 1 and 2, the effect of the out-of-plane walls is considerably more pronounced for loading in the 1-2 plane direction.

A predominant feature of the 3D pushover curve for walls 1 and 2 is a reduced deformation capacity compared with that of the 2D response. This behavior is a result of the P-delta effect, or a magnification of the overturning moment caused by lateral deflection of the structure. As the building translates, the downward force due to its own mass becomes eccentric to its base, producing a moment that combines with that caused by the lateral force. While both the 3D and 2D analyses include P-delta effects, the additional mass from the diaphragm and out-of-plane walls in the 3D model results in a much greater amplification. The weight of the building is just one of two contributing factors in evaluating the severity of P-delta effects, however. If the displacement of the structure is small enough, the effect will be minimal regardless of the vertical compressive force; such is the case for walls A and B. Figure 4–10 and Figure 4–11 each show the 3D pushover curves for both horizontal directions, with a curve that includes P-delta effects and a curve that neglects P-delta effects.

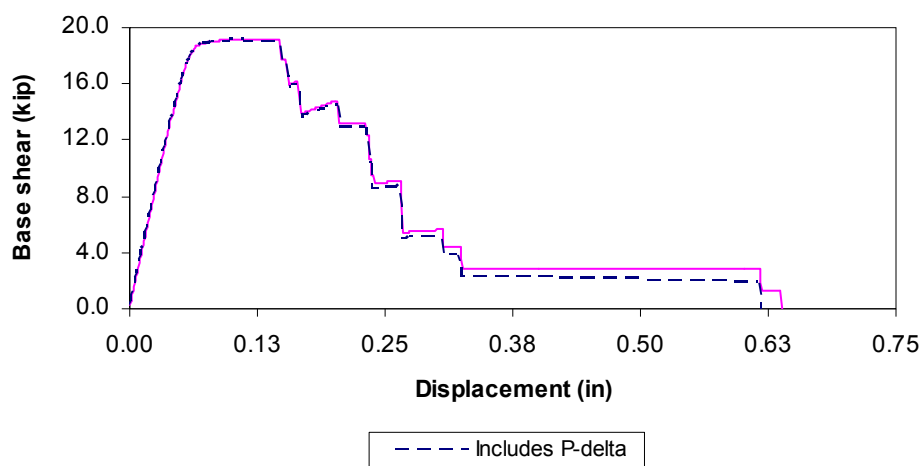


Figure 4-10. P-delta effects for A-B plane direction.

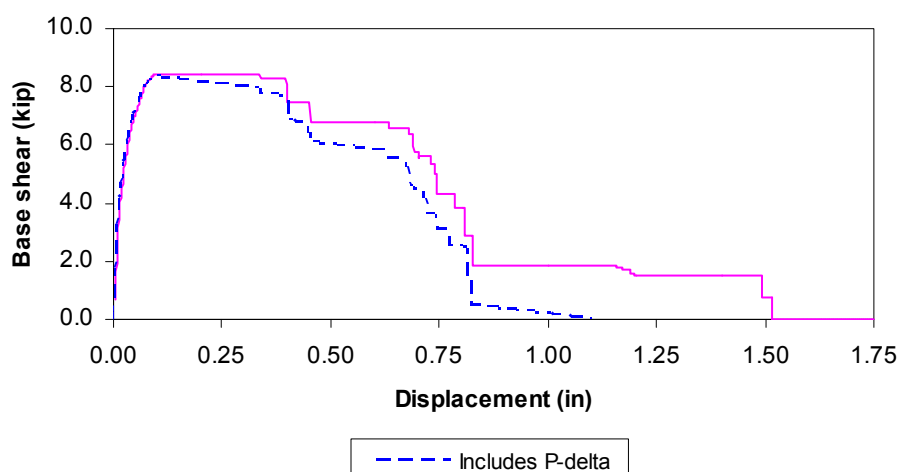
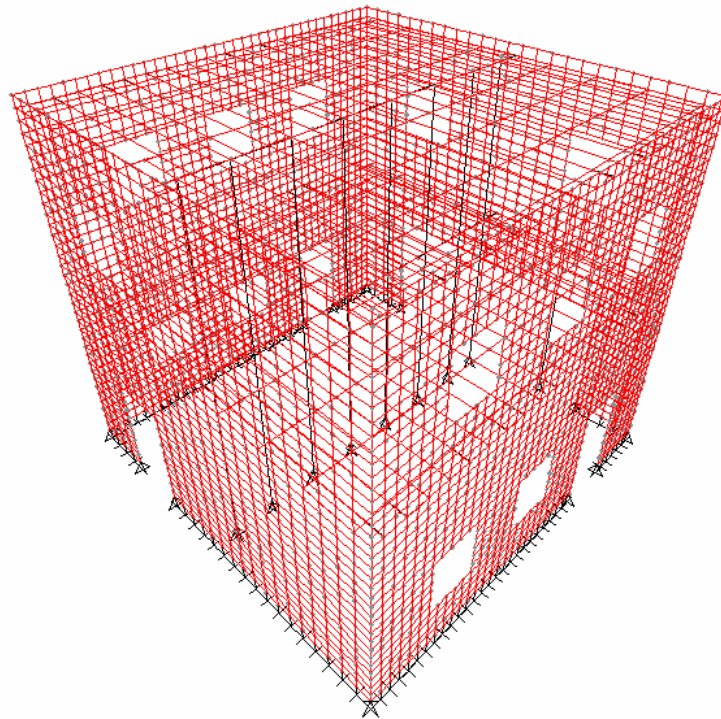


Figure 4-11. P-delta effects for 1-2 plane direction.

## Building Mode Shapes and Frequencies

A 3D finite element model was created in SAP 2000NL (Figure 4-12) in order to predict the dynamic characteristics of the building in addition to the response of the test structure to the Nahanni earthquake. The walls of the model were constructed of shell elements and assigned the experimental material properties presented in Chapter 2. The number of shell elements ensures geometric conformity and an accurate description of the response characteristics of the building. The diaphragms of the model were constructed of shell elements representing the diagonal sheathing and frame elements were used to represent the joists

and stud walls. The diaphragm was calibrated to obtain deflection characteristics in agreement with the results from Chapter 3 by reducing the thickness of the shell element (diaphragm thickness) to 0.0625 in.



**Figure 4–12. 3D finite element model created in SAP 2000NL.**

SAP 2000NL automatically calculates the building's mode shapes and frequencies for any dynamic analysis. The periods and mode shapes for the test model's first four modes are shown below in Figure 4–13 through Figure 4–16. The first two modes are the fundamental translational modes in the horizontal plan directions. The mode associated with walls 1 and 2 has a longer period than the mode associated with walls A and B because the structure is considerably less stiff in the 1-2 plane direction. The third and fourth modes are characterized by the out-of-phase response of the floor and roof diaphragms. Since walls A and B have a higher stiffness in bending than walls 1 and 2, in-plane diaphragm response in the A-B plane direction occurs at a longer period than in the 1-2 plane direction.

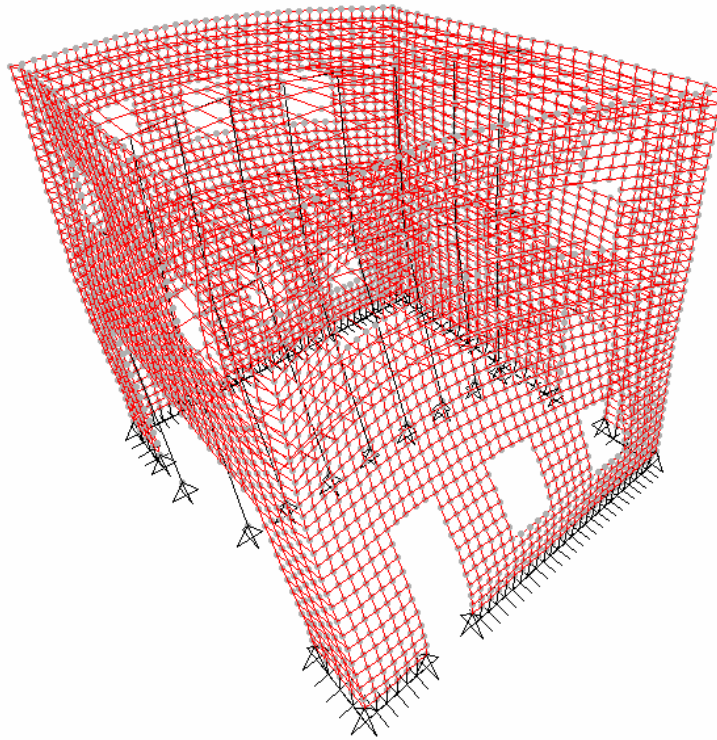


Figure 4–13. First-mode shape of test structure, period of 0.096 sec.

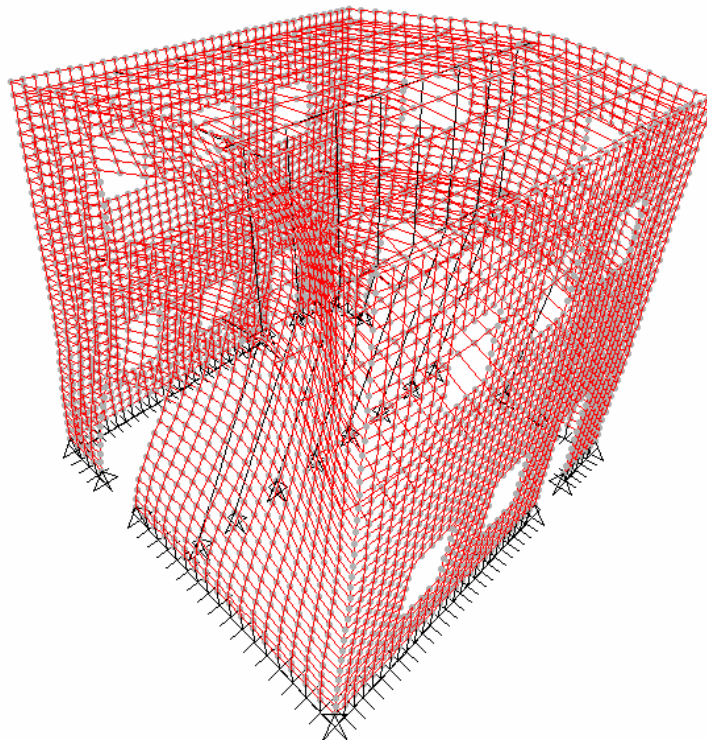


Figure 4–14. Second-mode shape of test structure, period of 0.086 sec.

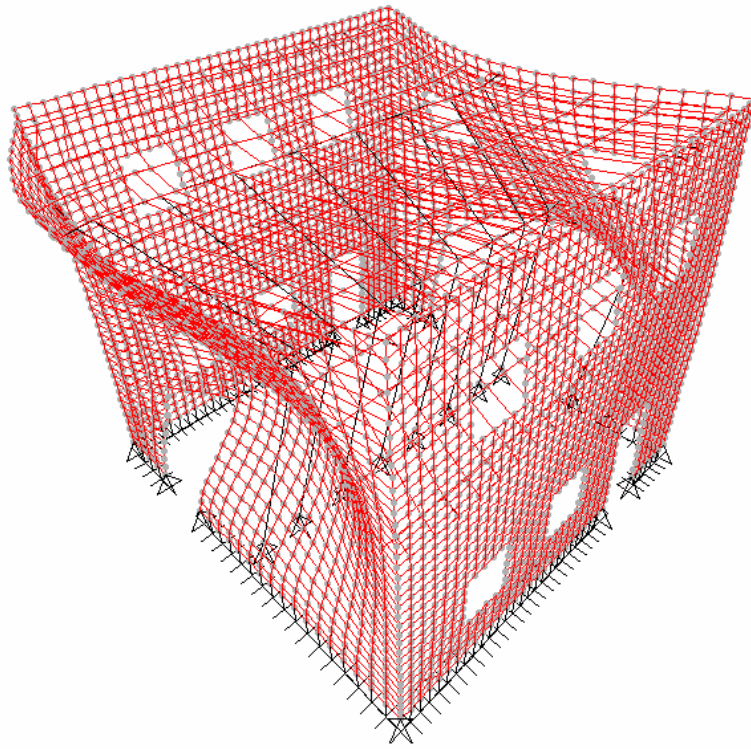


Figure 4–15. Third-mode shape of test structure, period of 0.063 sec.

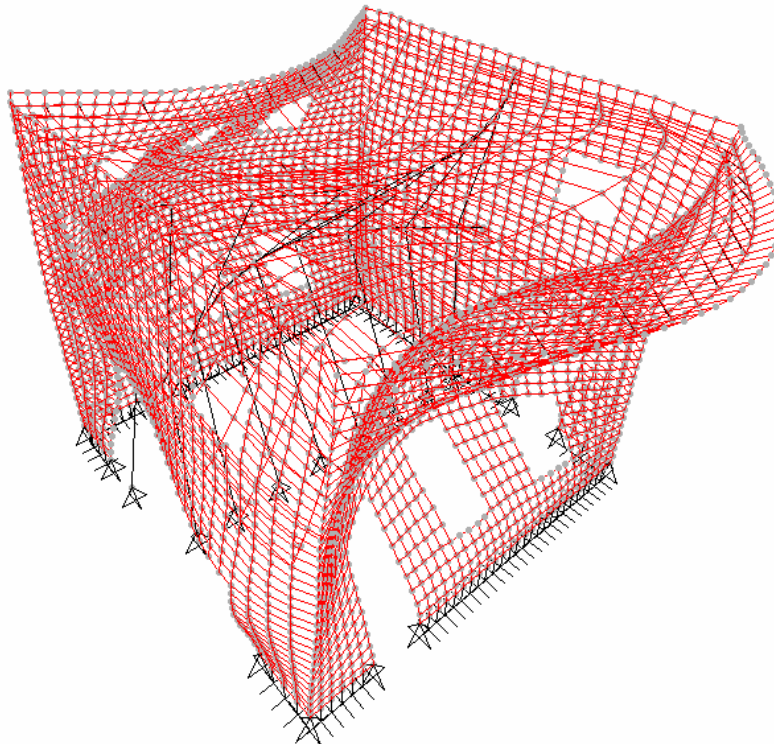


Figure 4–16. Fourth-mode shape of test structure, period of 0.053 sec.

## Predicted Dynamic Response

The response of a building to any load case is best understood through an evaluation of the load path from the point of application to the foundation. In the case of an earthquake, accelerations that occur at the foundation/ground interface propagate through the height of the structure and generate inertial forces by accelerating the structure's mass. At the floor levels, the diaphragms distribute inertial forces to the lateral load resisting system, which then transfers the forces back to the foundation. For most buildings, the lateral load resisting systems are independent, but because of the continuity of masonry walls, this is not the case for URM structures. Consequently, the lateral motions caused by one direction of motion have a significant effect on the lateral load resisting system in the orthogonal direction.

Sweeney et al. (2004) documented the preliminary analysis of the test model for the considered earthquakes listed in the previous chapter. As previously stated, the Nahanni earthquake produced large responses for multidirectional excitation because the peak responses of the building in the horizontal plan directions for unidirectional excitation occurred at the same time. This section discusses in detail the combinations predicted for the Nahanni earthquake and the effect that the lateral load resisting systems have on each other. In particular, the distribution of base shears, vertical forces, and their combined effect will be presented. Because the results of this section are based upon a 3D linear time-history analysis, this discussion is valid only until first cracking. The loads at which cracking is expected to occur are presented at the end of this section.

### **Base Shears**

The distribution of base shears in a building depends upon the distribution of mass, the acceleration of the mass during a seismic event, and the stiffness of the building's diaphragms. The base shear that an in-plane wall resists includes the inertial forces resulting from its own mass and a portion of the inertial forces generated by the mass of the diaphragms and the mass of the out-of-plane walls. In other words, the forces that result from the acceleration of an in-plane wall's mass are resisted entirely by that wall, but the forces that result from the acceleration of the diaphragms' mass and the out-of-plane walls' mass are distributed to the in-plane walls based upon the stiffness of the diaphragm. For a flexible diaphragm, like those in the test model, inertial loads are transferred according to amount of force located in the tributary area of the diaphragm to each in-plane wall. Because the distribution of mass at the diaphragm levels is fairly

symmetric in both plan directions, SAP predicts that the force resisted by the in-plane walls is approximately equal for excitation in either direction.

The predicted distribution of base shears in the test model is most easily understood for the case when ground motion is applied only in the x-direction. Figure 4–17 presents the direction of the shear forces applied to the test model's first-floor piers for this case. Due to symmetry of mass, noted above, the total predicted base shear in walls A and B are approximately equal. Figure 4–17 also demonstrates that the shear forces in the in-plane walls are transferred to the out-of-plane walls due to the connection of the lateral load resisting systems. This behavior is consistent with the direction of shear flow in a box beam section.

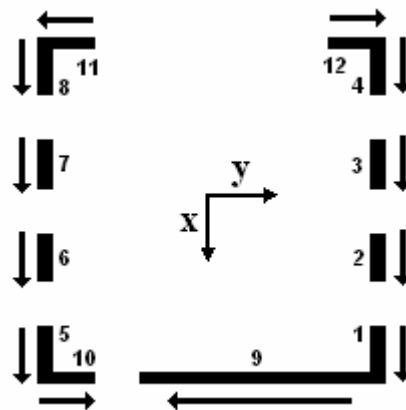


Figure 4–17. Distribution of shear forces for earthquake only in the x-direction.

In terms of magnitude, SAP predicts that the shear forces in the piers of wall A shown in Figure 4–17 are nearly equal (Figure 4–18). This result indicates the possibility that the pier stiffness values calculated from FEMA 356, which are presented in Table 4-1, are somewhat inaccurate. The distribution of shear force between the piers of wall B is essentially identical to what is shown in Figure 4–18. The piers of the out-of-plane walls (walls 1 and 2) develop shear forces that are equal in magnitude and opposite in direction, resulting in a total wall shear approximately equal to zero. Figure 4–19 presents the shear applied to the piers of wall 1 for ground motion only in the x-direction.

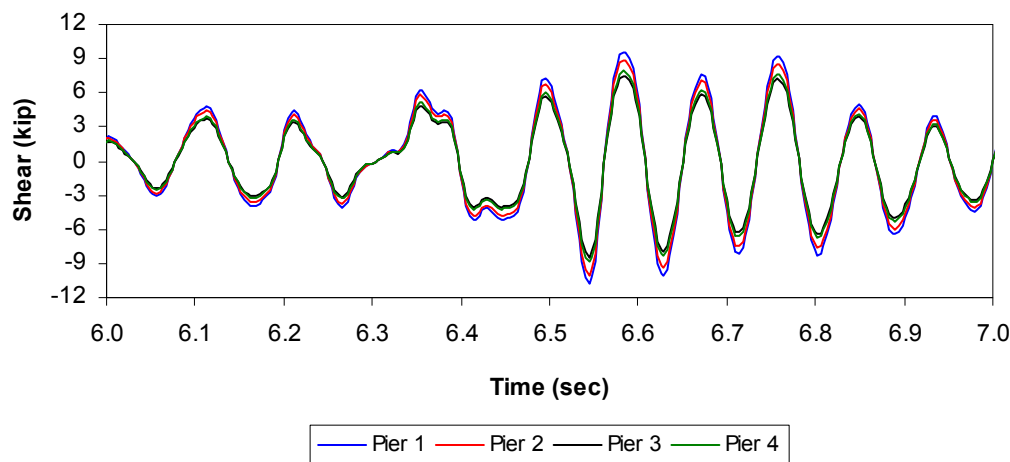


Figure 4-18. Shear in piers of wall A for earthquake only in the x-direction.

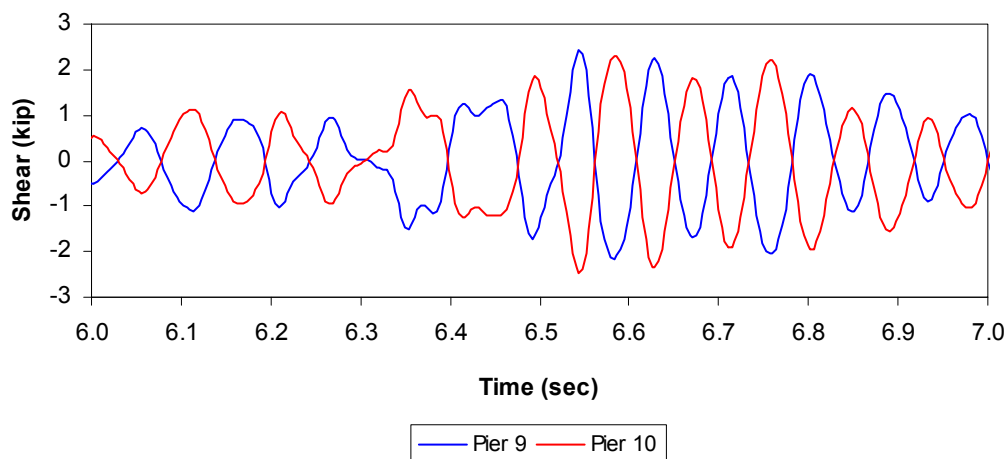


Figure 4-19. Shear in piers of wall 1 for earthquake only in the x-direction.

In the perpendicular direction, the base shear distribution is somewhat more complicated. This is due to the fact that the locations of the center of mass and the center of stiffness do not coincide in the 1-2 plane direction, as they do in the A-B plane direction (wall 1 is considerably stiffer than wall 2). The resulting applied base shear (inertial loads) is located at the center of mass, and consequently, the translation of the base shear to the center of stiffness results in a torsional moment. In the case of a rigid diaphragm, the full torsional moment is transferred to the walls in proportion to each wall's stiffness and its distance away from the center of stiffness. However, due to the deformation of a flexible diaphragm, only a portion of the torsional moment can be transmitted. For the test model, the stiffnesses of walls A and B are so much greater than the stiffnesses of walls 1 and 2 that it can be assumed that they resist the entire moment

transmitted. The shears developed in walls A and B are in opposite directions and form a couple that counteracts the applied torsional moment. Graphically, the distribution of base shears for excitation only in the y-direction can be understood as the sum of the translational and torsional shears (Figure 4–20).

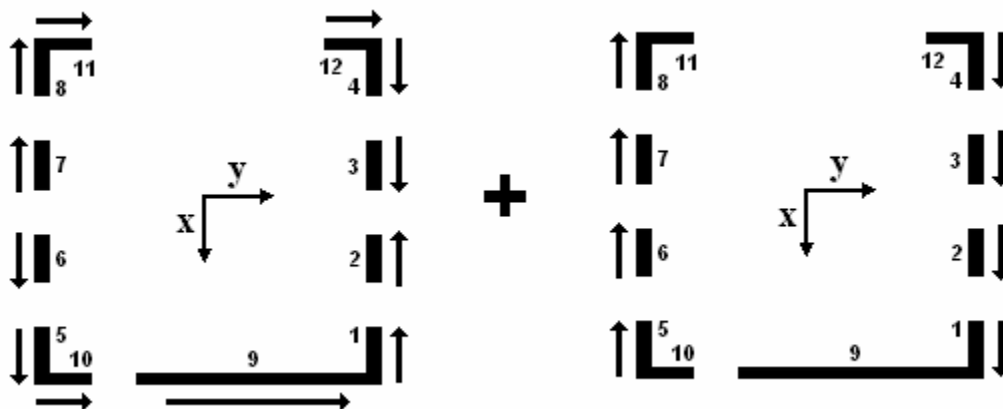


Figure 4–20. Distribution of shear forces for earthquake only in the y-direction.

While the magnitudes of the predicted shear forces in walls 1 and 2 are approximately equal for accelerations in the y-direction, the distribution of shear within these walls is very different. Because piers 11 and 12 are identical (wall 2), they resist the same shear force; however, pier 9, which comprises most of wall 1, resists a much larger shear force than pier 10 (Figure 4–21). The shear forces in the constituent piers of walls A and B are not as easily understood because it is impossible to separate the shears developed through translation from those developed through torsion when examining the results from SAP. However, the results do indicate that piers 4 and 8 (adjacent to wall 2) sustain large shear forces compared to the other piers in walls A and B (Figure 4–22 and Figure 4–23). Furthermore, the shear forces in piers 1 and 5 due to translation are larger than those due to torsion, and consequently, the direction of their shear forces is opposite of the other piers.

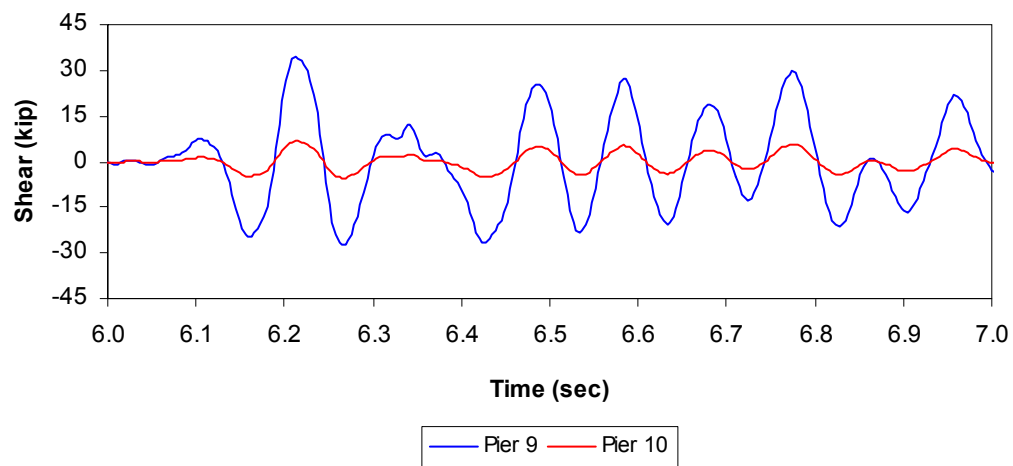


Figure 4-21. Shear in piers of wall 1 for earthquake only in the y-direction.

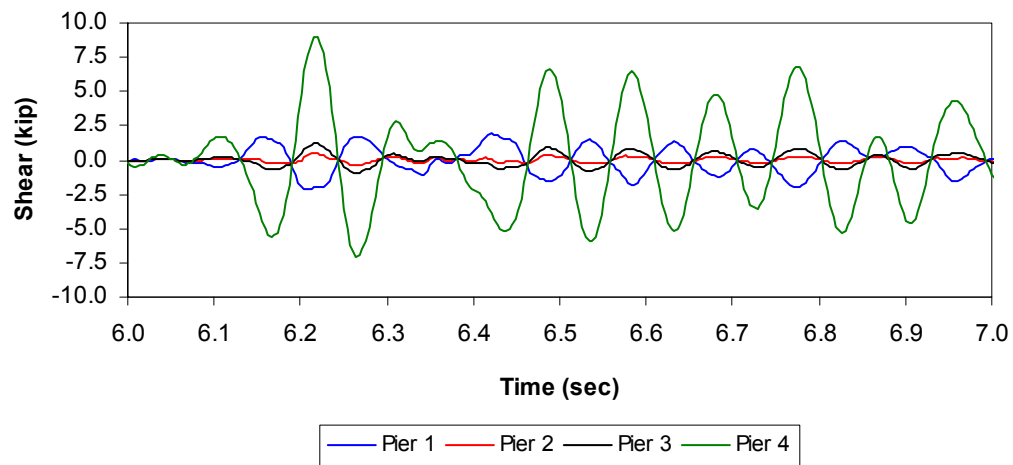
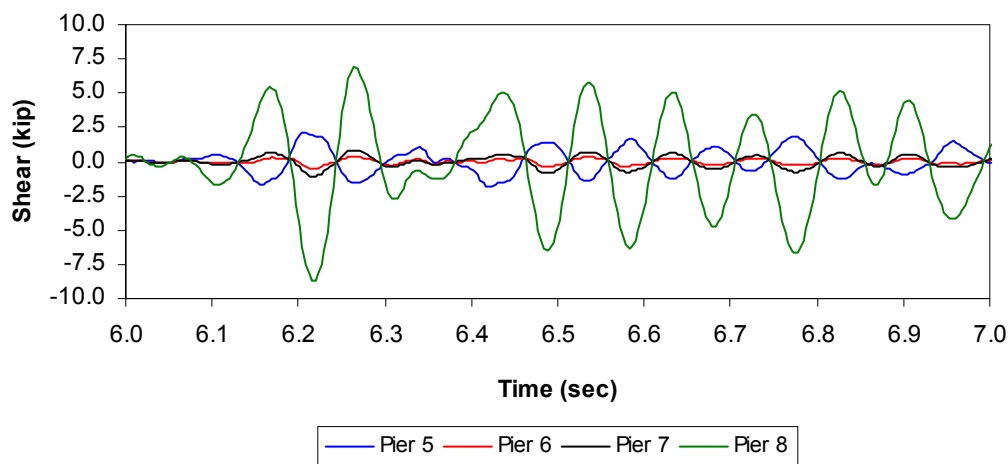


Figure 4-22. Shear in piers of wall A for earthquake only in the y-direction.



**Figure 4-23. Shear in piers of wall B for earthquake only in the y-direction.**

In the case of a linear analysis, the response of a building to a multidirectional earthquake can be determined by summing the time-history responses from individual earthquake components. For design, a combination rule is normally used, such as the FEMA 368 100%-30% combination of peak response quantities. This method is based on the principle that maximum responses from orthogonal ground motion components usually do not occur at the same time. However, previous analytical work performed by Sweeney et al. (2004) indicated that large horizontal responses occurred concurrently for the Nahanni earthquake, which generated wall forces up to 7.5% greater than those predicted by FEMA 368. The nature of the combination is positive in the x-direction and positive in the y-direction (or a negative combination when the force direction reverses). Therefore, Figure 4-17 and Figure 4-20 can be used to gain perspective on the summation of pier shear forces.

There are several piers in the test model that will experience additive shear from the two horizontal ground motion components. In particular, piers 12, 10, 4, and 3 demonstrate this behavior. The most severe case of shear combination occurs in pier 4, where the shear force resulting from the x and y components of ground motion are of comparable value. In instances where one component dominates the response, the combinational effect is considerably less significant. To demonstrate this principle and the nature of the building response to the bidirectional Nahanni earthquake, Figure 4-24 and Figure 4-25 plot the shear force in piers 4 and 12, respectively, for both the independent x and y direction earthquakes and also the simultaneous xy earthquake.

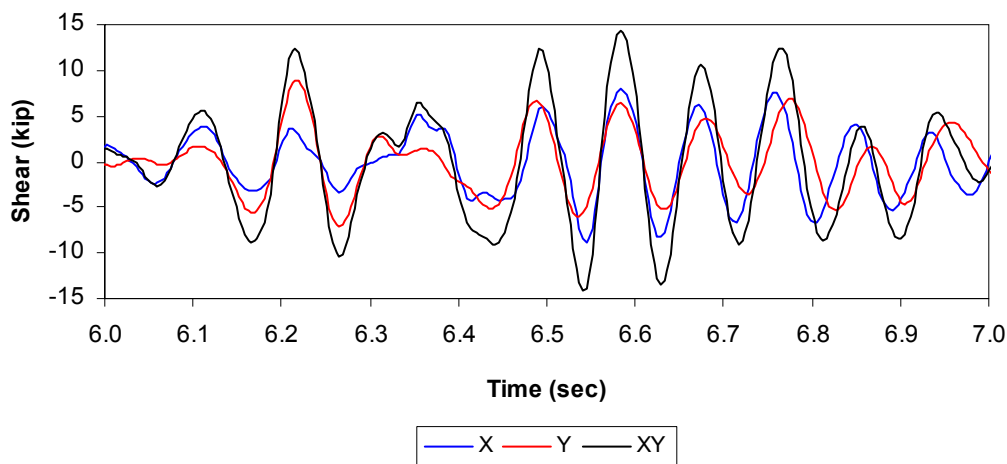


Figure 4-24. Shear in pier 4 for unidirectional and bidirectional Nahanni earthquake.

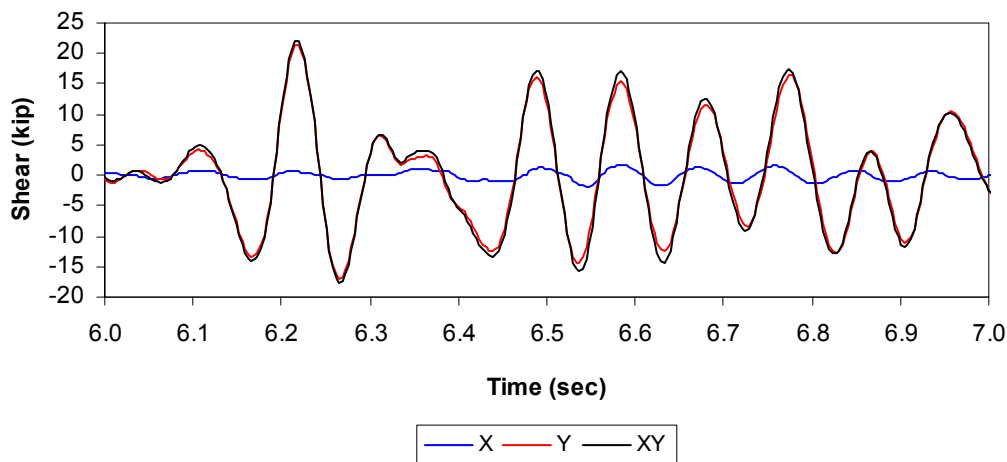


Figure 4-25. Shear in pier 12 for unidirectional and bidirectional Nahanni earthquake.

The behavior of each pier in the test structure shown in the above figures demonstrates the similarity of the horizontal building responses. However, as Figure 4-17 and Figure 4-20 indicate, some of the piers are subjected to shear forces from the two ground motion components acting in opposite directions, thereby reducing the bidirectional response. Table 4-4 presents the peak shear forces in all of the piers for unidirectional excitation and compares them with the peak shear force resulting from bidirectional excitation and the shear force predicted by the 100%-30% combination rule prescribed in FEMA 368. The table also indicates which piers violate the FEMA 368 method and by what percentage.

**Table 4-4. Comparison of peak shear forces due to bidirectional excitation with those predicted by the FEMA 368 combination rule.**

Pier (wall)	V <sub>x</sub> (kip)	V <sub>y</sub> (kip)	V <sub>100%-30%</sub> (kip)	V <sub>xy</sub> (kip)	Violates?	% Underestimated
1 (A)	-10.79	-2.17	11.44	9.72	NO	0.00%
2 (A)	-9.99	0.55	10.16	10.25	YES	0.93%
3 (A)	-8.41	1.24	8.78	9.06	YES	3.07%
4 (A)	-8.87	8.95	11.61	14.35	YES	19.09%
5 (B)	-10.35	2.07	10.97	11.32	YES	3.08%
6 (B)	-9.65	-0.56	9.82	9.36	NO	0.00%
7 (B)	-8.13	-1.11	8.46	7.53	NO	0.00%
8 (B)	-8.59	-8.71	11.29	8.86	NO	0.00%
9 (1)	2.43	34.24	34.97	33.24	NO	0.00%
10 (1)	-2.48	6.64	7.38	7.71	YES	4.23%
11 (2)	1.74	20.85	21.37	20.19	NO	0.00%
12 (2)	-1.85	21.29	21.85	21.95	YES	0.48%

### **Vertical Forces**

The decision was made to perform shake table tests only in the horizontal directions because most changes in vertical stress do not come from the vertical ground motions themselves, but rather from the lateral motions on the building. Masonry buildings constitute a box system, and that system is necessary to resist horizontal actions (Beskos 1997). Therefore, when the building experiences force in one direction, the in-plane walls resist the force by shear, and the connecting flanges of the out-of-plane walls resist the force by compression and tension. In this way, the out-of-plane walls help prevent the global overturning of the structure. This behavior is especially evident in a building like the test model, which has a small plan aspect ratio. The tensile and compressive forces that result from lateral motions in the positive x and positive y directions are represented graphically in Figure 4-26 and Figure 4-27, respectively. The two drawings of the building in Figure 4-27 correspond to the translational component (left) and the torsional component (right), as was the case for Figure 4-20. In both Figure 4-26 and Figure 4-27, only the total effect of the lateral load on adjacent piers at a building corner is given because of the complex interaction of the two piers.

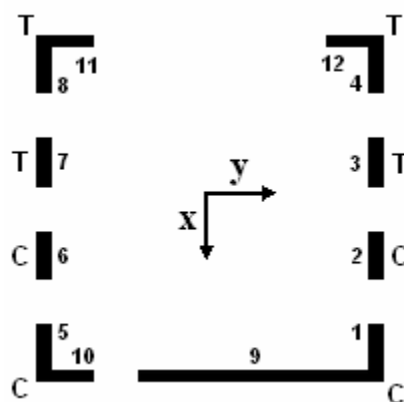


Figure 4-26. Direction of vertical forces for positive x-direction earthquake.

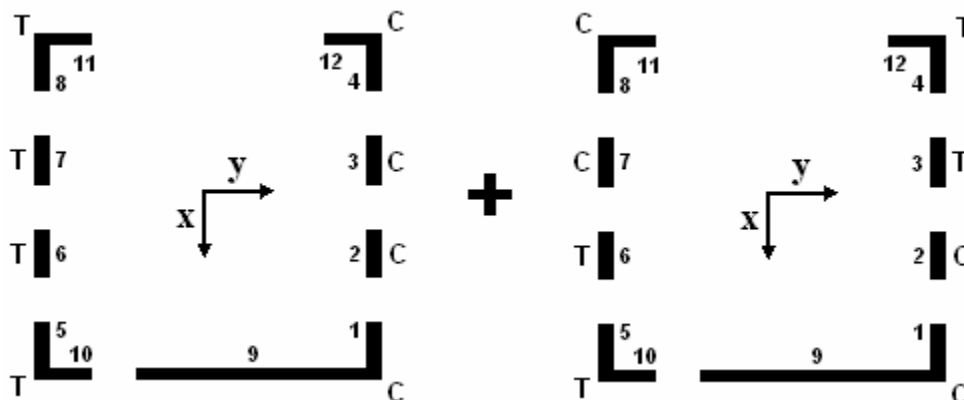


Figure 4-27. Direction of vertical forces for positive y-direction earthquake.

The vertical stresses imparted to an interior in-plane pier (piers 2, 3, 6, and 7) for unidirectional loading include those resulting from shear, global overturning moment, and dead load. The stresses caused by these components are shown acting on a pier in Figure 4-28. The dead load, displayed at the top of the figure, is constant over the length of the pier. The global overturning moment imparts a linear stress distribution along the length of an in-plane wall, ranging from maximum compression at one end of the wall to maximum tension at the other end. Therefore, the stresses in a pier due to this component will be linear and compressive or tensile in nature, in accordance with Figure 4-26 and Figure 4-27. The vertical stresses due to shear are simply bending stresses caused by the fixity at the top and bottom of the pier and are oriented such that they counter-act local overturning.

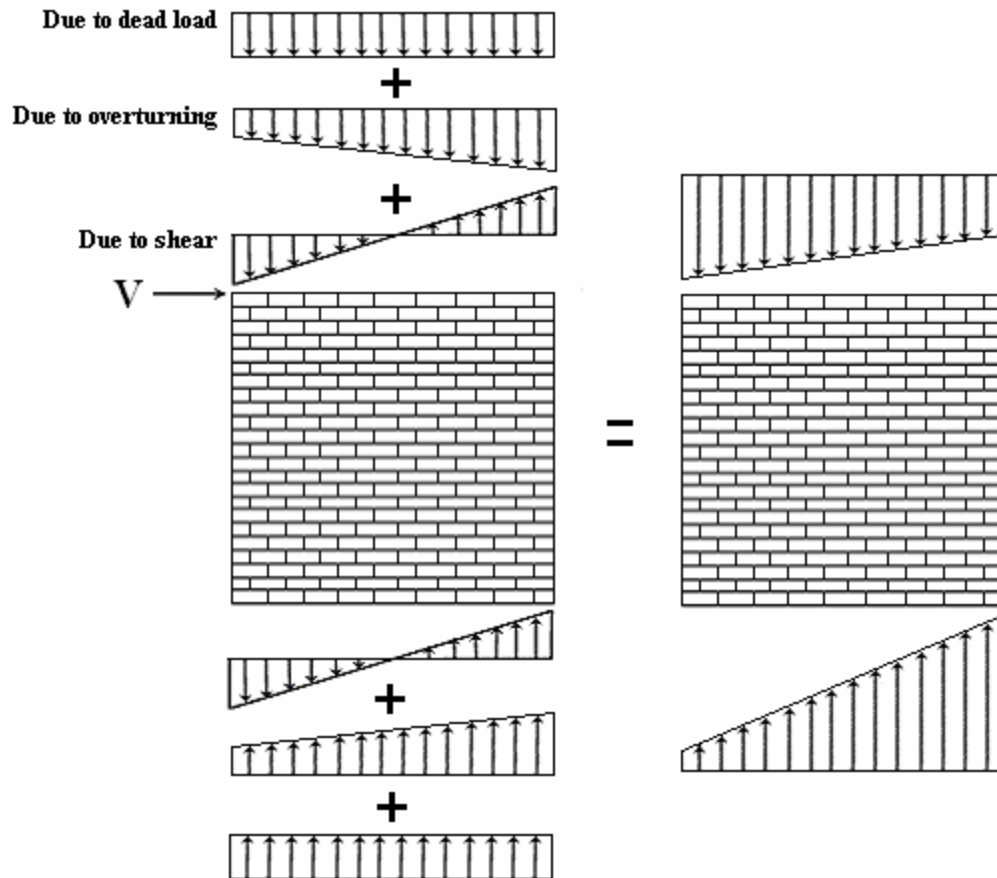
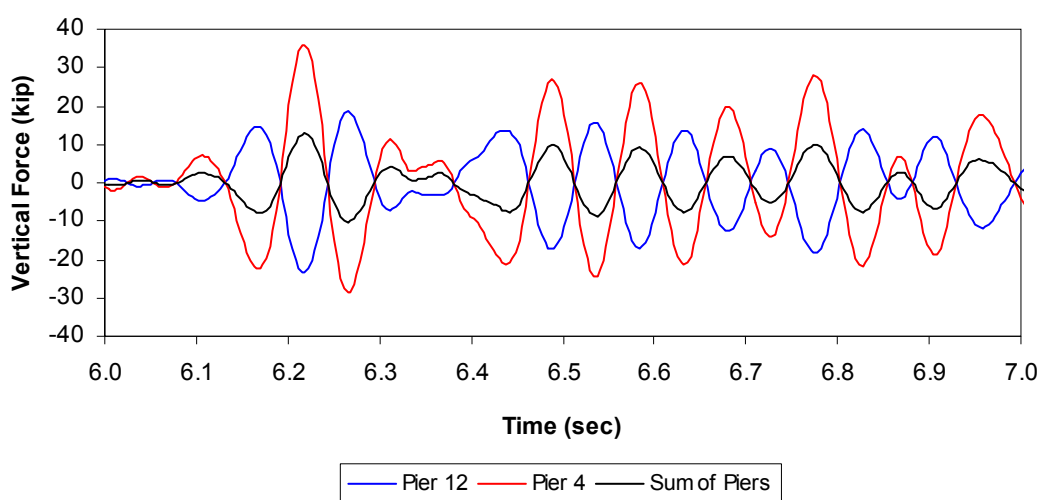


Figure 4-28. Combination of vertical stresses on an in-plane pier for unidirectional loads only.

At the corners of the structure, the distribution of stresses is more complicated than that shown in Figure 4-28 because the in-plane pier and the adjacent out-of-plane pier act together in bending like the web and flange of a beam. Therefore, the neutral axis for bending of the section shifts from mid-depth for a rectangular section, to a location closer to the flange. To illustrate the consequence of the interaction of corner piers, the behavior of piers 12 and 4 for positive y-direction loading will be considered. In this case, pier 12 acts as the web and pier 4 acts as the flange. The cross-section has a total depth of 24 in., a flange width of 24 in., a flange depth of 5.9 in., and a web width of 3.9 in. The elastic neutral axis for this section is only 1 in. below the bottom of the flange. Thus, over 70% of the base of pier 12 is in tension when considering the stresses resulting only from shear. The compressive stresses due to the overturning moment and the dead load of the structure lower the neutral axis some, but not enough to change the resultant force at the base of pier 12 from tensile to compressive because of the large magnitude of the stresses caused by the applied shear force.

The behavior of piers 12 and 4 in this example is contrary to the expectation that pier 12 will have a net compressive force for positive y-direction loading because of the effect of the overturning moment. Note, however, that the overall effect on the combined piers is compressive for a positive y-direction load, as Figure 4–29 demonstrates. This fact is considered in Figure 4–26 and Figure 4–27 by demonstrating that the total vertical effect for two corner piers is consistent with the nature of the global overturning moment. In Figure 4–29, vertical force does not include dead load and tensile forces are negative. Therefore, a positive y-direction load is being applied when the vertical force in pier 4 is positive.



**Figure 4–29. Vertical forces in piers 12 and pier 4, along with their sum, for y-direction earthquake.**

The composite behavior of piers 12 and 4 is consistent with the response of the other corners in the building. However, in not every case is the resultant force on the web of the cross-section tensile when the flange is in compression. There are two reasons for this fact. First, if the orientation of the cross-section is such that the pier of smaller width acts as the flange (pier 12 in our example), the neutral axis will be closer to mid-depth than in the case where the pier of greater width acts as the flange. As a result, more of the web will be in compression and the resultant tensile force will decrease. The second reason is that the vertical forces caused by shear may be small enough that the vertical forces due to global overturning and dead load mask them. This is the case for piers 10 and 5 when pier 10 acts as the web of the combined cross-section. The shear force sustained by pier 10 is less than one-third of the force that pier 12 sustains for ground motion only in the y-direction. Consequently, the total effect of the global overturning moment and dead load is just enough to convert the resultant force on pier 10 from tension to compression Figure 4–30.

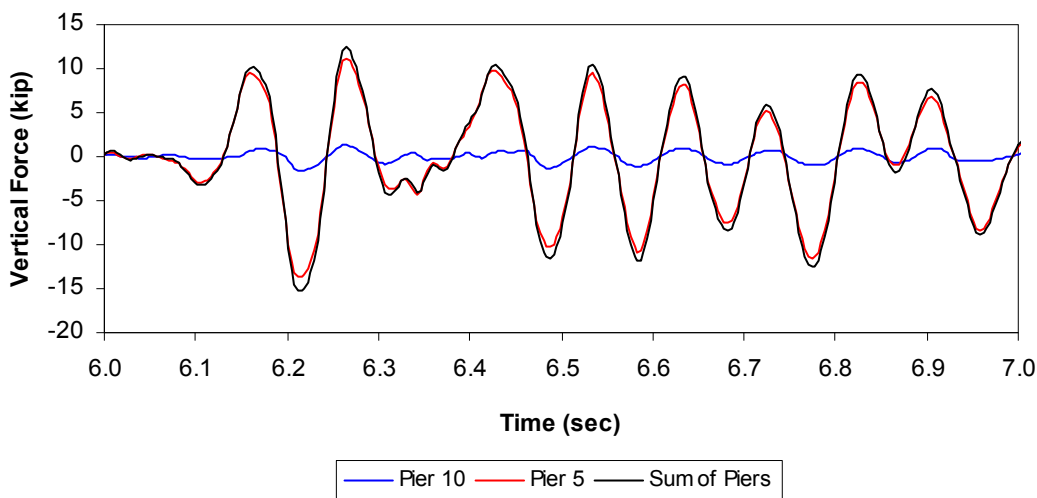


**Figure 4-30. Vertical forces in pier 10 and pier 5, along with their sum, for y-direction earthquake.**

The majority of the vertical forces resulting from ground motion perpendicular to a wall's length are located near the wall edges where the corner piers act as flanges for the corner piers of the in-plane walls. The interior piers of an out-of-plane wall also sustain vertical forces due to cross-motion, but those forces are considerably smaller than the forces at the ends of the wall. Figure 4-31 plots the vertical forces in wall B for ground motion only in the y-direction. As expected, the forces at the ends of wall B are larger than those acting on the interior piers because of flange effects. Pier 8 sustains larger vertical forces than pier 5 because the shear force in pier 12 is more than three times larger than the shear in pier 10. Consequently, the vertical force component due to shear is much greater in pier 8 than in pier 5. The behavior of wall A as an out-of-plane wall is identical to that shown in Figure 4-31. For the case where wall 2 acts as an out-of-plane wall during unidirectional ground motion in the x-direction, piers 12 and 11 receive the same vertical force. However, for wall 1, pier 9 resists vertical forces that are considerably larger than those resisted by pier 10 due to the size of pier 9.

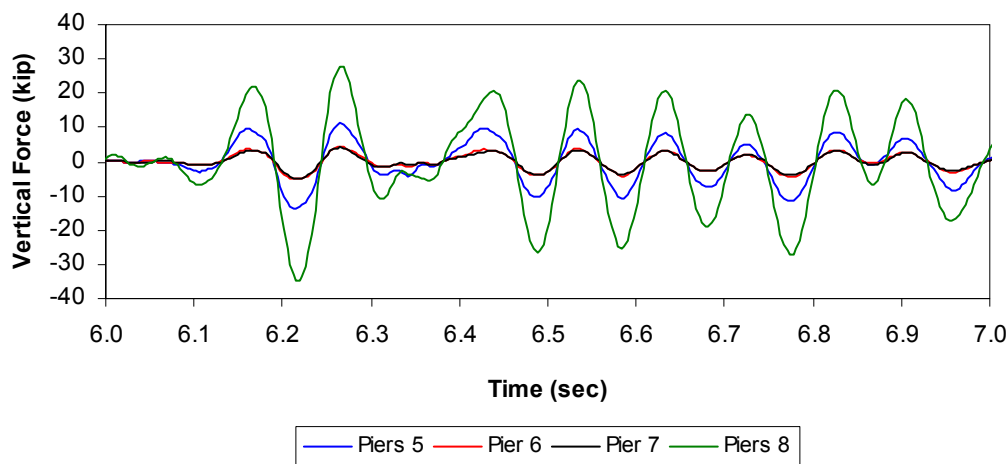


**Figure 4-31. Vertical forces in wall A for y-direction earthquake only.**

The discussion of vertical forces has thus far been limited to unidirectional ground motion. For bidirectional ground motion, Figure 4-26 and Figure 4-27 can be examined together to determine the distribution of vertical forces. These figures indicate that only piers 9 and 2 could possibly experience vertical forces that combine additively for all components. Figure 4-32 illustrates the combination of vertical forces on pier 2 for the both horizontal ground motion components and also demonstrates that for pier 2, the dominant component is due to cross-motion (y-direction).

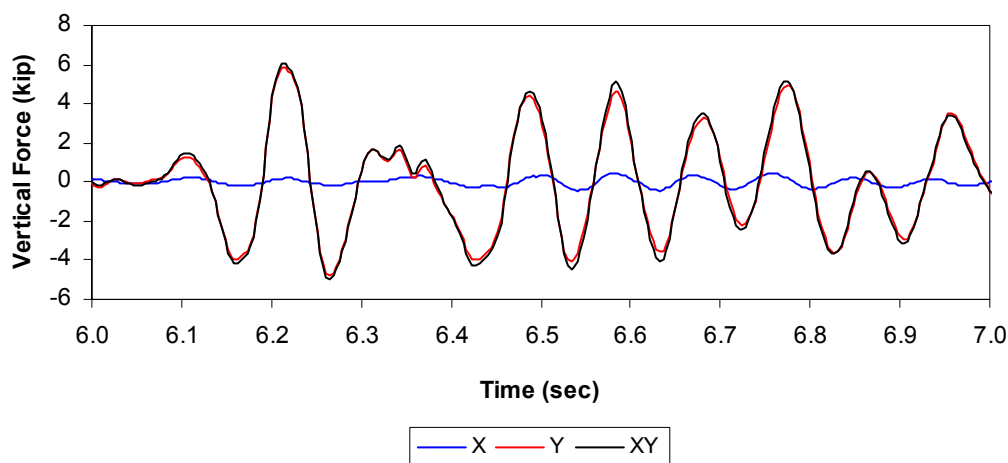


**Figure 4-32. Vertical forces in pier 2 for unidirectional and bidirectional ground motions.**

In general, due to the complexity of the combination of vertical stresses arising from shear, in-plane overturning moment, out-of-plane overturning moment, and dead load, the behavior of each pier should be examined individually. To gain perspective on the magnitude of vertical forces resulting from lateral load, Table

4-5 presents the maximum and minimum vertical forces on each pier resulting from the unidirectional and bidirectional earthquakes. Table 4-5 also includes the dead load in the piers, which can be added to the forces resulting from the ground motions to determine the total maximum and minimum vertical forces. The results indicate that for all piers except piers 11 and 12, the dominant vertical force is due to the ground motion component perpendicular to the length of the pier. Piers 11 and 12 do not conform to this trend because of the very large vertical forces generated by shear during in-plane excitation.

**Table 4-5. Maximum and minimum vertical forces due to unidirectional and bidirectional earthquakes.**

Pier (wall)	$P_{x, \max}$	$P_{x, \min}$	$P_{y, \max}$	$P_{y, \min}$	$P_{xy, \max}$	$P_{xy, \min}$	$P_{\text{dead}}$
1 (A)	4.18	-4.68	15.70	-12.71	17.59	-14.44	3.40
2 (A)	0.48	-0.43	5.86	-4.81	6.04	-4.96	3.81
3 (A)	0.97	-0.77	5.49	-4.49	5.19	-4.19	3.80
4 (A)	3.85	-3.11	36.08	-28.74	34.82	-27.55	4.45
5 (B)	5.11	-5.59	11.12	-13.72	10.17	-11.44	3.66
6 (B)	0.68	-0.66	4.30	-5.23	4.08	-4.95	3.94
7 (B)	1.13	-0.94	4.15	-5.07	4.53	-5.51	3.95
8 (B)	4.45	-3.57	27.86	-35.00	29.36	-36.55	4.75
9 (1)	19.93	-22.98	1.20	-1.07	19.71	-23.10	9.58
10 (1)	12.48	-13.59	1.33	-1.67	11.60	-12.66	2.44
11 (2)	14.56	-13.15	23.72	-18.95	18.91	-19.98	3.16
12 (2)	14.23	-12.31	18.60	-23.32	28.21	-29.34	2.79

### ***Combined Shear and Vertical Force***

The previous sections discussed only the distribution of base shears and vertical forces individually. However, based on the FEMA 356 equations, it is clear that the lateral strength of a pier is greatly dependent upon compressive stress. Therefore, the interaction of shear and vertical force could have a large effect on the behavior of a URM structure. This is particularly true for the test model because large horizontal responses occur concurrently for the bidirectional Nahanni earthquake. Since vertical forces are due primarily to lateral motions on the building, all piers of the test model will experience large shear forces and large vertical forces at the same time (Figure 4-33).

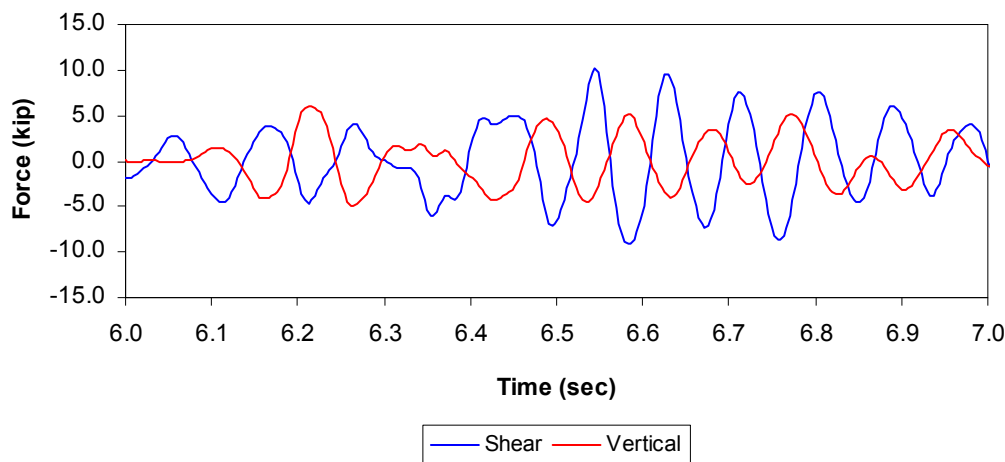


**Figure 4-33. Interaction of base shear and vertical forces for pier 2 under simultaneous xy ground motion.**

Using the FEMA 356 equations, graphs can be constructed for each pier plotting the variation in lateral strength for the four different pier failure modes as a function of vertical load. Figure 4-34 is an example of this type of graph for piers, with  $L/h_{eff}$  equal to 0.81 (piers 2, 3, 6, and 7). The strength of a pier for any vertical load is controlled by its strength in each failure mode. Therefore, for piers 2, 3, 6, and 7, the strength is controlled by rocking until the vertical load reaches 5600 lbs, at which point the failure mode switches to bed-joint sliding.

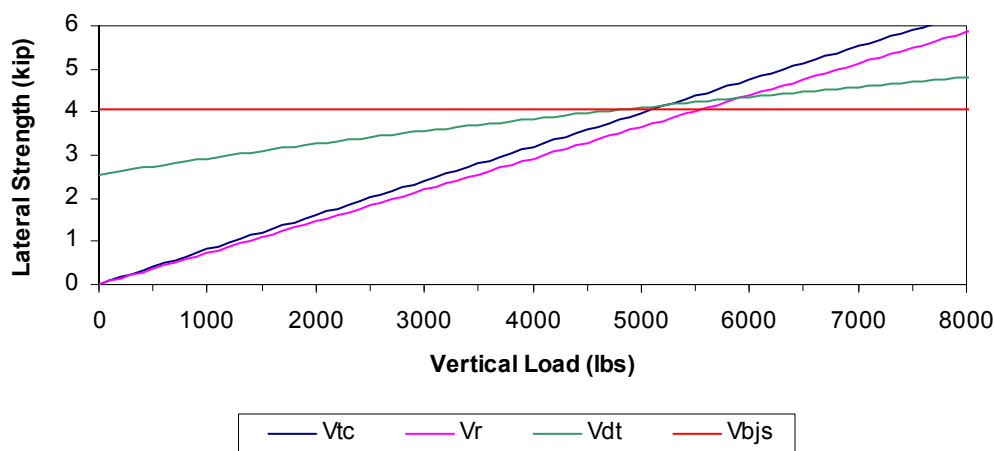


**Figure 4-34. Variation of lateral strength based on vertical load of a 20" x 24.6" pier based on FEMA 356.**

Examination of Figure 4-33 and Figure 4-34 together leads to an important conclusion: large tensile forces resulting from overturning may decrease the strength of a pier to such a degree that the concurrent peak lateral forces far exceed its strength, resulting in severe damage. However, the degree to which this

behavior will affect the test structure is uncertain because of the complex behavior of the corner piers, which comprise eight of the test model's twelve piers. While the vertical loads may decrease the lateral strength of the corner piers, the flange portion of the combined section may offset this reduction by a strength contribution that is not taken into account by the FEMA 356 equations. (FEMA 356 assumes that only the web of the corner cross-section resists shear.) Only seismic testing of the structure will reveal the true effect of shear force and vertical force interaction.

### ***Approximate Cracking Loads***

Based on the results of the SAP 2000NL linear time-history analysis, the percentage of the Nahanni earthquake that is required to cause cracking in each pier was determined. This percentage was found by dividing the capacity of each pier (cracking shear force in Table 4-1) by the demand on the pier for both unidirectional earthquakes (x and y) and the bidirectional earthquake (xy). The results are presented in Table 4-6, Table 4-7, and Table 4-8. Since the peak accelerations for the x-direction and y-direction Nahanni time histories are approximately  $\pm 1$  g, the percentages listed in the tables can also be thought of as the accelerations (in g) required to cause cracking multiplied by 100. Note that these cracking loads do not consider the interaction of shear and vertical forces (for reasons just discussed) and that they assume the entire structure is linear elastic. In other words, this analysis cannot take into account the structure's behavioral shift from a completely linear-elastic state to one that is partially nonlinear.

**Table 4-6. Cracking loads predicted by SAP 2000NL for Nahanni x-direction earthquake.**

Pier (wall)	V <sub>crack</sub> (kip)	V (kip)	% of EQ to Crack
1 (A)	3.417	-10.79	31.67%
2 (A)	2.373	-9.99	23.76%
3 (A)	2.373	-8.41	28.22%
4 (A)	1.981	-8.87	22.34%
5 (B)	3.417	-10.35	33.02%
6 (B)	2.373	-9.65	24.59%
7 (B)	2.373	-8.13	29.19%
8 (B)	1.981	-8.59	23.06%
9 (1)	3.513	2.43	144.59%
10 (1)	1.163	-2.48	46.91%
11 (2)	1.370	1.74	78.73%
12 (2)	1.370	-1.85	74.05%

**Table 4-7. Cracking loads predicted by SAP 2000NL for Nahanni y-direction earthquake.**

<b>Pier (wall)</b>	<b>V<sub>crack</sub> (kip)</b>	<b>V (kip)</b>	<b>% of EQ to Crack</b>
1 (A)	3.417	-2.17	157.48%
2 (A)	2.373	0.55	431.48%
3 (A)	2.373	1.24	191.38%
4 (A)	1.981	8.95	22.14%
5 (B)	3.417	2.07	165.09%
6 (B)	2.373	-0.56	423.78%
7 (B)	2.373	-1.11	213.80%
8 (B)	1.981	-8.71	22.75%
9 (1)	3.513	34.24	10.26%
10 (1)	1.163	6.64	17.52%
11 (2)	1.370	20.85	6.57%
12 (2)	1.370	21.29	6.43%

**Table 4-8. Cracking loads predicted by SAP 2000NL for combined Nahanni x-direction and y-direction earthquake.**

<b>Pier (wall)</b>	<b>V<sub>crack</sub> (kip)</b>	<b>V (kip)</b>	<b>% of EQ to Crack</b>
1 (A)	3.417	-9.72	35.16%
2 (A)	2.373	-10.25	23.15%
3 (A)	2.373	-9.06	26.19%
4 (A)	1.981	14.35	13.81%
5 (B)	3.417	-11.32	30.19%
6 (B)	2.373	-9.36	25.35%
7 (B)	2.373	-7.53	31.52%
8 (B)	1.981	8.86	22.36%
9 (1)	3.513	33.24	10.57%
10 (1)	1.163	7.71	15.09%
11 (2)	1.370	20.19	6.79%
12 (2)	1.370	21.95	6.24%

## 5 Testing Program

### Test Structure Instrumentation

#### *Objective*

Instrumentation of the test structure was designed such that the dynamic response of the building could be well described while also gaining insight into the force/deformation properties of the structural components. In particular, the instrumentation included accelerometers, global displacement transducers, and local displacement transducers. The following lists indicate the models used and intended purpose for each type of measurement device.

**Accelerometers:** Endevco Model 7290-10 and Microtron Model 7290-30

- Record the base motion.
- Determine dynamic building properties including fundamental periods and damping.
- Determine diaphragm amplification of wall accelerations and base accelerations.
- Determine wall amplification of base accelerations.

**Global Displacement Transducers:** Celesco Model PT101-20 variable-resistance, precision rotary displacement transducers

- Determine approximate deformed shape of diaphragm and out-of-plane walls.
- Determine displacement of in-plane walls relative to each other to investigate degree of coupling.
- Identify torsional or twisting response.
- Determine story drifts.

**Local Displacement Transducers:** ETI Inc. Model LCP12A-25-10K and ETI Inc. Model LCP12A-50-10K linear potentiometers

- Determine displacement of masonry piers.

### ***Instrumentation Scheme***

The following sections describe the instrumentation scheme designed for the test model and also include diagrams of the measurement locations.

#### **Accelerometers**

Figure 5–1 through Figure 5–3 show the locations of the accelerometers used at the level of the base beam, floor diaphragm, and roof diaphragm, respectively. The base beam accelerometers allowed for a complete description of the ground motion with respect to the translational and rotational components. While seismic testing was only conducted in the horizontal plan directions, rotational components inevitably exist and must be considered when evaluating the response of the structure. The diaphragm accelerometers measured the in-plane and out-of-plane accelerations of the walls, as well as accelerations at the center of the diaphragm.

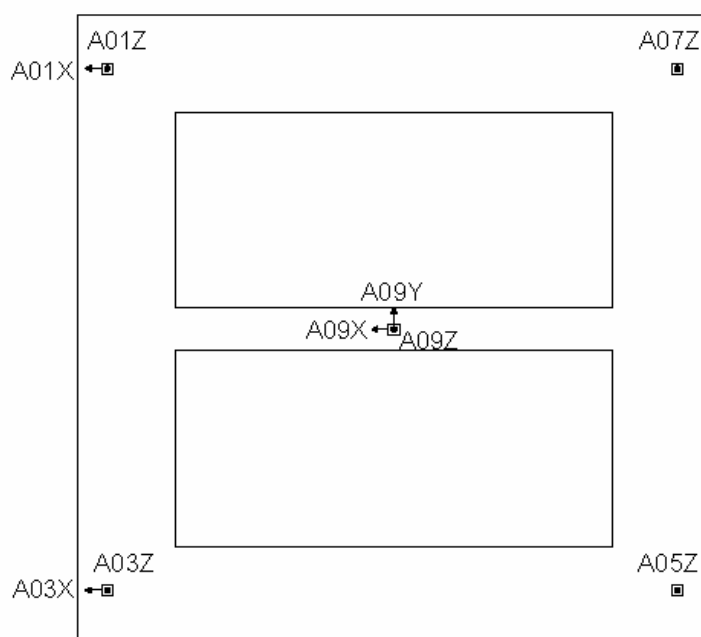


**Figure 5–1. Accelerometers located at base beam level.**

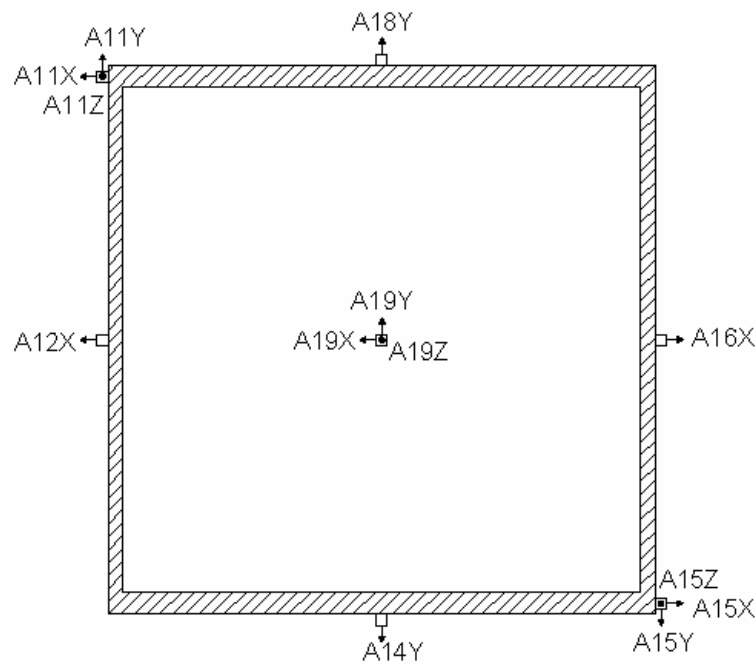


Figure 5-2. Accelerometers located at the floor diaphragm level.

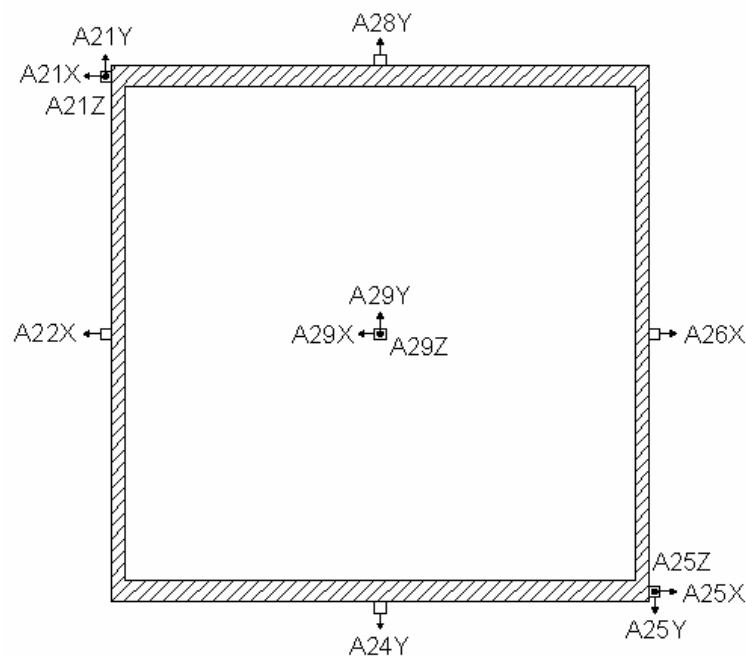
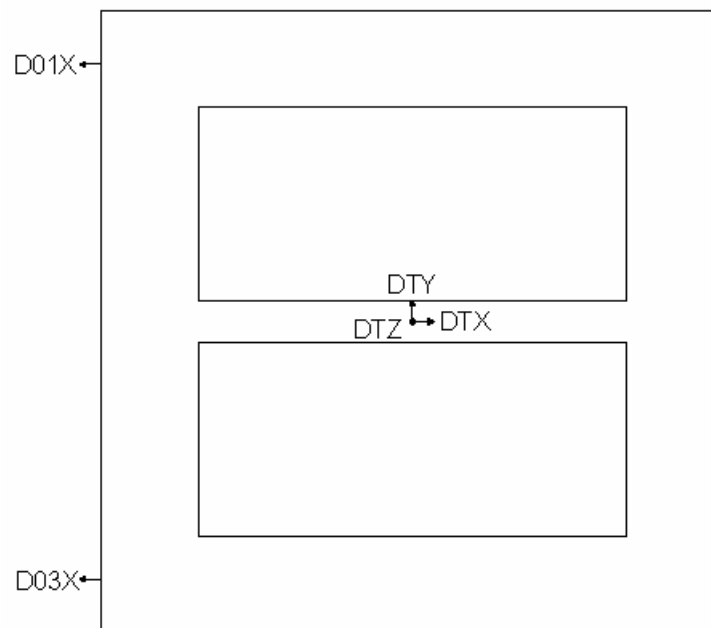


Figure 5-3. Accelerometers located at the roof diaphragm level.

### Global Displacement Transducers

Figure 5-4 through Figure 5-6 show the global displacement transducers located at the level of the base beam, floor diaphragm, and roof diaphragm, respectively.

Similar to the accelerometer scheme, the global displacements measured during testing included the ground motion, in-plane and out-of-plane displacement of the walls, and the displacement of the diaphragm (taken as the out-of-plane displacement of the walls due to connectivity). The global displacement transducers were attached to fixed locations away from the test structure and were connected to the positions shown using steel wire. The only exception to this setup was for the displacements DTX, DTY, and DTZ, which were measured directly by the shake table.



**Figure 5-4. Global displacement transducers located at base beam level.**

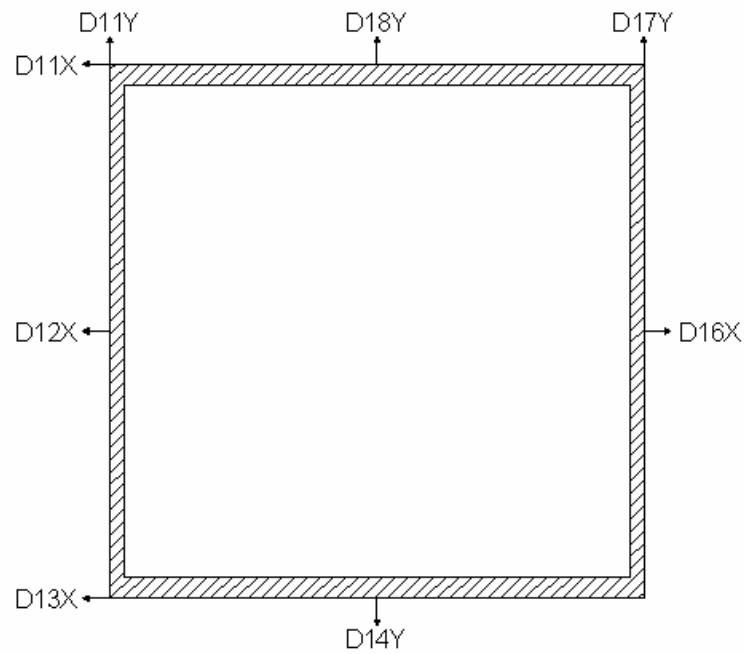


Figure 5–5. Global displacement transducers located at floor diaphragm level.

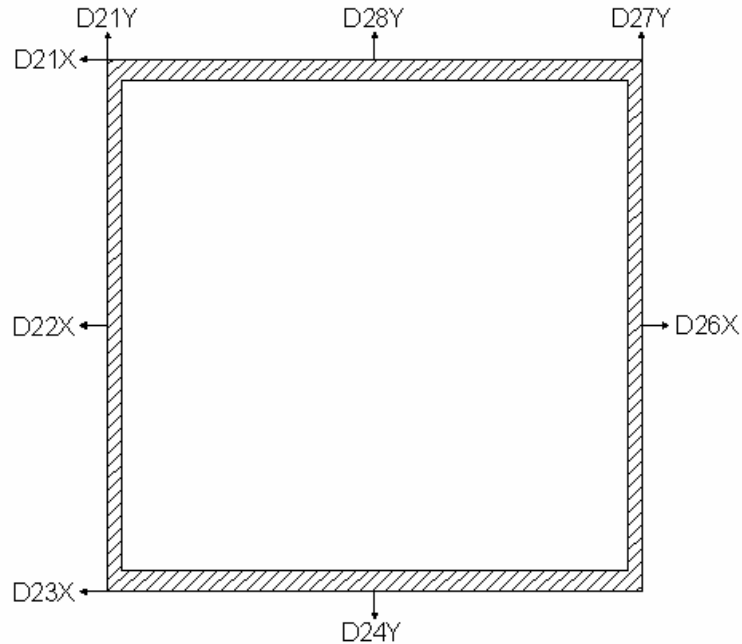


Figure 5–6. Global displacement transducers located at roof diaphragm level.

### Local Displacement Transducers

Figure 5–7 through Figure 5–10 show the local displacement transducers used on the walls of the test structure. In general, the transducers located on the

piers were oriented vertically and diagonally in order to measure rocking and sliding behavior, respectively. Figure 5–11 is a photograph of the instrumentation on pier 1, which is essentially identical to the instrumentation on the other piers of the test structure. The steel wires that span the gage length were visually inconspicuous in the original photo, so they have been accentuated with black lines. Local displacement transducers were also attached between the diaphragm and the walls (LAV9 – LAV11; LBV9 – LBV11) to measure slip in the joist pockets.

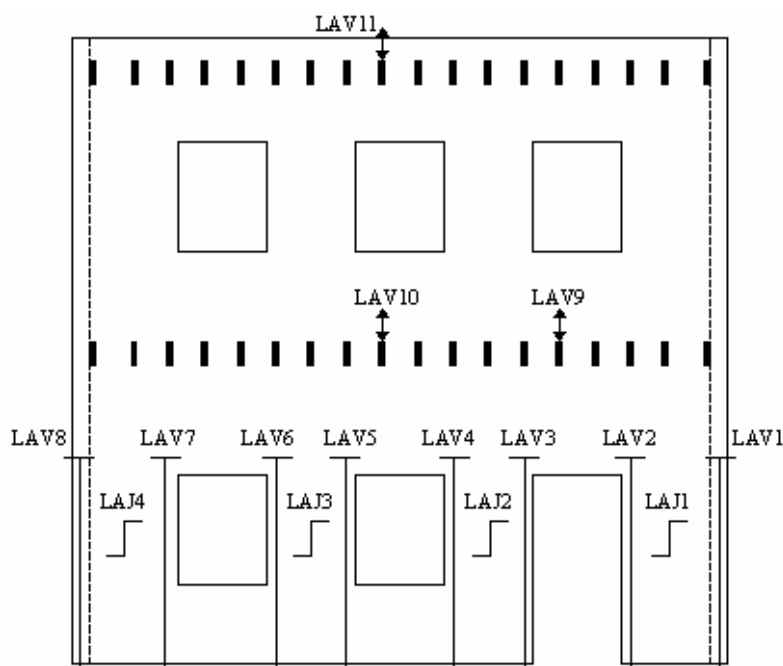


Figure 5–7. Local displacement transducers for wall A.

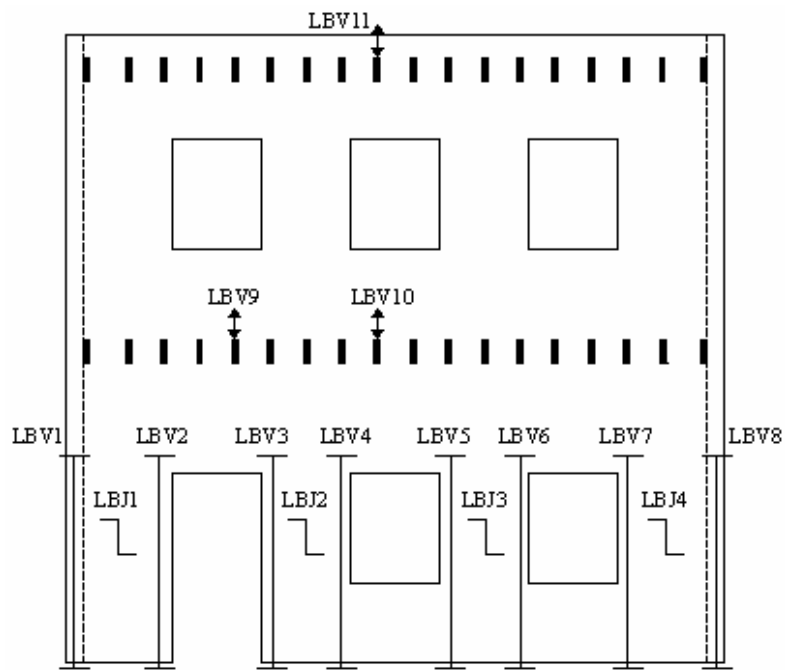


Figure 5–8. Local displacement transducers for wall B.

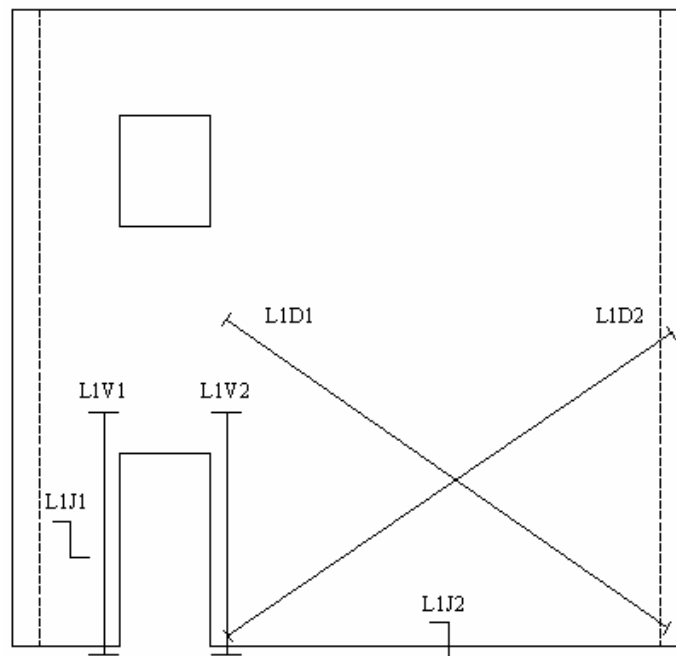


Figure 5–9. Local displacement transducers for wall 1.

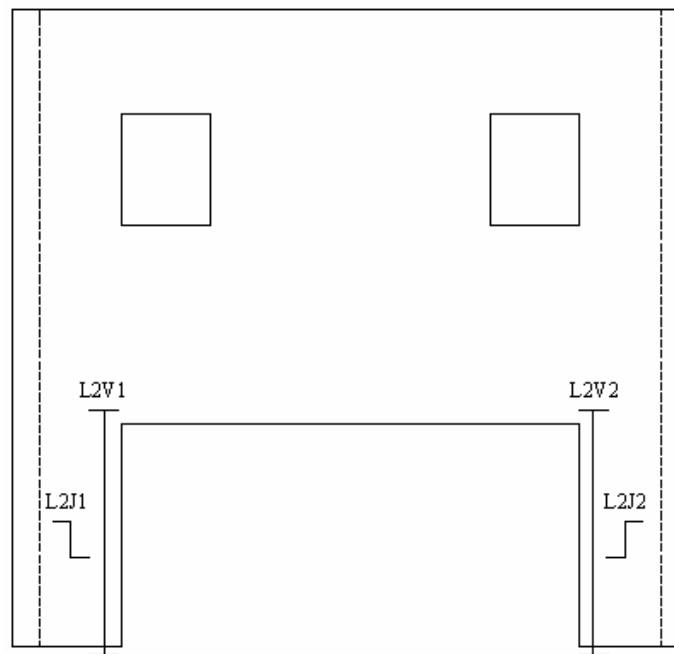


Figure 5-10. Local displacement transducers for wall 2.

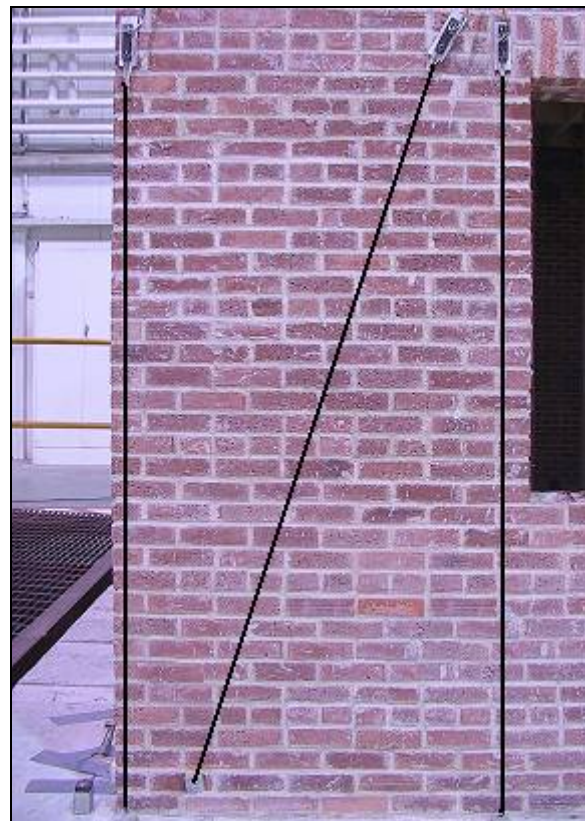


Figure 5-11. Instrumentation on pier 1.

## Sequence of Testing

The testing of the half-scale model was completed in two sets of shake table tests. The preliminary testing, performed on 1 April 2003, consisted of only low level tests. The second set of tests, completed on 8 April 2003, consisted of increasing magnitudes of the Nahanni earthquake until significant damage occurred. The change in natural periods and damping from the undamaged state to the damaged state was determined. White-noise and sine-sweep tests were used to determine the structure's natural periods and sine-decay tests were used to compute damping ratios. All tests were performed at ERDC-CERL on TESS, the Triaxial Earthquake and Shock Simulator.

### *Preliminary Testing*

The primary objective of the preliminary tests was to determine the test model's natural periods and its elastic response to the Nahanni earthquake before testing at levels that could cause damage. Table 5-1 presents the sequence of preliminary tests conducted. The amplitudes of the white-noise and sine-sweep tests (listed as peak accelerations in Table 5-1) were selected such that a clear response was achieved while also ensuring that the building did not sustain any damage. In some cases, the tests were repeated at larger amplitudes to obtain better results. Only the largest-amplitude tests are shown in Table 5-1.

Preliminary testing concluded with two low level unidirectional Nahanni earthquakes, scaled to 9.5% of the full earthquake in the x-direction and 7% of the full earthquake in the y-direction. The goal of these tests was to gain an understanding of the linear-elastic response of the test model and also to use the test results as a verification of the finite element model created in SAP 2000NL. The comparison of the experimental and analytical data helped to determine the accuracy of the SAP model and, consequently, the accuracy of the approximate cracking loads and cracking locations.

**Table 5-1. Sequence of preliminary tests performed on the structure.**

Test	Direction	Type	Peak X Acceleration	Peak Y Acceleration
1	Y	White-Noise	---	0.16 g
2	Y	Sine-Sweep	---	0.02 g
3	X	White-Noise	0.04 g	---
4	X	Sine-Sweep	0.02 g	---
5	X	Nahanni X (9.5%)	0.088 g	---
6	Y	Nahanni Y (7%)	---	0.083 g

The waveform used for the white-noise tests is a randomly generated sequence of excitations at varying frequencies, but with nearly constant amplitude (Figure 5–12). In contrast, the sine-sweep waveform is a sine curve excitation with constant amplitude, but with increasing frequency (Figure 5–13). All of the sine-sweep tests were performed within a range of 5 – 60 Hz. For both the white-noise and sine-sweep tests, the natural periods of the building can be determined by creating a transfer function between an acceleration time history of a point on the building and the acceleration time history of the table (Figure 5–14). The point of resonance in the transfer function marks the natural period of the structure.

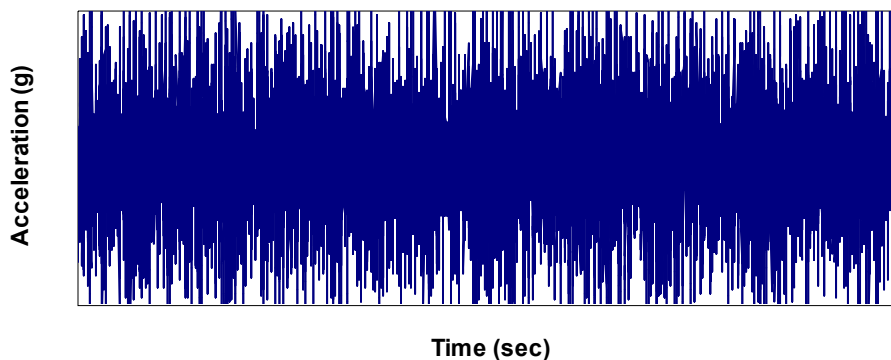


Figure 5–12. Typical white-noise test waveform.

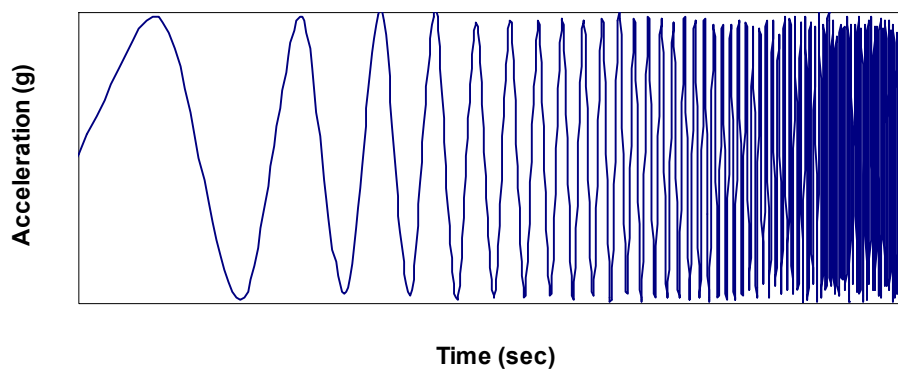


Figure 5–13. Typical sine-sweep test waveform.

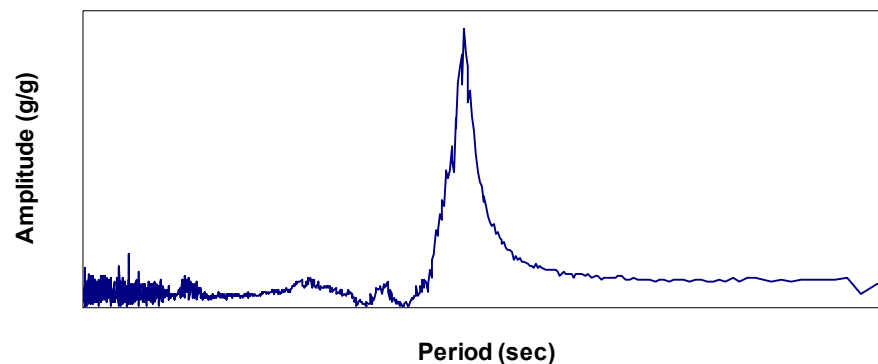


Figure 5–14. Typical transfer function generated by a white-noise test or sine-sweep test.

### ***Damage-Level Testing***

The objective of the damage-level testing was to test at levels that would allow for a description of the 3D linear and nonlinear responses of the test structure under the unidirectional and bidirectional Nahanni earthquake simulations. At the same time, damage of the structure had to be kept to a level that would allow for structural retrofit.

There are two contradicting aspects of URM shake table testing that were considered in creating the test sequence. First, seismic tests should start at a low level and increase at an increment that will allow for a reasonable determination of the load/deformation behavior of the structure. In other words, if the first seismic test is large enough to initiate pier failure, it is very difficult to create an accurate description of the building response because the limiting bounds of load are the applied load and zero. Second, the number of tests should be minimized to reduce the accumulation of damage before large-magnitude tests. Taking into account those considerations and the approximate cracking loads (Table 4-6 through Table 4-8), the decision was made to perform seismic tests at increments of 10 percent of the full Nahanni earthquake. Furthermore, because walls 1 and 2 have the lowest predicted cracking strengths, it was decided that testing would be performed in the x-direction first, followed by the y-direction, and then by the simultaneous xy ground motion. Table 5-2 presents the damage-level sequence of shake table tests. In addition to the Nahanni seismic tests, white-noise tests were performed to determine the test model's natural periods after damage had occurred, and sine-decay tests were performed at the beginning and end of testing to determine the test model's damping ratios before and after damage.

Next to each seismic test listed in Table 5-2 is the percentage of the Nahanni earthquake used for the test. Upon examination, it is clear that the peak ground

acceleration (PGA) for each test is greater than what would be expected for the percentage specified. From Chapter 3, the maximum and minimum ground accelerations of the full Nahanni earthquake in the x-direction are 0.9458 g and -1.0935 g, and in the y-direction earthquakes are 0.9355 g and -0.9723 g. The cause for this discrepancy is due to the connectivity of the shake table actuators. TESS has nine vertical actuators in the z-direction, six horizontal actuators in the x-direction, and two horizontal actuators in the y-direction that must all move together during a test. Consequently, when unidirectional or bidirectional excitation is specified as input for TESS, the actuators associated with the zero degrees of freedom must move as well as those associated with the intended direction(s) of excitation. As a way to compensate for this interaction, TESS generates waveforms for each degree of freedom which, when applied together, are intended to produce the desired excitation accelerations. This procedure is not exact on the first attempt, however, and numerous iterations may be needed to refine the waveforms. Furthermore, this process is dependent upon the magnitude of the accelerations; therefore, iterations would be required for each seismic test in order to produce an exact scale replica of the Nahanni earthquake. Due to the fragility of the URM test model, it was decided that the potential damage resulting from refining the test motions was not acceptable and that the process could be performed only once at a low level. As a consequence of this decision, the actual magnitudes of the applied ground motions were larger than intended and accelerations of notable magnitude occurred in degrees of freedom that were supposed to be zero.

**Table 5-2. Sequence of damage-level tests performed on the structure.**

Test	Direction	Type	Peak X Acceleration	Peak Y Acceleration
7	X	Sine-Decay	0.04 g	---
8	Y	Sine-Decay	---	0.06 g
9	X	Nahanni X (10%)	0.135 g	0.010 g
10	Y	Nahanni Y (10%)	0.019g	0.143 g
11	X + Y	Nahanni X (10%) + Nahanni Y (10%)	0.142 g	0.142 g
12	X	Nahanni X (20%)	0.368 g	0.035 g
13	Y	Nahanni Y (20%)	0.049 g	0.318 g
14	X + Y	Nahanni X (20%) + Nahanni Y (20%)	0.281 g	0.315 g
15	X	Nahanni X (30%)	0.558 g	0.053 g
16	Y	Nahanni Y (30%)	Error: Data Not Recorded	

Test	Direction	Type	Peak X Acceleration	Peak Y Acceleration
17	X + Y	Nahanni X (30%) + Nahanni Y (30%)	0.518 g	0.605 g
18	X	Nahanni X (40%)	0.772 g	0.191 g
19	X	White-Noise	0.04 g	---
20	Y	White-Noise	---	0.04 g
21	X	Sine-Decay	0.04 g	---
22	Y	Sine-Decay	---	0.06 g

The waveform used for the sine-decay tests is constant in amplitude and in frequency. The frequency is set at a level just above the test structure's natural frequency to ensure that the building responds clearly and also to ensure that if damage were to occur during the test, the structure would not shift into a resonance. The waveform is applied for a period of time and then suddenly stopped, allowing the test structure to vibrate freely. The free vibration portion of the building accelerometer records is used to calculate the damping ratio. A typical sine-decay test building accelerometer record is shown in Figure 5-15.

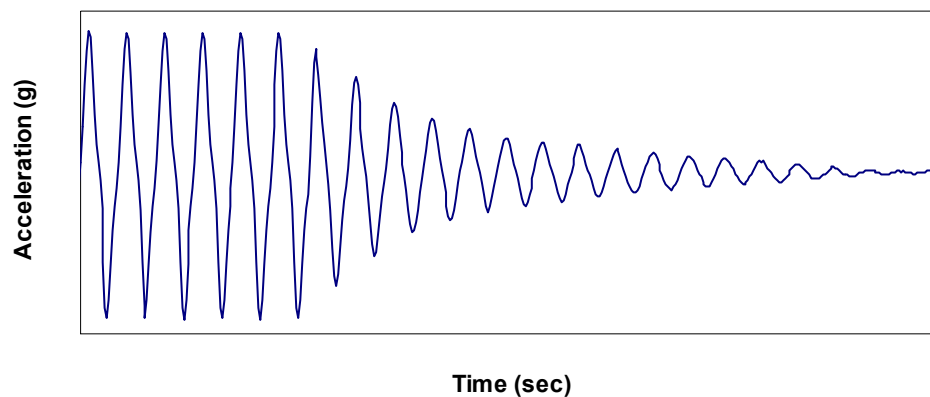


Figure 5-15. Typical building response to sine-decay test.

## Testing of Half-Scale Model

The testing of the half-scale model progressed according to the preliminary test schedule and the damage-level test schedule presented in Table 5-1 and Table 5-2, respectively.

### ***Natural Frequencies and Damping (Undamaged State)***

White-noise and sine-sweep tests were conducted to determine the natural periods of the undamaged test model. The Seismic Test EXecution (STEX) software application, developed and licensed by MTS Systems Corp., was used to generate transfer functions between accelerations recorded at the floor and roof levels of the model and the ground acceleration. The following data channel locations were used: the corner of walls A and 2 (A11x, A11y, A21x, A21y), the corner of walls B and 1 (A15x, A15y, A25x, A25y), and the center of the diaphragm (A19x, A19y, A29x, A29y). Table 5-3 presents the natural periods of the undamaged building calculated by the transfer functions for the white-noise and sine-sweep tests. As can be seen from the table, the two tests produced very similar results.

**Table 5-3. Results from white-noise and sine-sweep tests on undamaged building (sec).**

Direction	Data Channel	White-Noise Test		Sine-Sweep Test	
		Period	Average	Period	Average
X-Direction	A11x	0.08828	0.08828	0.08752	0.08752
	A15x	0.08828		0.08752	
	A19x	0.08828		0.08752	
	A21x	0.08828		0.08752	
	A25x	0.08828		0.08752	
	A29x	0.08828		0.08752	
Y-Direction	A11y	0.11130	0.11296	0.11253	0.11253
	A15y	0.11506		0.11253	
	A19y	0.11253		0.11253	
	A21y	0.11130		0.11253	
	A25y	0.11506		0.11253	
	A29y	0.11253		0.11253	

In addition to the white-noise and sine-sweep tests, sine-decay tests were performed prior to seismic testing to determine the damping of the undamaged structure. The damping ratio (percentage of critical damping) can be determined from the acceleration response recorded at a building location when the structure is under free vibration. The following equation was used to determine the damping ratio,  $\zeta$ , from an acceleration record generated by a sine-decay test (Chopra 2001):

$$\zeta = \frac{1}{2\pi\eta} \ln \frac{\ddot{u}_i}{\ddot{u}_{i+j}} \quad \text{Equation 5-1}$$

where  $\ddot{u}_i$  is a peak acceleration during the free vibration portion of the test and  $\ddot{u}_{i+j}$  is the peak acceleration  $j$  vibration cycles after  $i$ . The damping ratio was calculated at the same locations used to calculate the natural periods for the white-noise and sine-sweep tests. Table 5-4 presents the results of the sine-decay tests conducted on the undamaged structure.

**Table 5-4. Results from sine-decay tests on undamaged building.**

Direction	Data Channel	Percent Damping	Average
X-Direction	A11x	3.38%	4.37%
	A15x	3.41%	
	A19x	4.50%	
	A21x	5.53%	
	A25x	4.23%	
	A29x	5.18%	
Y-Direction	A11y	17.98%	13.02%
	A15y	6.51%	
	A19y	20.69%	
	A21y	15.62%	
	A25y	5.54%	
	A29y	11.80%	

### **Seismic Test Observations at Low-Level Excitation**

The low-level tests included the 10% and 20% unidirectional and bidirectional Nahanni earthquake simulations. During these tests, the structure remained visibly linear-elastic until the last test of the sequence (20%-XY), which initiated cracking in a few of the test model's piers. Table 5-2 lists the PGAs recorded for each of the low-level tests.

During the 10% unidirectional and bidirectional tests, the shaking of the table was only slightly visible. When the intensity of the unidirectional earthquakes was increased to the 20% level, indications of damage could be heard in the form of loud popping, although visible damage was not apparent. The 20%-XY earthquake initiated cracking on piers 8, 9, and 11 (see Figure 4–1 for pier numbers). A crack formed along the entire base of pier 11 and a very small crack formed along the edge of the masonry lintel above the door adjacent to pier 8. The most extensive damage appeared on pier 9, which developed long horizontal cracks along its base and at a vertical level just above the top of the adjacent door (Figure 5–16). The gray horizontal lines directly above the door and the window shown in Figure 5–16 indicate the locations of the WT 5x6 steel lintels.

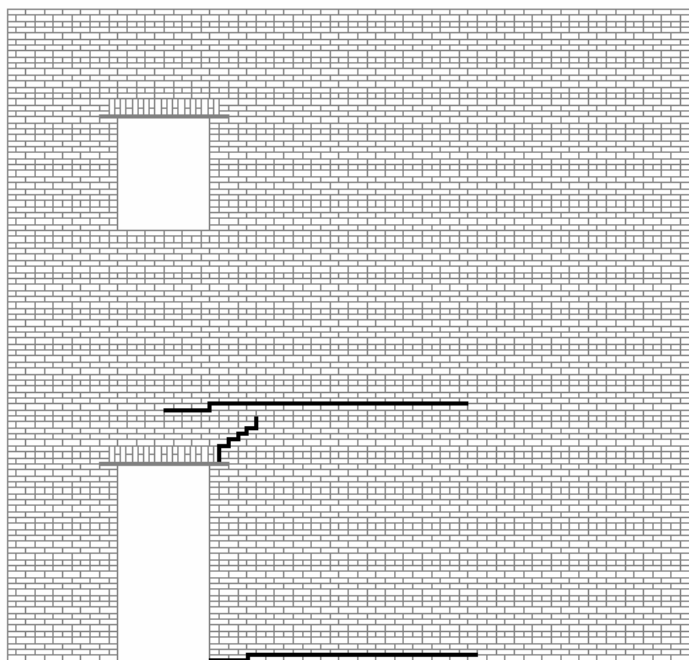


Figure 5-16. Crack locations in wall 1 after 20%-XY seismic test.

### ***Seismic Test Observations at High Level Excitation***

This set of tests included the last four seismic tests performed, which were the 30%-X, 30%-Y, 30%-XY, and 40%-X tests. Table 5-2 lists the PGA recorded for each of the high-level tests except for the 30%-Y test, which was not recorded due to an error in the data acquisition system.

The first test of this group, 30%-X, did not increase the visible damage of the structure. However, the 30%-Y test caused significant damage in the piers of wall 2, as cracks formed along the top and bottom of piers 11 and 12, allowing them to rock. Piers 8 and 4, adjacent to piers 11 and 12, respectively, also rocked during the 30%-Y test as a result of the twisting of the structure. The combination of base shears resulting from the horizontal earthquake components became evident during the 30%-XY test. A portion of all of the piers of wall A cracked, while none of the uncracked piers in wall B (piers 5, 6, and 7) demonstrated any apparent damage. The 30%-XY test also caused piers 11 and 12 to rock and sustain lateral displacements of approximately 0.25 in. At this point during the test sequence, the decision was made not to test in the y-direction again due to the extensive damage that had occurred in wall 2. The final seismic test conducted was the 40%-X test, which initiated rocking in all of the piers of wall A. In addition, permanent offsets of approximately 0.0625 in. were noticed at the tops of piers 4 and 8 at locations where horizontal cracks stepped up a wythe. This damage signaled a shift of those piers away from the remainder of the test

model. The final cracking patterns of each of the walls in the test model are shown in Figure 5–18, Figure 5–19, Figure 5–20, and Figure 5–21.

After the completed seismic testing, the diaphragms were examined for visible signs of damage, such as withdrawal of nails, deformation of the sheathing at nail holes, and splitting of the sheathing or joists. There were no signs of damage, and consequently, it is believed that the diaphragms remained linear-elastic throughout testing.

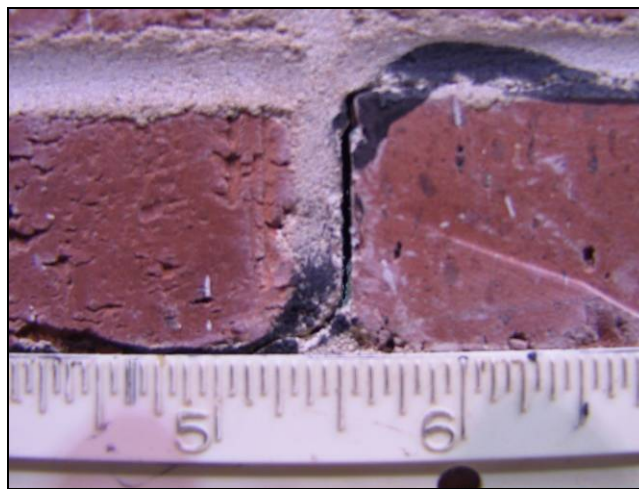


Figure 5–17. Permanent offset at the top of pier 4 after completed seismic testing.

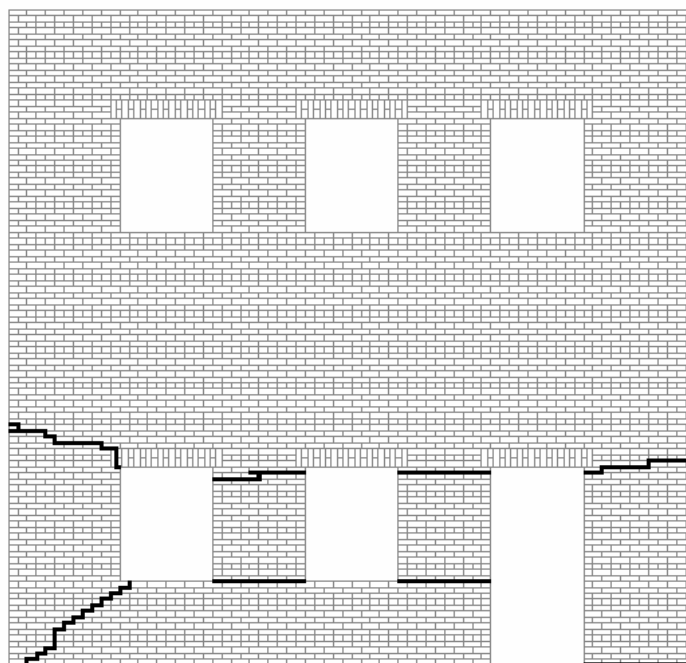


Figure 5–18. Crack locations in wall A after completed seismic testing.

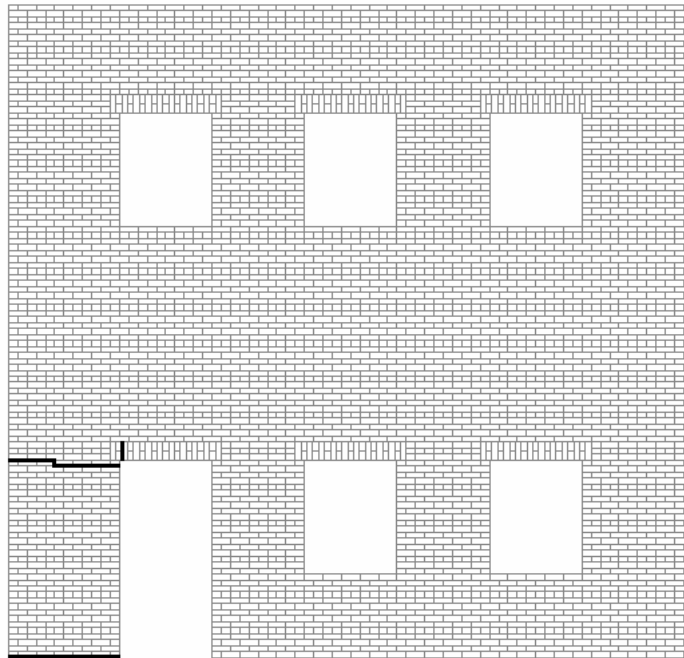


Figure 5–19. Crack locations in wall B after completed seismic testing.

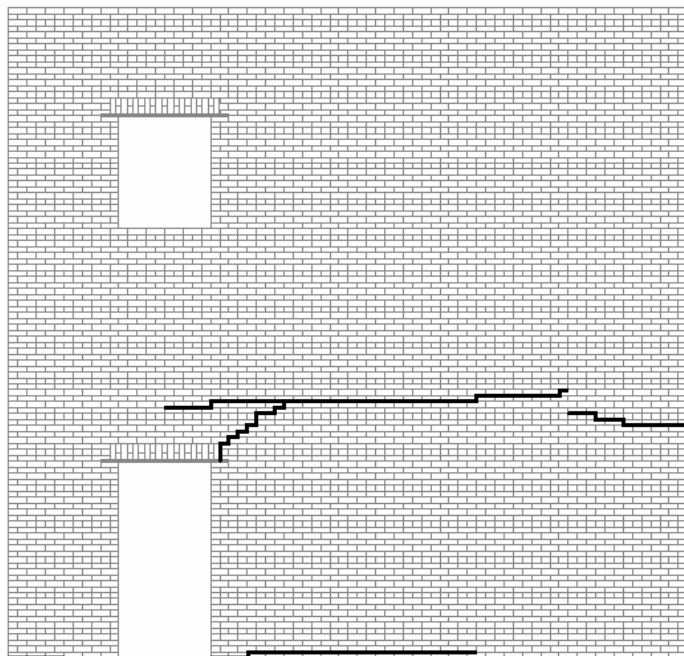


Figure 5–20. Crack locations in wall 1 after completed seismic testing.

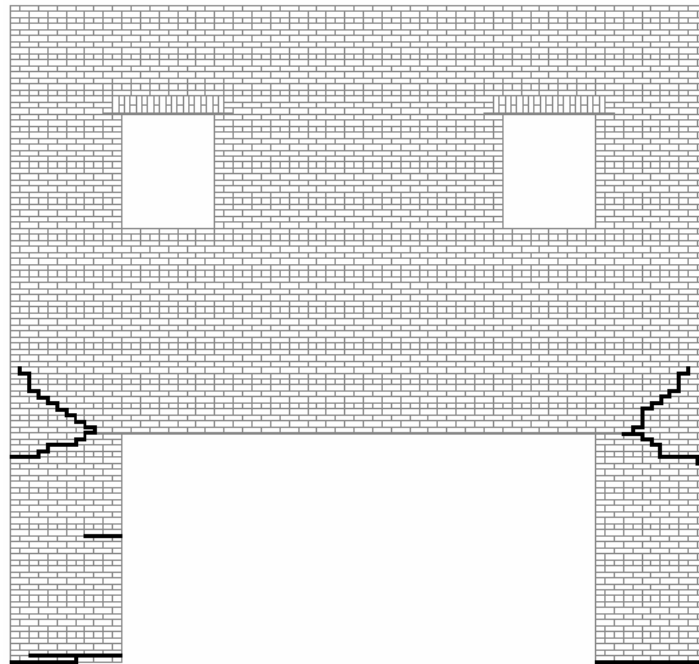


Figure 5-21. Crack locations in wall 2 after completed seismic testing.

### ***Natural Frequencies and Damping (Final Damage State)***

White-noise tests were conducted at the end of seismic testing to determine the change in the natural periods of the test model from the undamaged state to the damaged state. Sine-sweep tests were not performed because the natural periods calculated by the two test methods were very similar for the undamaged model (Table 5-3). STEX was used to generate transfer functions at the same locations used previously. Table 5-5 presents the results of the white-noise tests for the x-direction and the y-direction. As expected, the damage withstood by the test model lengthened the fundamental periods considerably. In addition to the white-noise tests, sine-decay tests were also performed at the end of damage-level testing. Table 5-6 presents the computed damping ratios from the sine-decay tests and indicates that damping increased after damage had occurred.

**Table 5-5. Results from white-noise test on damaged building (sec).**

Direction	Data Channel	Period	Average
X-Direction	A11x	0.09660	0.09691
	A15x	0.09846	
	A19x	0.09660	
	A21x	0.09660	
	A25x	0.09660	
	A29x	0.09660	
Y-Direction	A11y	0.11907	0.11907
	A15y	0.11907	
	A19y	0.11907	
	A21y	0.11907	
	A25y	0.11907	
	A29y	0.11907	

**Table 5-6. Results from sine-decay tests on damaged building.**

Direction	Data Channel	Percent Damping	Average
X-Direction	A11x	5.47%	6.91%
	A15x	6.37%	
	A19x	6.43%	
	A21x	8.62%	
	A25x	5.81%	
	A29x	8.75%	
Y-Direction	A11y	27.77%	23.73%
	A15y	21.29%	
	A19y	14.19%	
	A21y	26.78%	
	A25y	24.66%	
	A29y	27.69%	

## 6 Evaluation of Test Model Behavior

The following aspects of the measured building response are examined in terms of the overall objectives of this research:

- the force/deformation relationships for each wall
- the amplification of the ground acceleration by the walls and the diaphragms
- the effect, if any, that the flange portions of out-of-plane walls have on the strength of in-plane walls
- the vertical distribution of lateral forces
- the combinational effect of bidirectional base motions on the test model.

### Force/Deformation Relationships of Walls

The force/deformation responses of the masonry walls were determined by plotting the peak base shear and peak lateral displacement of the first floor of the wall for each seismic test that contained an in-plane component for the wall under consideration. Points were generated for walls A and B from the x-direction and simultaneous xy-direction earthquakes, and points were generated for walls 1 and 2 from the y-direction and simultaneous xy-direction earthquakes. The global displacement transducers D11x and D13x measured the displacement of walls A and B, respectively, while the global displacement transducers D17y and D11y measured the displacement of walls 1 and 2, respectively (Figure 5–5). The displacement of the table was subtracted from the measured displacements in order to determine the deformation of the walls.

The applied seismic forces were calculated by multiplying the acceleration time histories recorded during testing and the building mass tributary to each accelerometer. The test model was divided into a six-degrees-of-freedom system, with a degree of freedom associated with the acceleration of each in-plane masonry wall at the floor level, the acceleration of the floor diaphragm, the acceleration of each in-plane masonry wall at the roof level, and the acceleration of the roof diaphragm (Figure 6–1). The vertical distribution of mass was determined by dividing the story heights by 2 and assigning the mass within the divisions to the ad-

jacent floor level. The horizontal distribution of mass was determined by assuming that the mass located in the inner 50% of the transverse building dimension was tributary to the diaphragm, while the outer 25% on each side were assumed to be tributary to the in-plane walls. Based on the vertical and horizontal divisions, the mass tributary to each degree of freedom was calculated for ground motion in both horizontal plan directions (Table 6-1). Force/time histories were generated by multiplying the tributary weights and the associated acceleration time history (units in g). To determine the force in the first floor of a given wall, the force/time histories of the first and second floors of that wall are added along with half of the force/time histories for the floor and roof diaphragms (per standard lateral force distribution for a flexible diaphragm). The directions of the seismic forces are automatically accounted for since time history responses were added, as opposed to peak responses. Figure 6-2 is an example of a computed force time history for Wall A.

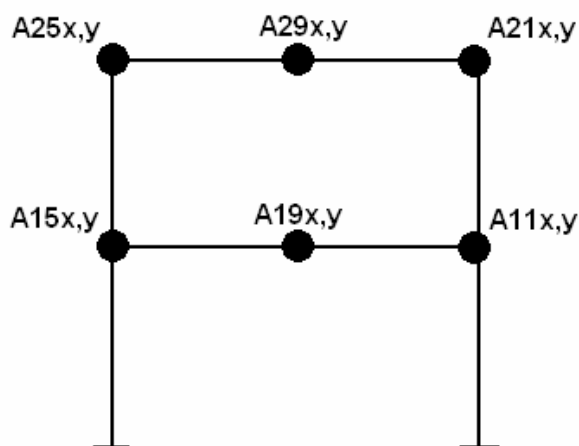


Figure 6-1. Six-degree-of-freedom model used to compute seismic forces.

Table 6-1. Mass associated with test model degrees of freedom for ground motion in the x-direction and y-direction.

**For Loads in the X-Direction (All units pounds unless otherwise stated)**

**For Seismic  
Forces  
Multiply By:**

At Roof Level							
Element	Diaphragm Lead	Out-of-Plane Wall Lead	In-Plane Wall Lead	URM	Diaphragm	Total (kips)	
Diaphragm	1021.00	1110.00	0.00	1423.33	225.00	3.78	
Wall A	989.50	480.00	1035.00	2563.33	112.50	5.18	
Wall B	989.50	480.00	1035.00	2506.67	112.50	5.12	→ A25x
At Floor Level							
Element	Diaphragm Lead	Out-of-Plane Wall Lead	In-Plane Wall Lead	URM	Diaphragm	Total (kips)	
Diaphragm	1021.00	2910.00	0.00	2409.14	225.00	6.57	
Wall A	989.50	1290.00	2745.00	4910.50	112.50	10.05	
Wall B	989.50	1290.00	2745.00	4837.58	112.50	9.97	→ A15x

**For Loads in the Y-Direction (All units pounds unless otherwise stated)**

At Roof Level							
Element	Diaphragm Lead	Out-of-Plane Wall Lead	In-Plane Wall Lead	URM	Diaphragm	Total (kips)	
Diaphragm	1020.00	1110.00	0.00	1857.33	225.00	4.21	
Wall 1	990.00	480.00	1035.00	2355.78	112.50	4.97	
Wall 2	990.00	480.00	1035.00	2280.22	112.50	4.90	→ A21y
At Floor Level							
Element	Diaphragm Lead	Out-of-Plane Wall Lead	In-Plane Wall Lead	URM	Diaphragm	Total (kips)	
Diaphragm	1020.00	2910.00	0.00	3619.33	225.00	7.77	
Wall 1	990.00	1290.00	2745.00	4465.61	112.50	9.60	
Wall 2	990.00	1290.00	2745.00	4072.28	112.50	9.21	→ A11y

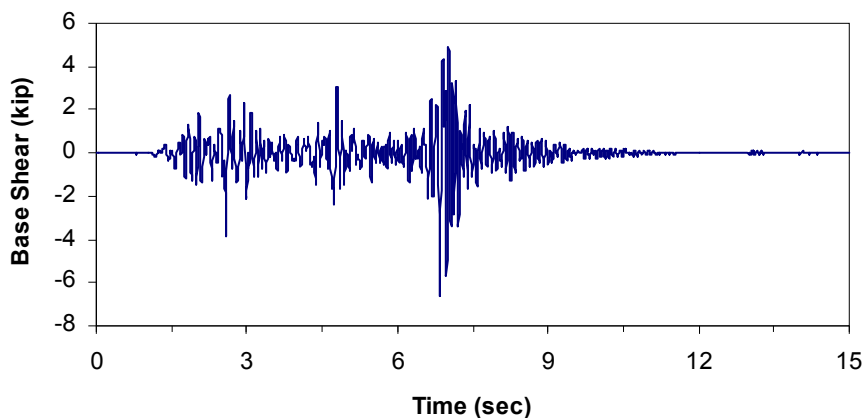


Figure 6–2. Applied base shear on wall A during 20%-X test.

Using the generated force/time histories, the peak force and peak first-floor displacement of each wall was plotted for seismic tests containing an in-plane component for the wall under consideration. The combination of the points creates a backbone curve for the behavior of the wall. Figure 6–3 through Figure 6–6 are graphs of the force/deformation response of each wall. The experimental data points are plotted discretely, while a bilinear best-fit curve is also plotted for visualization purposes. The bilinear curve was created by combining two best fit lines: one associated with data points corresponding to the linear-elastic response and one associated with data points corresponding to the plastic response.

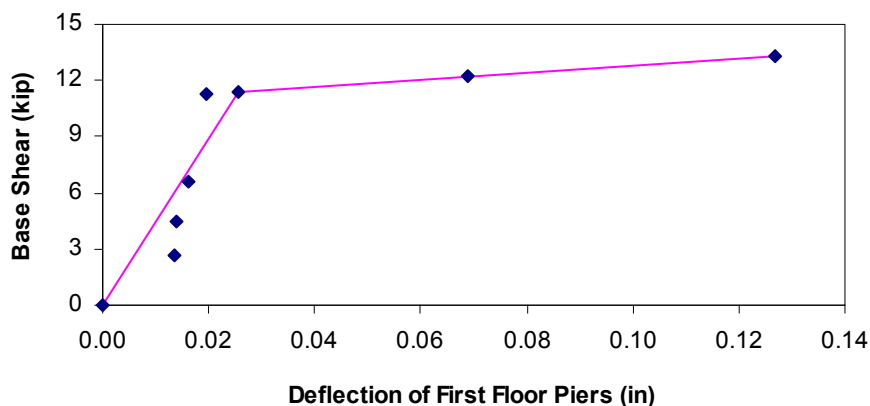


Figure 6–3. Plot of experimental force/deformation response of wall A.

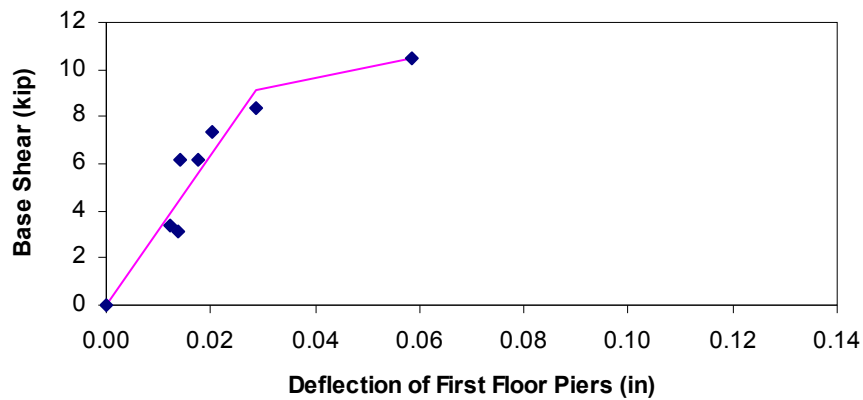


Figure 6-4. Plot of experimental force/deformation response of wall B.

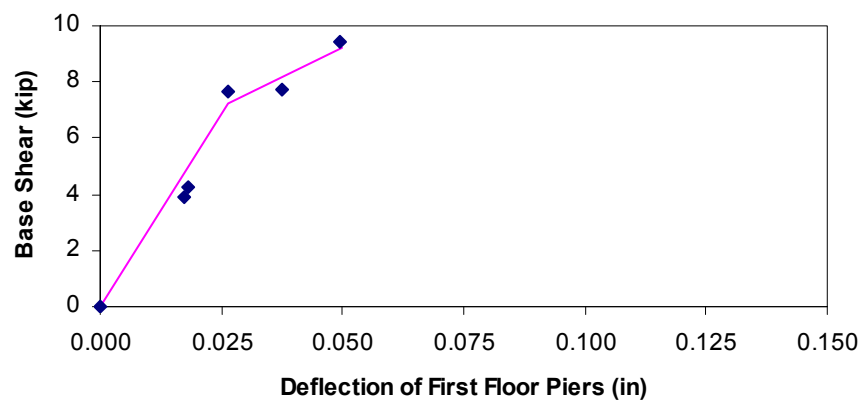


Figure 6-5. Plot of experimental force/deformation response of wall 1.

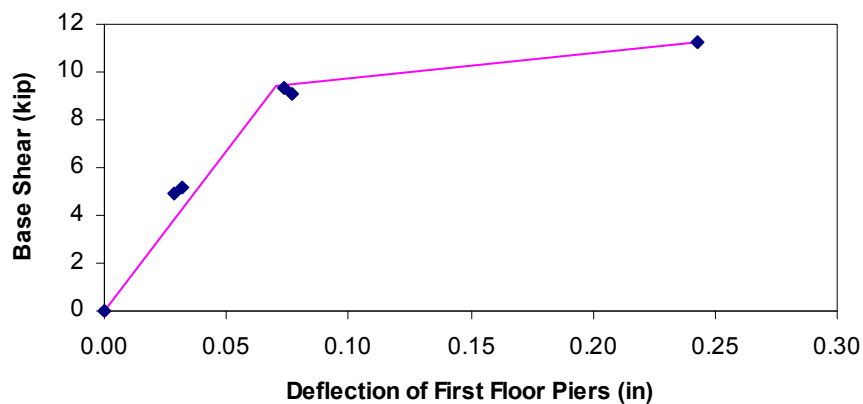


Figure 6-6. Plot of experimental force/deformation response of wall 2.

Figure 6–3 and Figure 6–6 show that both wall A and wall 2 demonstrated stable rocking behaviors, with ductilities of 5.0 and 3.5, respectively. Here, ductility is defined as the maximum displacement value divided by the yield displacement value. Walls B and 1, by comparison, sustained maximum displacements of approximately twice their yield displacements, indicating that they had experienced cracking (although a visible failure mechanism was not evident).

There is no indication from the force/deformation curves of wall A and wall 2 that the maximum wall displacements measured during testing are near the displacements that would cause collapse. Recall that testing was stopped not due to the model's loss of stability but to prevent damage from propagating to an extent that would prohibit retrofit and further testing. Costley and Abrams (1996) recorded ductilities ranging from 6.0 to 10.0 for a structure similar to the test model used in this study.

An important observation of Figure 6–5 and Figure 6–6 is that walls 1 and 2 exhibited strengths that were significantly larger than their predicted strengths (Figure 4–6 and Figure 4–7). The explanation of the unexpected strength of wall 1 lies in the incorrect assumption that pier 9 would behave as a cantilevered pier. Based on the final crack pattern of wall 1, shown in Figure 5–20, pier 9 behaved as a fixed-fixed pier with a height of 56 in. Using these dimensions and boundary conditions, pier 9 has a capacity of 12.7 kips, increasing the strength of wall 1 to 13.5 kips. This value correlates fairly well with Figure 6–5 considering that wall 1 had not visibly failed and may have retained additional strength. With regard to wall 2, the failure mode was correctly predicted, as well as the assumed pier height. Therefore, the additional strength must be due to factors outside of those normally considered. Possible explanations may include the beneficial effects of compressive overturning moment and the participation of the out-of-plane walls' flanges. The viability of these explanations is examined later in this chapter.

In addition to Figure 6–3 through Figure 6–6, force/deformation plots were also generated using displacements obtained from double integrating accelerometer time histories recorded during testing. There were several justifications for creating the additional curves. First and foremost, a comparison of the measured and integrated displacements allowed for a verification of the recorded test data. Second, the resolution of the experimental acceleration records was considerably better than that of the displacements since the building displacements were so small (especially in the linear-elastic region); therefore, it was thought that use of integrated displacements might reduce the data point scatter. Finally, there was concern that the vibration of the steel wire connecting the global displace-

ment transducers to the test model (see Chapter 5) contributed additional displacement to the building displacement.

Figure 6–7 through Figure 6–10 present the force/deformation curves created with the integrated displacements for each wall in the test model. For comparison purposes, the bilinear best-fit curve for the measured displacements is shown as a dashed line in the figures. The plots clearly indicate reduced data point scatter and increased stiffness (decreased displacement), as was expected. The only exception to this statement is Figure 6–10, which is not surprising since the displacements recorded on wall 2 were considerably larger than on the other walls and therefore less susceptible to the introduced errors.

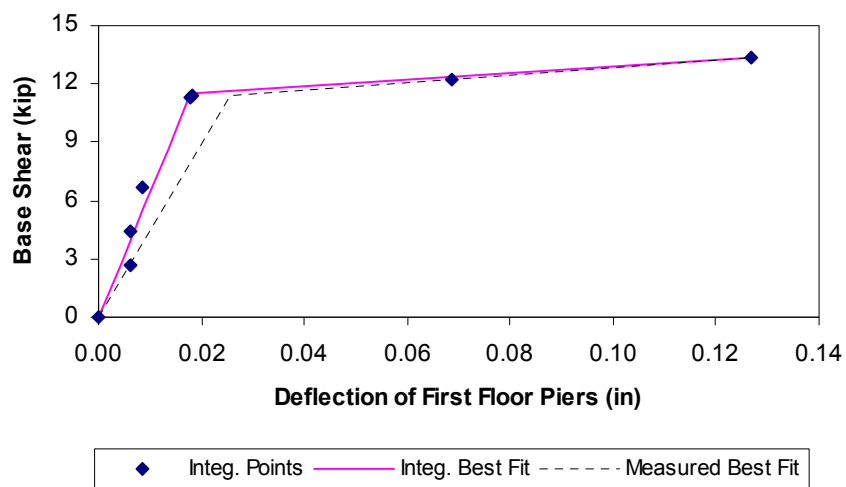


Figure 6–7. Plot of experimental force/deformation response of wall A (integrated displacement).

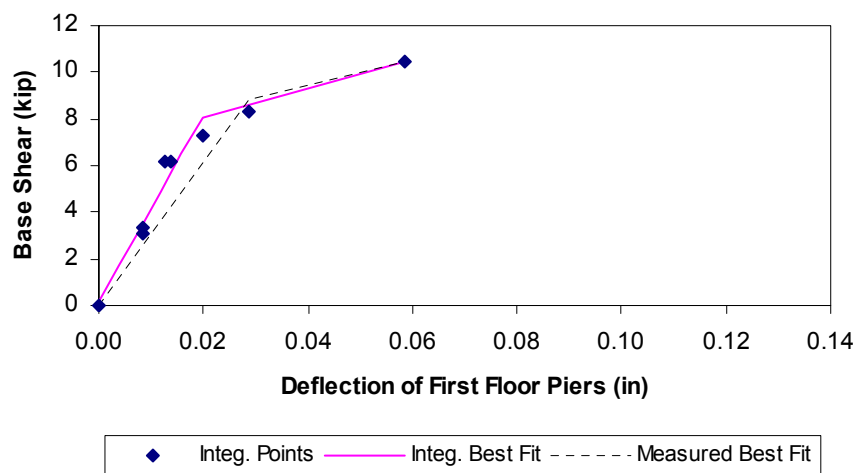


Figure 6–8. Plot of experimental force/deformation response of wall B (integrated displacement).

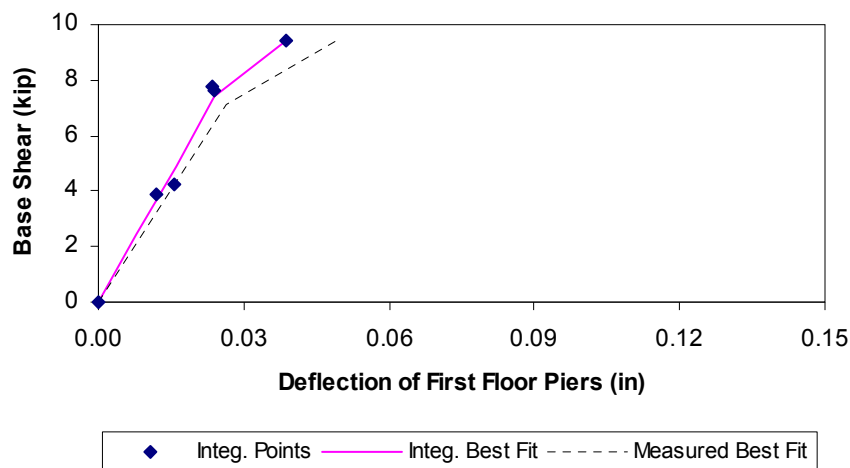


Figure 6–9. Plot of experimental force/deformation response of wall 1 (integrated displacement).

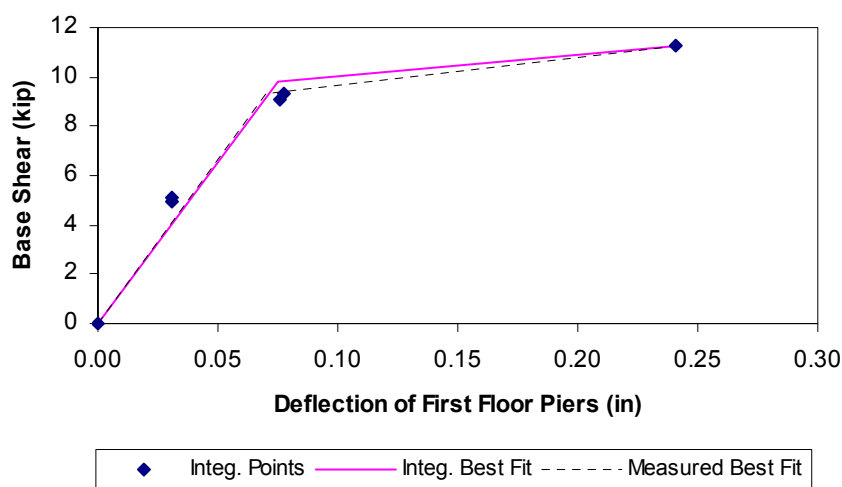


Figure 6–10. Plot of experimental force/deformation response of wall 2 (integrated displacement).

## Acceleration Amplifications

The in-plane walls of a structure act as initial modifiers of the earthquake ground motion as it propagates through the building. When the accelerations reach the floor levels, they excite the diaphragms, which act as secondary modifiers of the ground motion. Previous research has shown that for URM systems with flexible diaphragms, the diaphragm amplification of the input accelerations is usually 200% – 400%, depending on the intensity of the ground motion (Kariotis 1995).

The test model's wall and diaphragm amplification factors for unidirectional x-direction motion are plotted in Figure 6–11 through Figure 6–14. Figure 6–11 presents the wall A and wall B amplification at the floor and roof levels versus the PGA, calculated as the peak acceleration measured at the specified building location divided by the PGA. The data point sets at  $\text{PGA} = 0.368 \text{ g}$  and  $\text{PGA} = 0.558 \text{ g}$  demonstrate twisting of the structure, leading to an increased response of wall A and a decreased response of wall B. This behavior is surprising given the symmetry of walls A and B and the fact that the ground motion was intended to be unidirectional. However, as noted in Chapter 5, the interaction of the shake table actuators results in ground motion components in all six degrees of freedom. The recorded test data indicated that the y-direction and yaw rotation (i.e., rotation about the vertical axis) components have peak accelerations that are concurrent with the peak acceleration in the x-direction, and are directed such that they would increase the acceleration of wall A and decrease the acceleration of wall B. It is believed that this response caused the twisting shown in Figure 6–11, and that the building's behavior was not due to a torsional response incited by the frequency content of the x-direction ground motion. In general, the average wall amplification is close to 1.0, with slightly larger amplifications at the roof level than at the floor level (Figure 6–12).

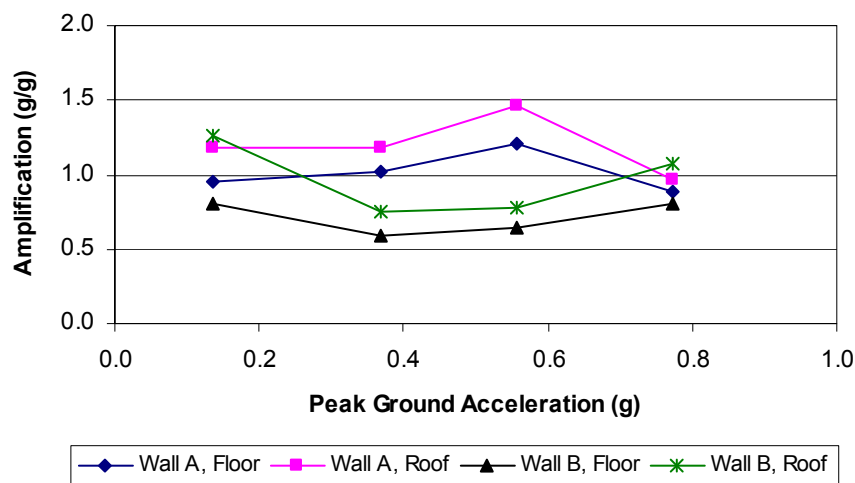


Figure 6–11. Wall A and wall B amplification of ground acceleration in the x-direction.

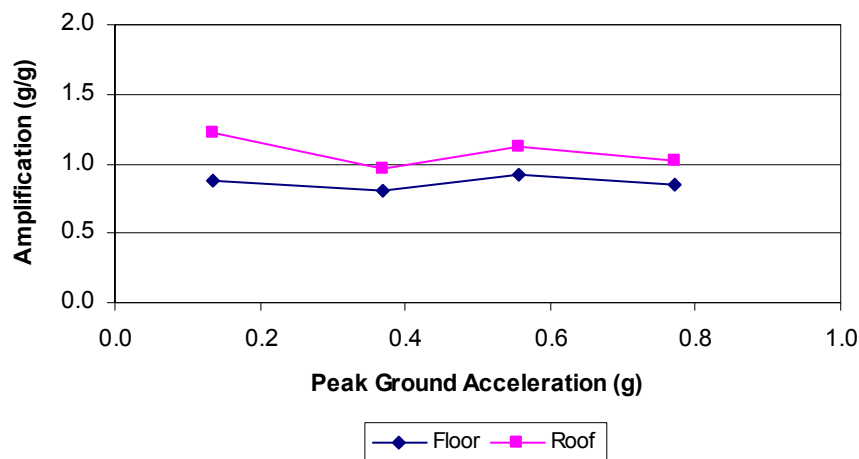


Figure 6-12. Average wall amplification of ground acceleration in the x-direction.

Figure 6-13 and Figure 6-14 present the diaphragm amplification of the average wall acceleration and the ground acceleration, respectively, at the floor and roof levels. The diaphragm amplification of the average wall acceleration was computed by dividing the peak diaphragm acceleration by the average of the peak in-plane wall accelerations (in this case, walls A and B). The diaphragm amplification of the ground acceleration was determined in the same manner as Figure 6-11. The calculated amplification factors are consistent with the low end of the expected response for flexible diaphragms. Furthermore, the figures indicate a reduction in amplification during rocking of the wall A piers (PGA of 0.772 g).

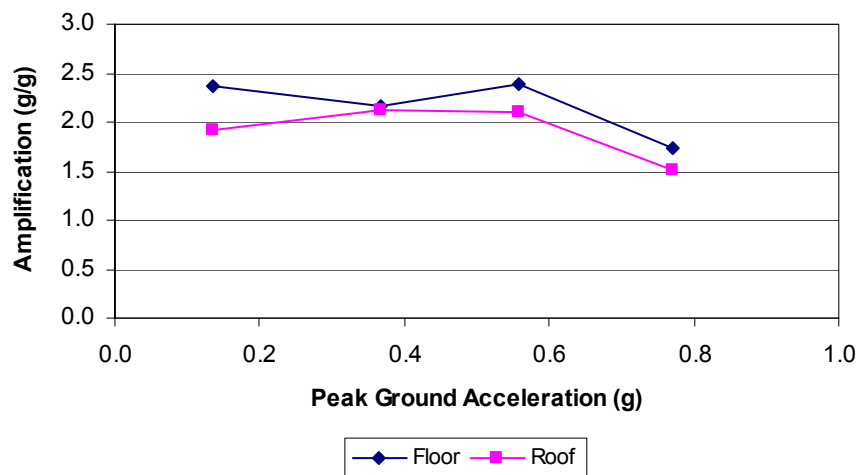


Figure 6-13. Floor and roof diaphragm amplification of average wall acceleration in the x-direction.

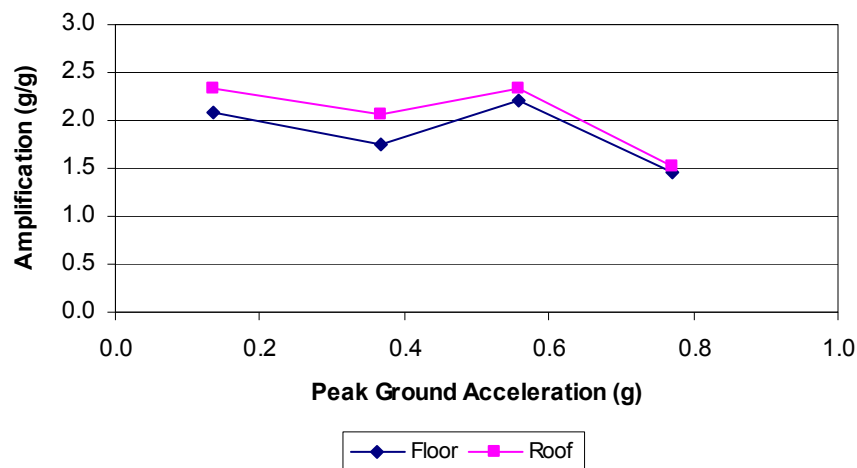


Figure 6–14. Floor and roof diaphragm amplification of ground acceleration in the x-direction.

Figure 6–15 through Figure 6–18 plot the wall and diaphragm amplification factors for ground motion in the y-direction. The first two data point sets were generated from the 10%-Y and 20%-Y tests, while the last data point set was created using the 30%-XY test (since there was a recording error during the 30%-Y test). The wall amplifications for y-direction tests were considerable at low-level excitation (Figure 6–15). In particular, the peak roof acceleration on wall 2 was close to 2 times greater than the peak ground acceleration. As expected, the wall 1 amplifications, while notable, were significantly smaller than the wall 2 amplifications. As the ground motion intensity was increased, the wall amplifications decreased greatly and converged to a value of approximately 1.0 at a PGA of 0.605 g.

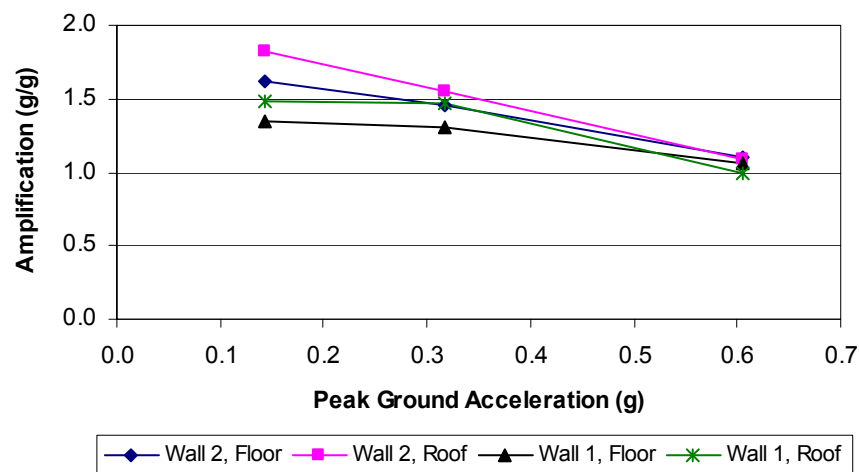


Figure 6–15. Wall 1 and wall 2 amplification of ground acceleration in the y-direction.

The diaphragm amplifications of the average wall acceleration and the ground acceleration for excitation in the y-direction (Figure 6–17 and Figure 6–18) produced an unexpected result: the roof amplification was much larger than the floor amplification. Based on the deflected shape of the diaphragms (Figure 6–16), it is clear that the floor deformed primarily through shear while the roof deformed through shear and bending. This fact is not surprising since at the first-floor level, the lateral stiffness of wall 2 is only 40% of the stiffness of wall 1 (based on experimental results), while at the second-floor level, the lateral stiffness values of the walls are most likely very similar. In other words, at the first-floor level, wall 2 does not provide the rigidity needed to develop bending (and amplified accelerations) in the diaphragm, and consequently the deformed shape is rhomboidal. The deflections at the first-floor level are transmitted to the roof through the continuity of the walls, but due to the increase in stiffness of the second story relative to the first story, acceleration amplification and bending do occur in the roof diaphragm.

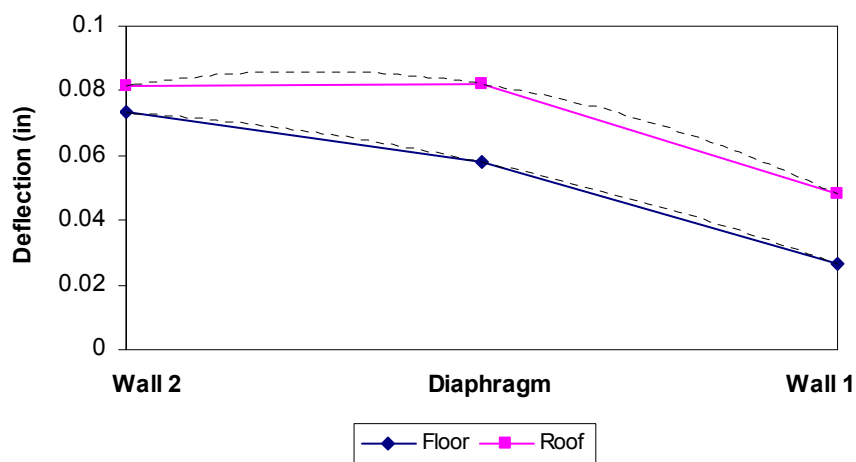


Figure 6–16. Deflected shape of diaphragms during 20%-Y test (with quadratic best fit).

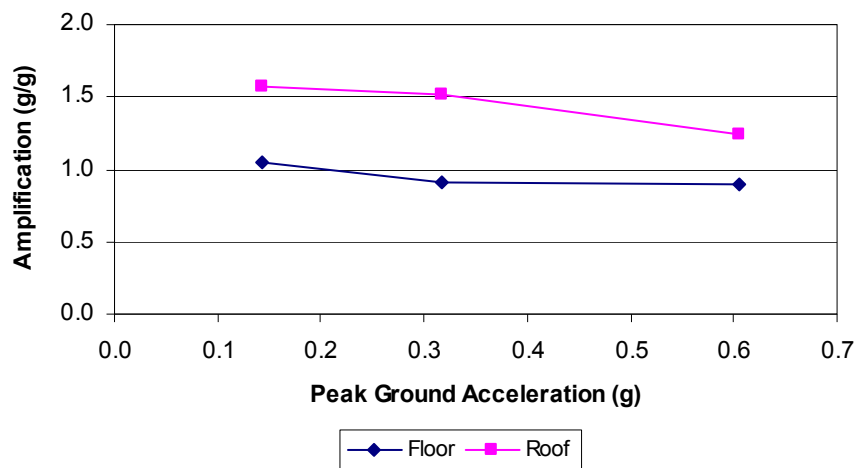


Figure 6-17. Floor and roof diaphragm amplification of average wall acceleration in the y-direction.

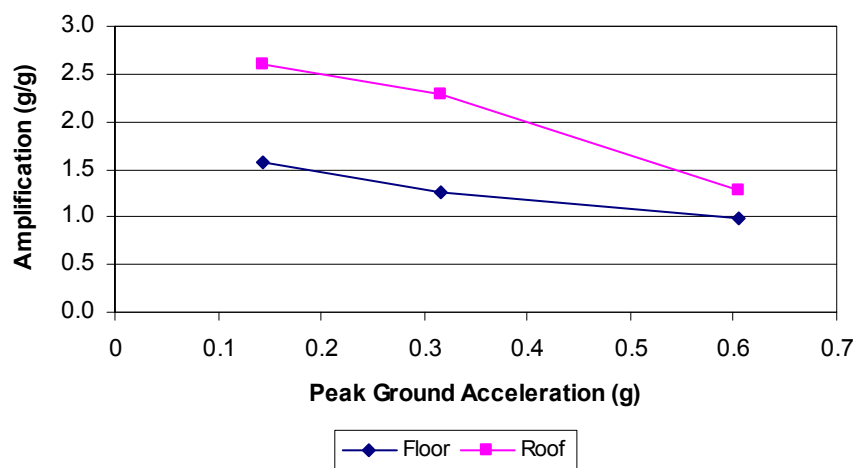


Figure 6-18. Floor and roof diaphragm amplification of ground acceleration in the y-direction.

### ***Behavior of Flanges in Out-of-Plane Walls***

Currently, the effects of out-of-plane wall flanges are not included in calculating the strength of an in-plane wall. This principle is based on studies comparing the response of continuous and discontinuous perpendicular walls, which indicate that flanges have a negligible effect on in-plane wall capacities (Paquette and Bruneau 2003). The first section of this chapter, “Force/Deformation Relationships of Walls,” raised the issue that walls 1 and 2 displayed capacities considerably greater than those predicted by standard methods. It had been incorrectly assumed that pier 9 would behave as a cantilevered pier, which resulted in a predicted strength for wall 1 that was only 25% of what it should have been.

However, similar errors were not made in the assumptions for computing the strength of wall 2, so two possible alternative explanations were offered: increased strength due to compressive overturning moment and/or increased strength due to flange effects.

The behavior of piers 11 and 12 is different from the behavior of the other outer piers in the test model in the sense that they actually form an isolated L-shaped pier with their adjacent out-of-plane wall piers (piers 8 and 4, respectively). During testing, a horizontal crack formed at the tops of the combined pier cross-sections, forcing the corner piers to rock together (Figure 6–19). That response is unlike the case where a perforated shear wall is connected to a plane masonry wall, a setup that was used in many studies that examined flange behavior.

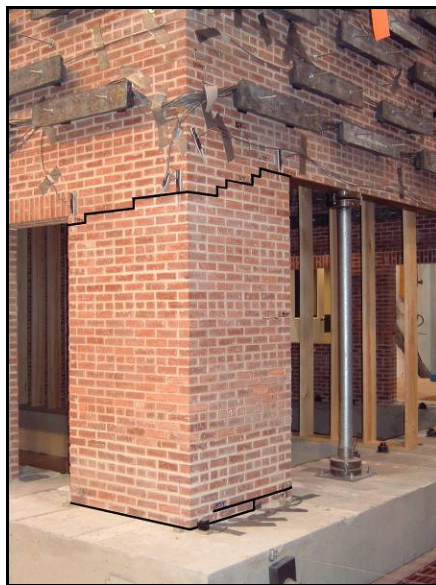


**Figure 6–19. Crack pattern on pier 12 and pier 4 indicating structural continuity.**

To attempt to quantify the flange effects contributing to the strength of wall 2, the rocking capacities of piers 11 and 12 were calculated to include the vertical force due to overturning. Since an accurate estimate of the vertical forces applied to piers 11 and 12 cannot be readily determined based on the recorded test data, SAP 2000 was used to predict the vertical forces applied to the piers during the 30%-XY earthquake. This ground motion was selected because wall 2 exhibited its greatest strength (11.2 kips) during the test. The strengths of pier 11 and pier 12 were calculated separately on a time history basis, according to the FEMA 356 rocking equation (both piers rocked during the 30%-XY test):

$$V_r = 0.9\alpha P_E \left( \frac{L}{h_{eff}} \right) \quad \text{Equation 6-1}$$

where  $P_E$  is the vertical force computed by SAP 2000. If  $P_E$  was less than zero (tensile),  $V_r$  was taken to be zero. The calculated rocking strengths were then summed to determine the total strength of wall 2. The strength of wall 2 during the 30%-XY test, including the effect of overturning moment, is shown in Figure 6–20.

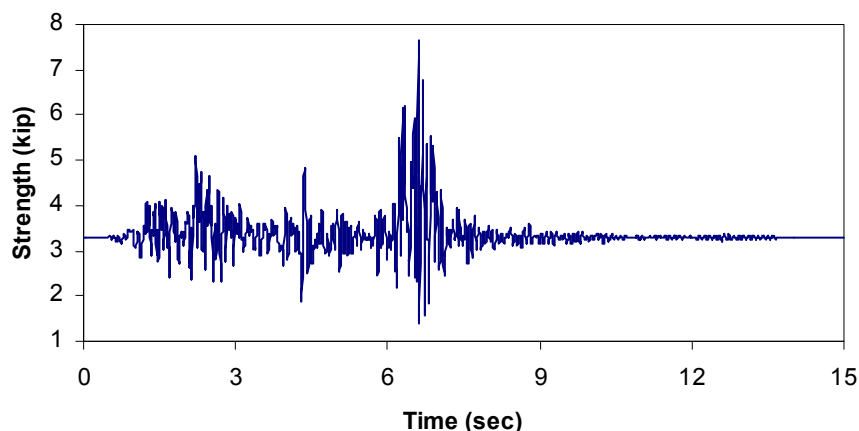


**Figure 6–20. Variation in strength of wall 2 including overturning moment for 30%-XY earthquake.**

The maximum strength of wall 2 displayed in Figure 6–20 is 7.6 kips, compared with the 11.2 kips of lateral load resisted during the test. Thus, there is a 50% increase in the capacity of wall 2 that is unaccounted for when considering only the behavior of the in-plane piers. Furthermore, the actual strength of wall 2 is 340% greater than the strength calculated by the rocking equation considering only gravity loads (3.3 kips). Based on these results, it seems that piers 4 and 8 must contribute to the lateral resistance of piers 11 and 12.

The other walls in the test structure did not demonstrate the great disparity between expected and actual strengths that wall 2 did. Table 6-2 compares the expected wall strengths (based on gravity loads and gravity loads plus overturning loads) with the peak force resisted by each wall. Based on the final crack patterns of walls B and 1 (Figure 5–19 and Figure 5–20), it seems that they did not reach their ultimate capacities; therefore, comparison between expected and actual strengths is difficult for these walls. The strength of wall A, which visibly rocked during testing, was accurately predicted to within 10% when overturning forces were included in the analysis. In general, the expected strengths for wall

A, wall B, and wall 1 seem to be in reasonable agreement with their experimental response; however, that is clearly not the case for wall 2. The behavior of corner piers with configurations similar to those of wall 2 need to be examined in additional detail to determine more accurately the effect that flanged piers have on rocking capacity.

**Table 6-2. Comparison of expected strengths and peak forces resisted for walls of test model.**

Wall	Peak Force (kip)	Expected (kip)	Expected Plus Overturn. (kip)
Wall A	13.33	9.26	14.69
Wall B	10.5	9.26	13.25
Wall 1	9.5	13.5	16.38
Wall 2	11.25	3.3	7.64

It must be emphasized that the expected strengths of the test model's walls, including the effects of overturning, are upper bounds in the sense that these capacities were calculated at points of maximum compressive load. As Figure 6-20 shows, the strength of the wall will be less than that value at all other points during the earthquake and will oscillate about the expected strength of the wall as calculated based on gravity loads. The inclusion of overturning effects in this section was primarily to demonstrate that there was no explanation for the high strength of wall 2 other than the participation of piers 4 and 8.

## Vertical Distribution of Lateral Forces

In order to design a structure for a specific base shear, the vertical distribution of lateral force must be determined. The standard method used by structural engineers considers the vertical distribution of mass in the structure and the height of the masses above the foundation. For the case where the floor masses are equal, the distribution of lateral forces is an inverted triangle shape. This procedure assumes that as the distance between the foundation and a mass increases, the greater the mass's acceleration (and the associated inertial force) will be. No consideration is given to the flexibility of the diaphragm. FEMA 368 states that the portion of the total base shear applied to level  $x$ ,  $C_{vx}$ , can be determined using the following equation:

$$C_{vx} = \frac{w_x h_x^k}{\sum_{i=1}^n w_i h_i^k} \quad \text{Equation 6-2}$$

where  $w_i$  and  $w_x$  are the portion of gravity load assigned to level  $i$  and  $x$ ,  $h_i$  and  $h_x$  are the height from the base to level  $i$  and  $x$ , and  $k$  is equal to 1.0 for structures

having a period of 0.5 seconds or less. Using this equation for the test model, the lateral force applied to the floor and roof levels would be equal.

Table 6-3 and Table 6-4 present the measured ratio of second-floor-level forces (F) to roof-level forces (R) for ground motion in the x-direction and y-direction, respectively. More specifically, the table looks at the ratio of inertial forces at the floor and roof level resulting from wall mass, diaphragm mass, and total mass. Inertial forces were computed by multiplying tributary masses by their accelerations in accordance with Table 6-1. At each level, the two in-plane wall forces were summed to determine the total wall force, and the total wall force and diaphragm force were summed to determine the total force at a given level.

**Table 6-3. Ratio of lateral floor forces to lateral roof forces in the x-direction (kips).**

Test	Wall, F	Diaph, F	Wall, R	Diaph, R	Diaph F/R	Wall F/R	Total F/R
10x	2.37	1.86	1.51	1.19	1.55	1.58	1.57
10xy	2.61	1.81	1.72	1.16	1.56	1.52	1.54
20x	5.97	4.22	3.54	2.86	1.48	1.69	1.59
20xy	8.28	5.16	4.63	2.80	1.84	1.79	1.81
30x	10.35	8.07	6.43	4.94	1.63	1.61	1.62
30xy	8.47	6.45	5.30	4.28	1.51	1.60	1.56
40x	11.88	7.40	7.50	4.45	1.66	1.58	1.61
<b>Average</b>					1.60	1.62	1.61

**Table 6-4. Ratio of lateral floor forces to lateral roof forces in the y-direction (kips).**

Test	Wall, F	Diaph, F	Wall, R	Diaph, R	Diaph F/R	Wall F/R	Total F/R
10y	3.35	1.75	2.07	1.57	1.11	1.62	1.40
10xy	3.59	1.77	2.22	1.64	1.08	1.62	1.39
20y	5.92	3.09	3.78	3.04	1.02	1.57	1.32
20xy	5.76	3.16	3.46	2.82	1.12	1.67	1.42
30xy	7.56	4.59	4.27	3.26	1.41	1.77	1.61
<b>Average</b>					1.15	1.65	1.43

The results shown in Table 6-3 and Table 6-4 demonstrate that the test model does not follow the traditional lateral force distribution used for design, which would result in a floor/roof force ratio equal to 1.0. In the x-direction, the behavior of the test model is consistent with the response of a stiff shear wall and flexible diaphragm system. The amplification of ground motion is small through the height of the in-plane walls, and consequently, the response of the diaphragms does not depend on their distance from the foundation. Assuming that the diaphragms at each level are essentially identical, they will demonstrate similar amplification of the ground motion (Figure 6-14). Thus, the distribution of lateral forces will be similar to the relative amounts of mass at the floor levels (Abrams 1995). For the test model, the floor/roof mass ratio is 1.89, which is considerably closer to the actual ratio of forces (1.62) than that predicted by

FEMA 368. Figure 6–21 plots the lateral forces at the floor and roof level for tests that contain a ground motion component in the x-direction.

The behavior of the test model for ground motion in the y-direction does *not* represent the response of a stiff shear wall and flexible diaphragm system. Based on the deformation modes of the diaphragms (Figure 6–16), the test model would more appropriately be described as an intermediate or semi-rigid system, where the displacement of the walls is comparable to the displacement of the diaphragm. As a result, the vertical distribution of lateral forces is not accurately described by either the FEMA 368 code equation or the ratio of floor masses. Figure 6–22 plots the lateral forces at the second floor and roof level for tests that contain a ground motion component in the y-direction.

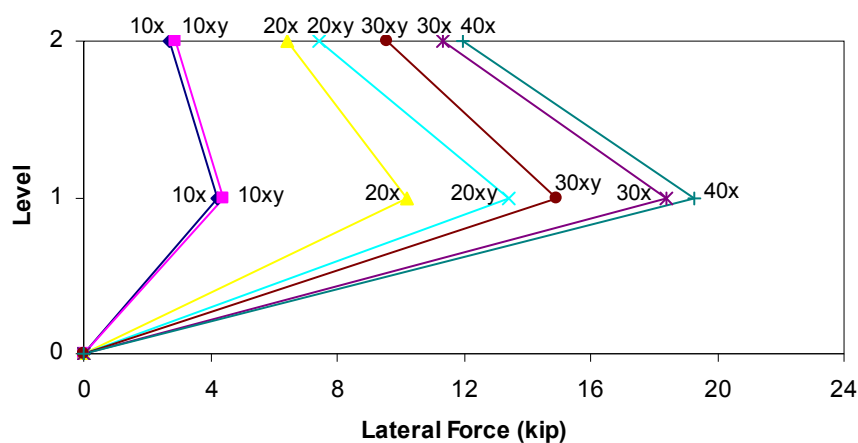


Figure 6–21. Vertical distribution of lateral forces in the x-direction.

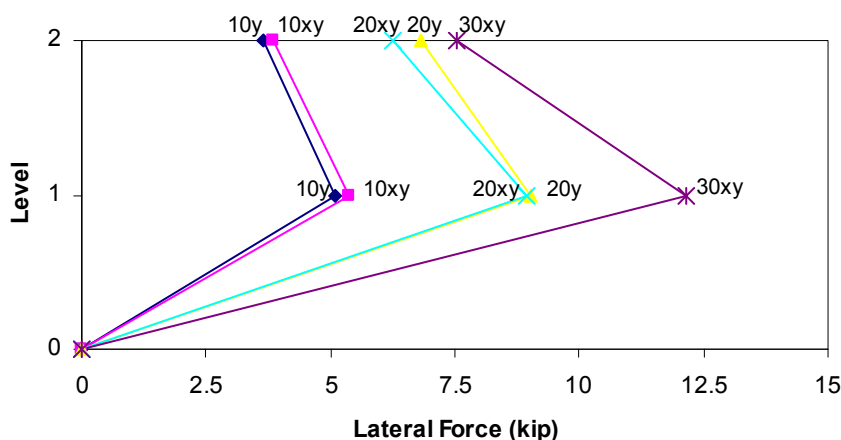


Figure 6–22. Vertical distribution of lateral forces in the y-direction.

### ***Combinational Effect of Bidirectional Excitation on Test Model***

The Nahanni earthquake was selected as the test motion primarily because preliminary analysis indicated that peak base shears resulting from the horizontal components occurred at the same time, resulting in an essentially 100%-100% combination during bidirectional excitation. Recall that the direction of the combination was positive in the x-direction and positive in the y-direction. Furthermore, the analysis predicted that twisting of the structure caused by ground motion in the y-direction resulted in base shears that added directly with the in-plane base shears on wall A (Figure 4-17 and Figure 4-20). Due to limitations of linear-elastic modeling and the fact that the ground motion simulation would be modified to account for shake table connectivity, there was some concern as to whether or not the measured building response would exhibit the combinations predicted by the preliminary analysis. However, the behavior of the test model during the 30%-XY earthquake seemed to indicate that the combinations did occur: all of the piers on wall A cracked and none of the uncracked piers on wall B displayed any damage. (Pier 8 cracked during the 30%-Y test.)

To demonstrate the severity of the base shear combinations, Table 6-5 and Table 6-6 present the maximum, minimum, and peak base shears on walls A and B for the 10% and 20% earthquake tests, respectively. In addition to the measured base shears, the base shears calculated by adding the time history responses from the unidirectional tests are also included in the tables. Walls 1 and 2 are not included because twisting of the structure is resisted almost entirely by walls A and B (Figure 4-20), so combinational effects are of little concern.

**Table 6-5. Base shear on wall A and wall B for 10% earthquakes (kips).**

	10% X		10% Y		10% XY		10% X + 10% Y	
	Wall A	Wall B	Wall A	Wall B	Wall A	Wall B	Wall A	Wall B
<b>Max</b>	2.0359	2.6113	1.2192	0.8356	2.2824	2.9646	2.0968	3.0415
<b>Min</b>	-2.6330	-3.0924	-1.3967	-1.0882	-4.4374	-3.3688	-3.4762	-3.2675
<b>Peak</b>	2.6330	3.0924	1.3967	1.0882	4.4374	3.3688	3.4762	3.2675

**Table 6-6. Base shear on wall A and wall B for 20% earthquakes (kips).**

	20% X		20% Y		20% XY		20% X + 20% Y	
	Wall A	Wall B	Wall A	Wall B	Wall A	Wall B	Wall A	Wall B
<b>Max</b>	4.9102	4.7174	3.3768	2.3557	6.1504	6.1756	5.0760	6.1039
<b>Min</b>	-6.6413	-6.1632	-3.6072	-2.5877	-11.3236	-5.5068	-10.0278	-6.4945
<b>Peak</b>	6.6413	6.1632	3.6072	2.5877	11.3236	6.1756	10.0278	6.4945

Table 6-5 and Table 6-6 confirm the visual response of the test model and show that the peak base shears on wall A due to unidirectional ground motion directly combined to produce a greatly increased response under bidirectional excitation.

In fact, the simultaneous xy-direction earthquakes produced base shears that were slightly larger than the superposed unidirectional base shears. The implications of these combinations on seismic provisions for design are discussed in Chapter 7. As would be expected, wall B did not show an increased response during the bidirectional tests, and experienced peak base shears that were essentially equal to those recorded during the x-direction-only tests.

Only the 10% and 20% earthquakes were examined for combinations of base shear because the test model was basically still linear-elastic at that point. Once the structural response becomes nonlinear and the piers reach their capacity, the combinations are disguised by the fact that the maximum applied load cannot surpass the lateral strength. Such was the case during the 30% tests, as a peak base shear of 11.41 kips was recorded on wall A during the 30%-X test, while a peak base shear of 12.24 kips was recorded during the 30%-XY case (a force which caused cracking in all piers). Thus, the load due to twisting initiated damage, but consequently did not demonstrate the real severity of the combination. As an illustration of these principles, Figure 6–23 plots the base shear on wall A during the 20% tests to show visually the nature of the additive response and Figure 6–24 confirms the linear behavior of wall A by superposition.

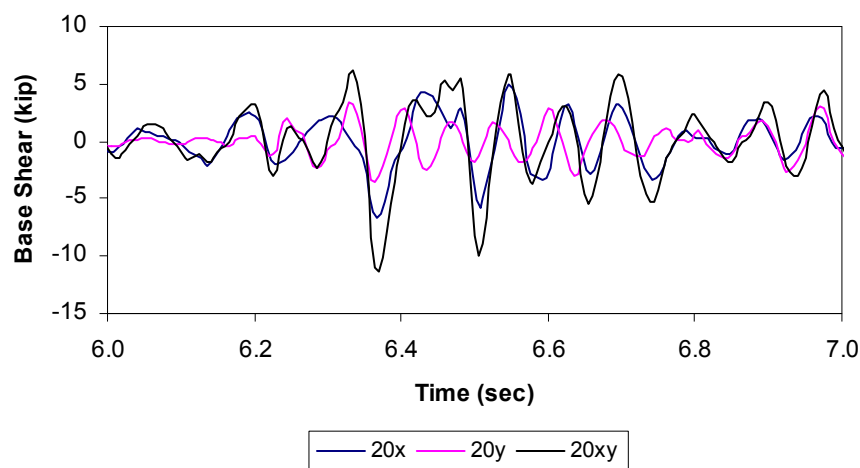


**Figure 6–23. Base shear on wall A due to 20% unidirectional and bidirectional earthquakes.**

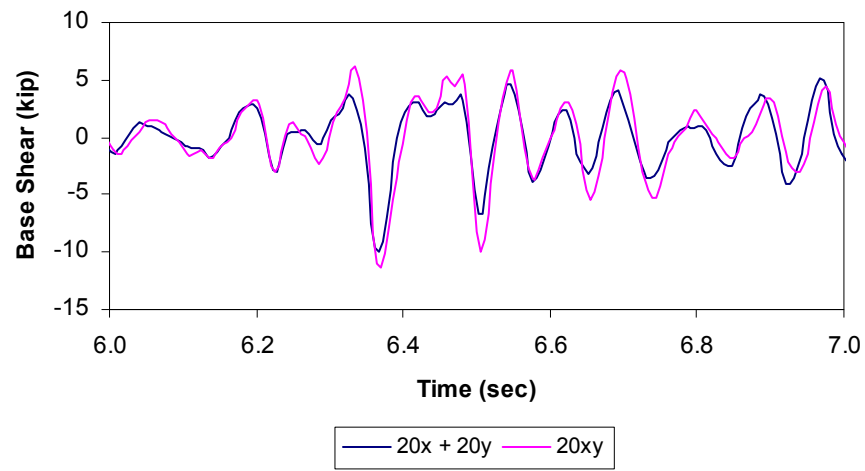


**Figure 6–24. Base shear on wall A for the superposition of the 20% unidirectional earthquakes and for the 20% bidirectional earthquake.**

## 7 Implications of Research on Seismic Provisions

Based on the results of the seismic tests, implications of this research on the seismic provisions contained in FEMA 356 are discussed. In particular, the following topics are addressed:

- force/deformation prescriptions for in-plane URM wall behavior
- vertical distribution of lateral forces for static analysis procedures
- strength contribution to in-plane walls from out-of-plane wall flanges
- combination of seismic forces for multi-component excitation.

### Force/Deformation Prescriptions

In Chapter 4, the predicted force/deformation curves for the test model's walls were determined based on FEMA 356 prescriptions (Figure 4–5 through Figure 4–7). Figure 7–1 through Figure 7–5 compare the predicted responses of the walls with the force/deformation backbone curves measured during the seismic tests. Based on the previous discussion of integrated wall displacements versus measured wall displacements, the former approach was for use in the figures. In addition, two figures are presented for wall 1 to account for the incorrect assumption that pier 9 would behave as a cantilevered pier. Figure 7–3 compares the measured wall 1 behavior with the original prediction and Figure 7–4 compares the measured wall 1 behavior with a recalculated FEMA 356 curve based on the actual response of pier 9.

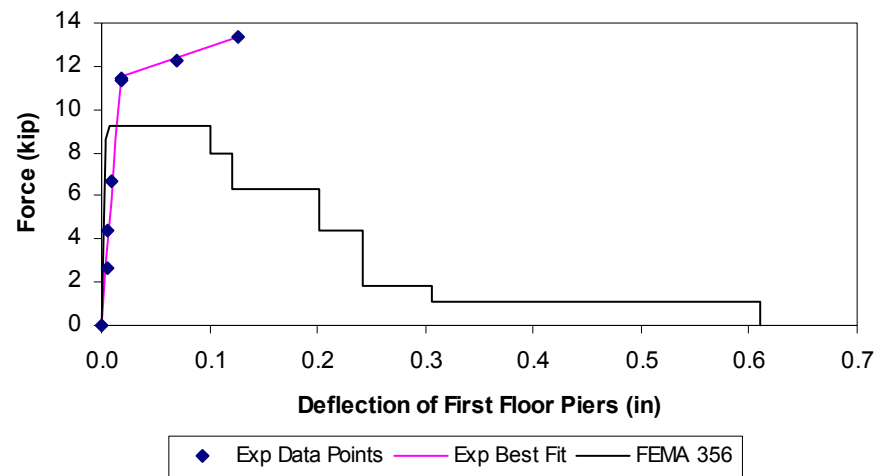


Figure 7-1. Comparison of force/deformation responses measured during seismic tests with those predicted by FEMA 356 for Wall A.

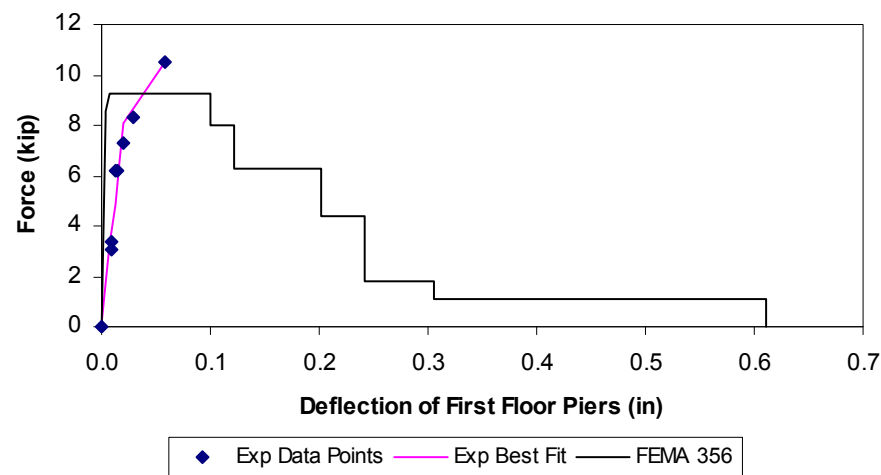


Figure 7-2. Comparison of force/deformation responses measured during seismic tests with those predicted by FEMA 356 for Wall B.

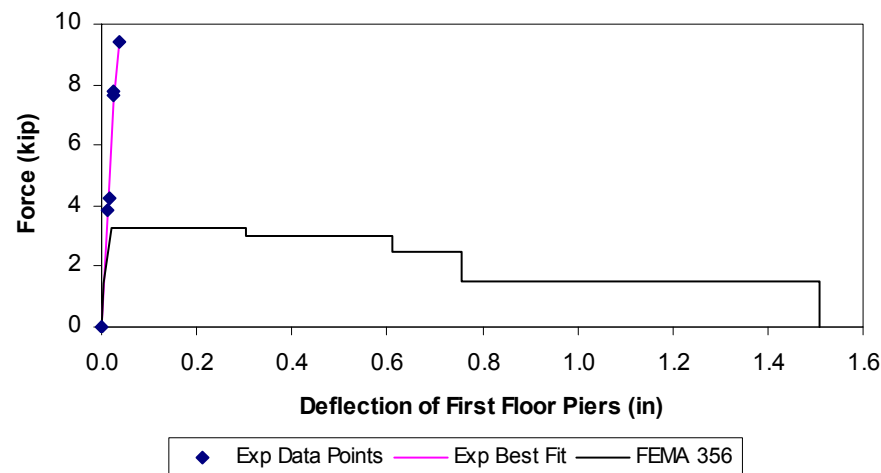
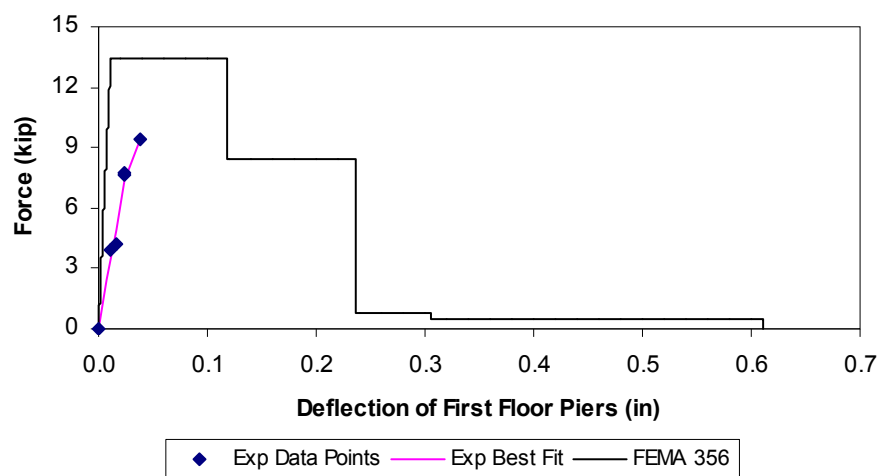
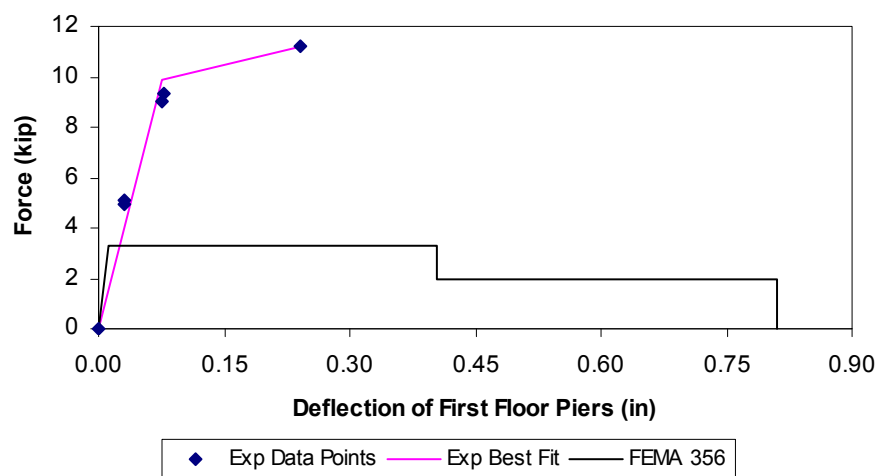


Figure 7-3. Comparison of force/deformation responses measured during seismic tests with those predicted by FEMA 356 for Wall 1.



**Figure 7-4.** Comparison of force/deformation responses measured during seismic tests with those predicted by FEMA 356 for Wall 1 (based on actual crack pattern).



**Figure 7-5.** Comparison of force/deformation responses measured during seismic tests with those predicted by FEMA 356 for Wall 2.

The predicted behaviors for wall A and wall B are in reasonable agreement with the measured responses. The peak forces resisted by wall A and wall B were 44% and 14% greater than predicted, respectively. The measured stiffness values for both walls were slightly lower than predicted by FEMA 356, but that would be expected given the assumptions that the masonry is homogenous and the full gross cross-section resists lateral deflection. Both walls also demonstrated a positively-sloped post-yield stiffness, in contradiction of the FEMA 356 assumption of perfectly plastic response. Finally, the strength degradation predicted by FEMA 356 could not be challenged because the deflection of the walls was not large enough.

The correlation between expected and measured responses was inconclusive for wall 1 and very poor for wall 2. Figure 7-3 shows that the peak force resisted by

wall 1 was 286% greater than the original prediction, while Figure 7-4 shows that the same peak force is 30% smaller than the predicted strength recalculated on the basis of the actual crack pattern of pier 9. However, the measured force/deformation behavior of wall 1 was essentially linear at the end of testing. Therefore it is difficult to judge the accuracy of the FEMA 356 curve since wall 1 retained some strength. As noted in Chapter 6, the peak force resisted by wall 2 was 340% greater than predicted. That result was probably due to unaccounted flange strength, as discussed later in this chapter.

## Vertical Distribution of Lateral Forces

Chapter 3 of FEMA 356 prescribes methods for determining the vertical distribution of lateral forces for use in both linear static and nonlinear static analysis procedures. The linear static method permits the use of either of two different distributions for URM structures. The first is the same as Equation 8-2 in FEMA 356 and takes the shape of an inverted triangle when the floor masses are equal. The second distribution (section 3.3.1.3.5) involves a base shear computation for each floor that is proportional to the weight of the floor. The determination of the base shear is also dependent on other factors, but if the properties of the stories are identical then the vertical distribution of lateral load will be proportional to the story masses. Unlike the linear static method, the nonlinear static method *requires* that two load patterns be used in the analysis as a way to bound the range of building response. One of the selected patterns must be a modal distribution while the other may either be proportional to the story masses or be an adaptive procedure that accounts for the properties of the yielded structure.

The vertical distributions of lateral force prescribed in FEMA 356 allow the designer to consider both rigid and flexible diaphragm behavior. There is no doubt that these distributions will bound the actual force distribution in a building, and in that sense they are definitely satisfactory. However, if a more accurate description of structural behavior is desired, some combination of these methods may be necessary for buildings that have diaphragms with an intermediate amount flexibility. The diaphragms of the test model, which demonstrated acceleration amplifications on the low end of the flexible range to the high end of the intermediate range, exhibited floor force to roof force ratios of 1.61 in the x-direction and 1.43 in the y-direction (Table 6-3 and Table 6-4). Both of those ratios fall within the middle 50% of the range of the floor force to roof force ratios calculated using Equation 8-2 (1.0) and based on the distribution of floor masses (1.89). Consequently, the measured vertical distributions of lateral forces are

well bounded by the prescriptions of FEMA 356 (as intended by the code), but at the same time, the computed distributions do not accurately describe the actual behavior of the test model.

### **Strength Contributions to In-Plane Walls from Out-of-Plane Wall Flanges**

The measured versus predicted strengths of wall 2 (Figure 7–5) clearly demonstrate a great discrepancy. In Chapter 6, two possible explanations for the unexpected strength were examined: the beneficial effect of compressive overturning moment and out-of-plane wall flange effects. The discussion demonstrated that while the compressive overturning moment could have increased the strength of wall 2 by a notable amount, it was not nearly enough to solely account for the discrepancy. Therefore, it is believed that pier 4 and pier 8 significantly increased the rocking resistance of pier 12 and pier 11, respectively.

Presently, strength contributions to in-plane walls from out-of-plane wall flanges are not considered in FEMA 356, and various studies have demonstrated that flanges do not increase in-plane wall strength at high intensity levels (see Costley and Abrams 1996 and Paquette and Bruneau 2003, for example). However, pier layouts in those studies were very similar to wall A and wall B, which did not demonstrate the great difference in expected and measured strengths exhibited by wall 2. Wall 2, unlike wall A and wall B, has only two relatively small piers with adjacent out-of-plane wall piers of equal length and 50% greater thickness. In the current study, the strength of the in-plane piers is so low that the effect of the flanges is very pronounced. Furthermore, the in-plane piers of wall 2 truly formed combined sections with their adjacent out-of-plane wall piers after cracking, forcing them to rock together (Figure 6–19). Again, the layout used in the current study is dissimilar to the studies noted above in that the out-of-plane walls in those studies were solid.

There are not sufficient quantifiable results from this phase of the research to recommend specific changes to FEMA 356. It may reasonably be argued that ignoring any possible beneficial flange effects is prudent and conservative, but the apparent 3.4 factor of safety associated with wall 2 would nevertheless seem excessive. Further research would be advisable to determine the influence of out-of-plane wall flanges on in-plane wall strength for a variety of layouts.

## Combination of Seismic Forces for Multi-component Excitation

Section 3.2.7 of FEMA 356 details the requirements for considering multidirectional seismic effects. It states that

multidirectional seismic effects shall be considered to act concurrently for buildings meeting the following criteria:

1. The building has plan irregularities, or
2. The building has one or more primary columns which form a part of two or more intersecting frame or braced frame elements.

FEMA 356 subsection 3.2.7.1, “Concurrent Seismic Effects,” prescribes that for both linear and nonlinear procedures, the maximum force resulting from a horizontal component shall be added to 30% of the maximum force resulting from the other horizontal component when computing the design force. However, the response of the test model to the bidirectional Nahanni earthquake demonstrated that base shears on wall A resulting from orthogonal components combined directly, contradicting the 100%-30% rule in FEMA 356. Table 6-5 and Table 6-6 present the measured base shears on wall A for the 10% and 20% level unidirectional and bidirectional earthquakes.

The unusual behavior of a single test model does not necessarily imply that the 100%-30% rule needs to be changed. Recall that concurrent peak forces due to orthogonal components were not present in the time-history analyses of the El Centro and Loma Prieta earthquakes (Sweeney et al. 2004). However, the current study should serve as a reminder that there are exceptions to the 100%-30% rule, so all due caution should be taken when performing any seismic analysis.

The response of a given building to a specific earthquake is unique. Consequently, the prediction of combinational effects is very difficult since it is impossible to predict the exact ground motions to which a building will be subjected during its life cycle. Nevertheless, certain structural features will result in greater susceptibility to large force combinations. Among those are:

- floor and roof diaphragms with rigid to intermediate flexibility
- in-plane lateral force resisting systems that are not symmetric
- similar fundamental periods in horizontal plan directions (Lopez et al. 2001).

When performing a structural analysis it would also be prudent to select a large number of ground motions with varying characteristics. The most difficult as-

pect of computer modeling is the creation of the structural system and the first seismic analysis. It is usually a straightforward task to modify the analysis to include additional ground motions. Furthermore, as this study has shown, linear time-history analysis is an excellent method to use when examining combination effects since the forces resulting from each ground motion component can be examined over the duration of the earthquake.

## 8 Conclusions and Recommendations

### Conclusions

Based on the results of this research, conclusions are offered in connection with each of the project objectives:

1. *Determine failure mechanisms and force/deformation behavior of the test model's walls.*

The test model resisted ground motion accelerations of up to 0.772 g and sustained a relatively small amount of damage, demonstrating that URM systems with flexible diaphragms are capable of resisting large-magnitude earthquakes.

The piers of wall A and wall 2 demonstrated stable rocking behaviors with ductility values of 5.0 and 3.5, respectively. Given the level of damage, additional deformation capacity was likely.

Wall B and wall 1 did not develop failure mechanisms.

2. *Examine acceleration amplification of the ground motion by the walls and the diaphragms.*

In general, the wall amplification of the ground acceleration was small. In the x-direction, average wall amplifications were slightly less than 1.0 at the second-floor level and slightly larger than 1.0 at the roof level. In the y-direction, initial wall amplifications were approximately 1.5, with roof values just above and floor values just below. The larger amplification in the y-direction was presumably due to its lower stiffness as compared with the stiffness in the x-direction. As earthquake intensity increased (along with damage), wall amplification in the y-direction converged to 1.0.

The diaphragm amplification of ground accelerations in the x-direction was approximately 2.0 – 2.5, constituting a building response on the stiffer side of

the rigid-wall/flexible-diaphragm range. As expected, diaphragm amplifications decreased after pier rocking initiated on wall A.

The diaphragm amplification of ground accelerations in the y-direction were initially around 2.5 at the roof level and around 1.5 at the second-floor level. Consequently, the behavior of the floor diaphragm was not consistent with a rigid-wall/flexible-diaphragm system as defined in FEMA 356, and would be more appropriately described as semi-rigid. This response was a result of the flexibility of the first-story piers of wall 2. Like the diaphragms in the x-direction, acceleration amplifications decreased in the y-direction after pier rocking initiated on wall 2.

3. *Approximate the effect, if any, that the flange portions of out-of-plane walls have on the strength of in-plane walls.*

The expected strength of wall 2 was 3.3 kips, but the measured strength was 11.2 kips. Based on previous calculations, it appears that at least 32%, or 3.6 kips, of the measured strength was due to participation of out-of-plane wall flanges.

Wall A, wall B, and wall 1 did not demonstrate the degree of disparity between expected and measured strengths that wall 2 exhibited. Consequently, it is believed that either the expected strength of wall 2 was so small that flange effects were more apparent or that the isolation of the flanges from wall A and wall B through cracking enabled greater participation in the response of wall 2 (Figure 6–19).

4. *Investigate the vertical distribution of lateral forces for stiff-wall/flexible-floor systems.*

The average ratio of lateral second-floor-level forces to roof-level forces was 1.61 in the x-direction and 1.43 in the y-direction.

The measured vertical distribution of lateral forces was bounded by the distribution calculated from the ratio of floor masses (1.89) and from the standard FEMA 356 equation for rigid diaphragms (1.0).

5. *Determine the combinational effect of multidirectional base motions on the test model.*

Peak base shears due to orthogonal horizontal ground motion components combined directly on wall A as predicted by finite element analysis. The combinations occurred during each bidirectional test through which the test structure remained linear-elastic (10%-XY and 20%-XY). During the nonlinear response of wall A, the combinations were masked by the fact that combining base shears could not be larger than the wall strength.

Combinational effects like those occurring on wall A did not occur with the same severity on the other walls of the test model.

6. *Provide fundamental knowledge needed to develop seismic protection design.*

With exception to wall 2, the FEMA 356 force/deformation prescriptions predicted the behavior of the test model's walls with acceptable accuracy.

The two primary types of methods used to vertically distribute lateral forces, as prescribed by FEMA 356, bounded the actual behavior of the test model, as they were intended to do.

Out-of-plane wall flanges are not currently considered in calculating the strength of in-plane walls using FEMA 356. As a result, the actual strength of wall 2, for example, was measured to be 3.4 times greater than that predicted by FEMA 356.

Although wall A experienced a 100%-100% combination of base shears, this behavior is rare. Consequently, a change in the 100%-30% rule prescribed in FEMA 356 is not necessarily recommended. However, structural engineers should be aware of the potential risk of using this formulation to address concurrent seismic effects resulting from multidirectional excitation.

## Recommendations

Based on the conclusions, the following recommendations are offered:

The results of this study indicate that research should be conducted to quantify the effects of out-of-plane wall flanges on in-plane wall strength. A sufficient variety of pier layouts should be studied to determine how the connection of different types of URM walls results in greater flange participation. In order to produce definitive results, both strong in-plane wall/weak out-of-plane wall and weak in-plane wall/strong out-of-plane wall systems should be investigated.

Additional research should be performed to determine the effect of overturning forces on the in-plane strength of piers.

Research should be conducted to determine critical ground motion characteristics that lead to the direct combination of response quantities due to orthogonal earthquake components.

The results of this study should feed into future research on developing more effective techniques for seismic rehabilitation of URM building systems.

## References

- Abrams, D.P. 1995. "The importance of the diaphragm on seismic response of buildings." *Structures Congress – Proceedings, Restructuring: America and Beyond* 2, 1813-1816.
- Anastassiadis, K., Avramidis, I.E., and Panetsos, P. 2002. "Concurrent design forces in structures under three-component orthotropic seismic excitation," *Earthquake Spectra* 18, 1-17.
- American Forest and Paper Association. 1997. *National Design Specification for Wood Construction (NDS)*.
- ASTM C109/C109M-02, *Standard Test Method for Compressive Strength of Hydraulic Cement Mortars* (Using 2-in. or [50-mm] Cube Specimens) (ASTM International, West Conshohocken, PA, 10 June 2002).
- Beskos, D.E., and Anagnostopoulos, S.A., ed. 1997. *Computer Analysis and Design of Earthquake Resistant Structures*, Computer Mechanics Publication, Boston.
- Carleton, H.D. 1970. "Digital Filters for Routine Data Reduction." Waterways Experiment Station Miscellaneous Paper N-70-1.
- Chopra, A. 2001. *Dynamics of Structures: Theory and Applications to Earthquake Engineering*, Prentice Hall.
- Cohen, G. 2001. *Seismic Response of Low-Rise Masonry Buildings with Flexible Roof Diaphragms*, Master Thesis, University of Texas at Austin.
- Costley, A.C., and Abrams, D.P. 1996. *Dynamic Response of Unreinforced Masonry Buildings with Flexible Diaphragms*, National Center for Earthquake Engineering Research Technical Report NCEER-96-0001.
- Faherty, K., and Williamson, T. 1997. *Wood Engineering and Construction Handbook 3<sup>rd</sup> Edition*, McGraw-Hill.
- Federal Emergency Management Agency (FEMA). 1999. *Evaluation of Earthquake Damaged Concrete and Masonry Wall Buildings*, FEMA 306, Washington D.C.
- \_\_\_\_\_. 2000. *Prestandard and Commentary for the Seismic Rehabilitation of Buildings*, FEMA 356, Washington D.C.
- \_\_\_\_\_. 2001. *NEHRP Recommended Provisions for Seismic Regulations for New Buildings and Other Structures*, Part 1 – Provisions, FEMA 368, Washington D.C.
- \_\_\_\_\_. 2001. *NEHRP Recommended Provisions for Seismic Regulations for New Buildings and Other Structures*, Part 2 – Commentary, FEMA 369, Washington D.C.
- Harris, H., and Sabnis, G. 1999. *Structural Modeling and Experimental Techniques 2<sup>nd</sup> Edition*, CRC Press.

- Hwang, J., and Hsu, T., 2000. "Experimental study of isolated building under triaxial ground excitations," *Journal of Structural Engineering-ASCE* **126**:8, 879-886.
- Kariotis, J.M. 1995. "Seismic response of unreinforced masonry buildings with flexible diaphragms." *Structures Congress – Proceedings, Restructuring: America and Beyond* **2**, 1817-1820.
- Kingsley, G.R., Magenes, G., and Calvi, G.M. 1996. "Measured Seismic Behavior of a Two-Story Masonry Building." *Structures Congress – Proceedings, Worldwide Advances in Structural Concrete and Masonry*, 123-134.
- Lopez, O., Chopra, A.K., and Hernandez, J.J., 2001. "Evaluation of combination rules for maximum response calculation in multicomponent seismic analysis," *Earthquake Engineering and Structural Dynamics* **30**, 1376-1398.
- Masonry Standard Joint Committee (MSJC). 1999. *Building Code Requirements for Masonry Structures*.
- Moon, Franklin L., *Seismic Strengthening of Low-Rise Unreinforced Masonry Structures with Flexible Diaphragms*, doctoral thesis. Georgia Institute of Technology, May 2004. [http://etd.gatech.edu/theses/available/etd-12112003-110041/unrestricted/Moon\\_Franklin\\_L\\_200405\\_phd.pdf](http://etd.gatech.edu/theses/available/etd-12112003-110041/unrestricted/Moon_Franklin_L_200405_phd.pdf).
- Pacific Earthquake Engineering Research (PEER) Strong Motion Database. Regents of the University of California, June 2002. <http://peer.berkeley.edu/smcat>.
- Paquette, J., and Bruneau, M. 2003. "Pseudo-Dynamic Testing of Unreinforced Masonry Building with Flexible Diaphragm." *Journal of Structural Engineering* **129**:6, 708-716.
- SAP2000 Non-Linear Version 7.40. 2000. Computers and Structures, Inc., Berkeley, CA.
- Seismic Test EXecution (STEX). MTS Systems Corp, Eden Prairie, MN.
- Simsir, C.C., Aschheim, M.A., and Abrams, D. P., 2001. "Response of unreinforced masonry bearing walls situated normal to the direction of seismic input motions," *Proceedings 9th Canadian Masonry Symposium*, Fredericton, Canada.
- Sweeney, S., Horney, M., and Orton, S. 2004. *Tri-Directional Seismic Analysis of an Unreinforced Masonry Building With Flexible Diaphragms*, U.S. Army Engineer Research and Development Center, Construction Engineering Research Laboratory, Technical Report TR-04-6.
- Tena-Colunga, A. 1992. *Response of an Unreinforced Masonry Building During the Loma Prieta Earthquake*, PhD Thesis, University of Illinois Urbana-Champaign, 1992.
- United States Army Corps of Engineers (USACE). 1998. "Technical Instructions: Seismic Design for Buildings," TI 809-04, Washington, D.C.
- Wilson, E.L., Der Kiureghian, A., and Bayo, E. P., 1981. "A replacement for the SRSS method in seismic analysis," *Earthquake Engineering and Structural Dynamics* **9** (2), 187-194.
- Yi, Tianyi, *Experimental Investigation and Numerical Simulation of an Unreinforced Masonry Structure with Flexible Diaphragms*, doctoral thesis. Georgia Institute of Technology, February 2004. [http://etd.gatech.edu/theses/available/etd-02262004-135843/unrestricted/yi\\_tianyi\\_200405\\_phd.pdf](http://etd.gatech.edu/theses/available/etd-02262004-135843/unrestricted/yi_tianyi_200405_phd.pdf).

REPORT DOCUMENTATION PAGE				Form Approved OMB No. 0704-0188	
Public reporting burden for this collection of information is estimated to average 1 hour per response, including the time for reviewing instructions, searching existing data sources, gathering and maintaining the data needed, and completing and reviewing this collection of information. Send comments regarding this burden estimate or any other aspect of this collection of information, including suggestions for reducing this burden to Department of Defense, Washington Headquarters Services, Directorate for Information Operations and Reports (0704-0188), 1215 Jefferson Davis Highway, Suite 1204, Arlington, VA 22202-4302. Respondents should be aware that notwithstanding any other provision of law, no person shall be subject to any penalty for failing to comply with a collection of information if it does not display a currently valid OMB control number. <b>PLEASE DO NOT RETURN YOUR FORM TO THE ABOVE ADDRESS.</b>					
1. REPORT DATE (DD-MM-YYYY) September 2005		2. REPORT TYPE Final		3. DATES COVERED (From - To)	
4. TITLE AND SUBTITLE  Seismic Response of a Half-Scale Masonry Building with Flexible Diaphragms				5a. CONTRACT NUMBER	
				5b. GRANT NUMBER	
				5c. PROGRAM ELEMENT NUMBER 21 2040 622784T4100	
6. AUTHOR(S)  Steven C. Sweeney, Matthew A. Horney, and Sarah L. Orton				5d. PROJECT NUMBER AT41-CFM-A001	
				5e. TASK NUMBER	
				5f. WORK UNIT NUMBER	
7. PERFORMING ORGANIZATION NAME(S) AND ADDRESS(ES) U.S. Army Engineer Research and Development Center Construction Engineering Research Laboratory P.O. Box 9005 Champaign, IL 61826-9005				8. PERFORMING ORGANIZATION REPORT NUMBER ERDC/CERL TR-05-25	
9. SPONSORING / MONITORING AGENCY NAME(S) AND ADDRESS(ES) Headquarters, U.S. Army Corps of Engineers 441 G Street NW Washington, DC 20314-1000				10. SPONSOR/MONITOR'S ACRONYM(S)	
				11. SPONSOR/MONITOR'S REPORT NUMBER(S)	
12. DISTRIBUTION / AVAILABILITY STATEMENT  Approved for public release; distribution is unlimited.					
13. SUPPLEMENTARY NOTES					
14. ABSTRACT <p>Unreinforced masonry (URM) buildings constructed on Army installations before the development of modern seismic codes may be susceptible to earthquake damage and therefore could benefit from seismic mitigation measures. Improved understanding of URM structural response under multidirectional loads is required to develop the most effective seismic structural retrofit strategies.</p> <p>This research used a half-scale structural model to investigate the seismic response of URM buildings with flexible diaphragms. The objectives were to determine failure mechanisms and deformation behaviors; examine amplification of ground motion acceleration by walls and diaphragms; approximate any strength effects that flange portions of out-of-plane walls may have on in-plane walls; investigate vertical distribution of lateral forces; and identify any combinational effects of multidirectional base motions.</p> <p>An unexpected level of out-of-plane wall flange contribution to in-plane wall strength indicates the need for experimental quantification using different pier layouts, URM wall combinations, and wall connection methods. Results also indicate the need to investigate the effect of overturning forces on the in-plane strength of piers and to determine critical ground motion characteristics that lead to the direct combination of response quantities due to orthogonal earthquake components.</p>					
15. SUBJECT TERMS unreinforced masonry (URM), seismic engineering, flexible diaphragms, finite element analysis, Triaxial Earthquake and Shock Simulator (TESS), Nahanni earthquake					
16. SECURITY CLASSIFICATION OF:			17. LIMITATION OF ABSTRACT	18. NUMBER OF PAGES  127	19a. NAME OF RESPONSIBLE PERSON
a. REPORT Unclassified	b. ABSTRACT Unclassified	c. THIS PAGE Unclassified			19b. TELEPHONE NUMBER (include area code)